AN ABSTRACT OF THE THESIS OF

David R. Michalsen for the degree of Master of Science in Ocean Engineering presented on July, 15 2004.

Title: An Investigation on the Modeling of Wave Field Transformation and Shoreline Morphology Near Steep Bathymetric Features

Redacted for Privacy

Abstract approved: _____

Merrick C. Haller

Steep bathymetric anomalies in the beach profile, such as offshore borrow pits, submerged breakwaters, and nearshore canyons can significantly transform the wave climate through the effects of refraction, diffraction, and reflection. When located in the nearshore region the modified wave climate can also substantially change the location of breaking and has been observed to impact the shoreline morphology. The current study focuses on the borrow pit case and attempts to explain how limitations in existing methodologies may impact the predictions in both the wave field modification and shoreline response. Recent analytical methods by Bender (2003) have successfully explained the wave transformation near pits. However, these models are only capable of modeling bathymetries of constant depth surrounding the anomaly. Therefore in order to investigate cases without this restriction, this often requires numerical solutions following Berkhoff's (1972) mild-slope equation (MSE). However, a significant limitation of these model types is the accuracy suffers for steep bathymetric features. Booij (1983) demonstrates this for slopes larger than 1:3 (rise:run). Furthermore, these models often rely on Radder's (1979) parabolic approximation to the MSE which restricts the ability to include wave reflection which can be substantial in the case of a borrow pit. These limitations and their effects on shoreline response are investigated in the current study. By utilizing a form of the modified mild-slope equation (MMSE) originally derived by Massel (1993) the

limitation of the MSE in representing steep features is removed. Additionally, a numerical model following Lee et al. (1998) is employed to investigate wave transformation around borrow pits of arbitrary depth. The formulation of the model is of hyperbolic form; therefore, the reflected waves generated by a borrow pit are included. The models accuracy is validated through a rigorous set of tests showing that the model compares well with previous analytical solutions for steep features.

To estimate the importance of wave reflection, information from documented borrow sites is gathered. Using dimensionless parameters relating the incident waves and the pit geometry, an estimate of the amount of reflection generated by each borrow pit is calculated. It is shown that upward of 30% of the wave energy can be reflected by a borrow pit. Additionally, it is shown as wave frequency increases (or *kh* located in the intermediate depth region), the MSE's inaccuracy in predicting reflection is enhanced. Expanding on this conclusion, a parameterization analysis is performed. The analysis describes conditions under which resonance inside the trench capable of producing large reflection is reached. The study serves as preliminary design guidance which can be used to avoid borrow pit geometries that are capable of producing a large amount of reflection.

It is also of interest to describe how the effects of reflection affect the regions far shoreward of the pit. Employing a form of the MMSE model, the evolution of the wave field is analyzed. It was found that although the effects of reflection are strong near the borrow pit, as the distance leeward of the pit increases the effects of refraction and diffraction outweigh the impacts of reflection. Thus, the result using a wave model including reflection would not substantially differ from that of using a model that neglects the reflected waves when investigating the impacts on shoreline evolution.

Finally, the last part of the study looks at the validity of utilizing current shoreline response models for this particular problem. Wave height and direction at breaking dictate how one-line models predict shoreline response. However, these models fail to include the effect that longshore gradients in wave height have on generating mean water level (MWL) gradients. MWL gradients in wave height are capable of producing longshore currents which can significantly alter the sediment

transport trends. Coupling the MMSE wave model with a 2DH nearshore circulation model shows that MWL gradients have a significant impact on current generation. Results indicate that incipient rip currents result from the converging currents associated with the MWL gradients. The presence of these currents would thereby dictate a new sediment transport trend, possibly transporting sediment offshore instead of in the theorized salient formation predicted by one-line models.

An Investigation on the Modeling of Wave Field Transformation and Shoreline Morphology Near Steep Bathymetric Features

by
David R. Michalsen

A THESIS

submitted to

Oregon State University

in partial fulfillment of
the requirements for the
degree of

Master of Science

Presented July, 15 2004
Commencement June 2005

Master of Science thesis of David R. Michalsen
presented on July 15, 1 2004.

APPROVED:

Redacted for Privacy

Major Professor, representing Ocean Engineering

Redacted for Privacy

Head of the Department of Civil, Construction, and Environmental Engineering

Redacted for Privacy

Dean of the Graduate School

I understand that my thesis will become part of the permanent collection of the Oregon State University libraries. My signature below authorizes release of my thesis to any reader upon request.

Redacted for Privacy

David R. Michalsen, Author

ACKNOWLEDGEMENTS

I would like to thank Dr. Mick Haller for always being there to answer my questions and giving me the opportunity to work on this project. I would also like to thank Dr. K.D. Suh and Dr. Tuba Ozkan-Haller whose knowledge was a tremendous asset with questions I had about the numerical models and the topic in general. I would like to thank my other committee member Dr. Daniel Cox for his time and advice on the presentation of my work. Additionally, Dr. Christopher Bender was a wonderful help and his generosity to provide insight on the topic was very much appreciated.

Finally I want to thank Mandy Sapp for being the best possible person I could ever ask to be with. You mean more than anything to me and your love and support is something I truly cherish.

TABLE OF CONTENTS

TABLE OF CONTENTS (continued)

TABLE OF CONTENTS (continued)

LIST OF FIGURES

LIST OF FIGURES (continued)

LIST OF FIGURES (continued)

LIST OF FIGURES (continued)

LIST OF FIGURES (continued)

LIST OF FIGURES (continued)

LIST OF TABLES

1.0 Introduction

This study investigates how the presence of relatively steep bathymetric anomalies in the nearshore region (e.g. offshore borrow pits, submerged breakwaters, or rocky outcrops) modify the wave climate and impact the shoreline morphology. A borrow pit is generated by the dredging of sediment from an offshore site, which leaves an irregular bathymetric feature in the beach profile. The impacts of borrow sites on both the wave field and shoreline response has been of considerable interest recently due to the popularity of beach nourishment as a safeguard against the on-going problem of coastal erosion. Since the cost of borrow material significantly increases in areas further offshore, these features are often found in the nearshore region. Another example of a relatively steep feature located in the nearshore region is a submerged breakwater (i.e. artificial reef). These structures also serve as a device for shore protection and are composed of rubble mound embankments that fall below the wave trough line so they are submerged at all times. Such structures are commonly used in place of surface piercing breakwaters which can be undesirable due to their unaesthetic appearance or their consequences on marine life. Since wave action is allowed to propagate over these structures, the impacts on the wave field can be substantial, especially if wave breaking is induced. Naturally occurring bathymetric features that can also be classified as a nearshore bathymetric anomaly are rocky outcrops and nearshore canyons. Examples of these are the Scripps and La Jolla canyons which have recently been studied in the Nearshore Canyon Experiment (NCEX) near La Jolla, California. At the site significant impacts to the wave climate, nearshore circulation, and potentially shoreline morphology have been shown (e.g. Thornton and Stanton 2003; Long et al. 2003).

In conclusion, although steep features have been witnessed to severely impact the wave climate in their vicinity, many methods employed for predicting this process may be flawed. The present study investigates the significance of these flaws to determine whether new steps should be taken in future analysis.

1.1 Nature of problem

The borrow pit, submerged breakwater, and nearshore canyon all serve as examples where complex wave transformation results. The current study places main emphasis on the borrow pit and the potential consequences it creates. A study by Combe and Soileau (1987) in Grand Isle, Louisiana has spurred a great deal of interest in the shoreline response patterns generated around this type of anomaly. The presence of two salient formations was observed directly shoreward of the borrow sites as shown in Figure 1.1. The principal effect of any bathymetric anomaly is the wave field modification through the effects of refraction, diffraction, and reflection as illustrated in Figure 1.2. The change in depth causes the waves to refract away from the pit centerline much like a lens refracts light. As a result the wave energy directly leeward of the pit becomes minimal and a so-called "shadow region" is created. As the waves propagate to shore the persistence of diffraction will allow energy to leak back into the shadow region as the distance from the pit becomes greater. Additionally, especially if the geometry of the pit is such that resonance inside of the pit is met, significant reflection may also be generated. A large amount of wave reflection may also result in a more extensive shadow region, since the energy transmitted past the pit would be substantially reduced. All of these effects are magnified if the feature is located within the nearshore region. Here, the disruption from equilibrium created when the pit is dredged will subsequently drive changes in the circulation pattern and modify the sediment transport pattern that governs shoreline morphology. It has been theorized by authors such as Dean (2002) that a shadow region of low wave set up surrounded by regions of high wave setup will initiate mean water level (MWL) gradients capable of driving longshore currents. This result will have a prominent impact on the longshore sediment transport rate. The presence of converging and diverging currents may be responsible for generating the phenomenon witnessed in Grand Isle, LA. The cuspate features seen here have since been referred to as an Erosional Hot Spot (EHS). In a standardized classification of various types of EHS, the U.S. Army Corps of Engineers classify this EHS as Type 11 (e.g. Kraus and Galgano 2001).

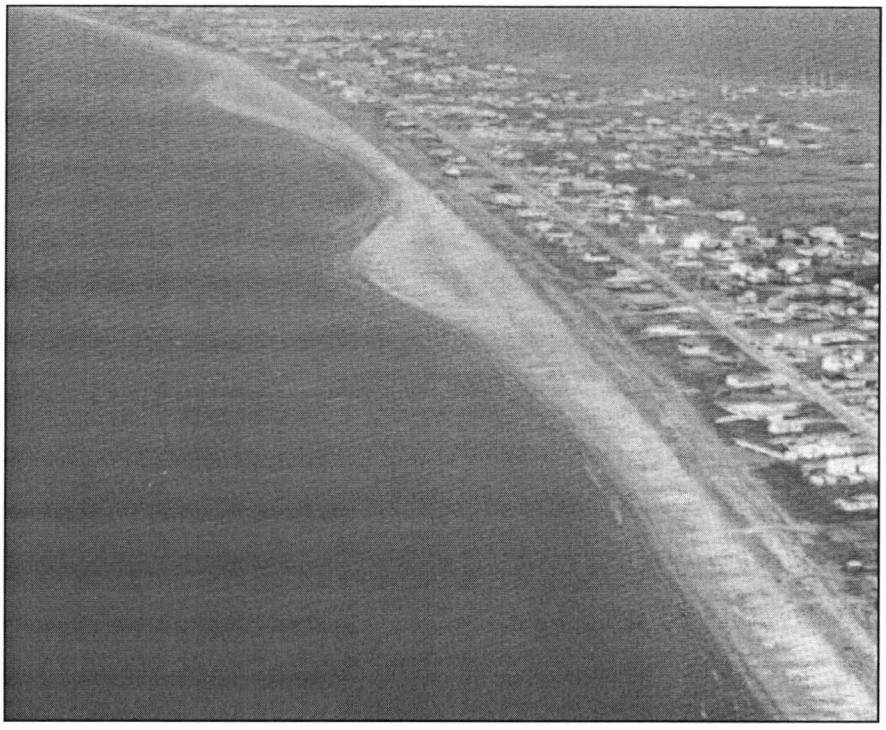

Figure 1.1: Salient formations witnessed in Grand Isle, LA (from Combe and Soileau, 1987)

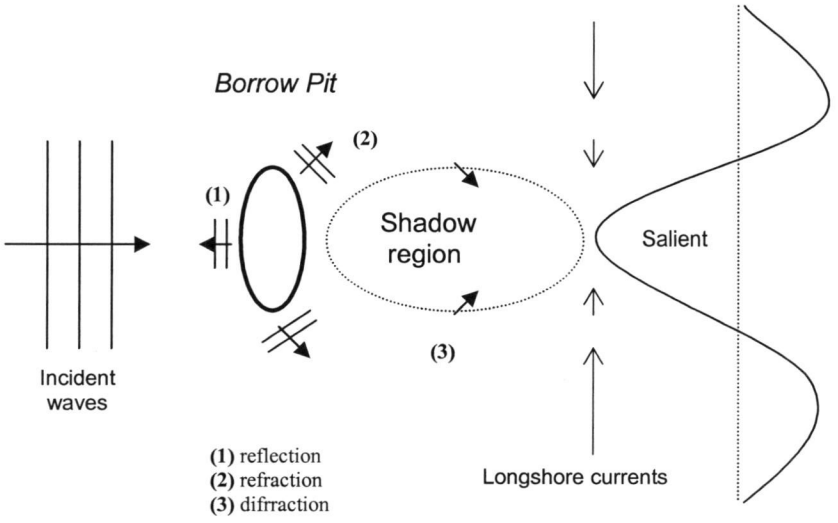

Figure 1.2: Theorized process for salient formation

Studies describing wave field modification around borrow sites have mainly focused on the effects of refraction and diffraction. However, wave energy reflected by these features may be significant, given the right combination wave of conditions

and pit geometries. The reflected waves might also contribute toward generating the alongshore non-uniform of wave energy at the shoreline which has been theorized to form EHS. Therefore, it is important to determine the significance and role in the nearshore process in order to fully understand the problem. Having the ability to quantify the amount of reflection that occurs for practical pit geometries will allow the direct effects of this to be known. Regardless of the consequences near the shoreline, the presence of reflection near the borrow pit is important especially for navigation purposes. Therefore practical design guidance may be given toward reducing the disruption in the wave climate near the anomaly and possibly the undesired affects on the shoreline.

1.1.1 Introduction of parameters

There are limited case studies regarding the effects of offshore borrow sites. However, from the few that exist, a general sense about the pit shape and geometry may be inferred as a prototype for future applications. Studies have also been performed for field cases with the aid of numerical models. Through this route, engineers attempt to estimate the potential impacts of dredging by inputting the proposed borrow pit geometry and wave conditions for the site. Therefore, these studies also provide a sense in the practical dimensions of borrow sites. In addition, in efforts to isolate the direct influence of a borrow site on the shoreline laboratory experiments have been performed. Comparing the dimensionless properties of the borrow pit to those of the field cases also may be important if trends in the resulting wave patterns and/or shoreline morphology are similar.

Intuitively, the parameters which will most significantly affect the wave field modification around a borrow site are the water depth inside (h_3) and outside (h_1) the borrow pit. Additionally, the horizontal physical pit dimensions such as the cross-shore width (a), longshore length (b), borrow pit sidewall slopes (S), and distance offshore (x_{pit}) will determine the extent and magnitude of its influence on the wave pattern. The incident wave conditions (i.e. wave height H, period T, and direction θ) will also have an impact on the wave transformation. However, the frequency of the

wave is most influential, since this controls the resonance conditions inside the pit. As a reference, Tables 1.1 to 1.3 (on pages 20 and 21 of this document) list of all the important dimensional and dimensionless parameters used to represent the geometry, placement, and wave conditions for each site studied.

1.2 Review of borrow pit/nearshore trench studies

1.2.1 Review of field cases and their effects on shoreline response

The Grand Isle, LA project was conducted by the U.S. Army Corps of Engineers (USACE) New Orleans District. Approximately 4.2 million m^3 of sand was dredged from a distance x_{pit} = 800 m offshore. The dredge area consisted of a dumbbell shaped feature. The depth below the seabed was approximately 6 m in each of the bells and 3 m in the center bar shaped channel connecting the bells. Combe and Soileau (1987) document the evolution of the shoreline over the course of the two years following project completion. During 1985 three hurricanes struck the coast and were credited toward significantly modifying the shoreline into the cuspate shape shown in Figure 1.1. The authors note that the "shadowing" effects from the borrow site on the wave field were clearly visible through aerial photography. This gave qualitative evidence that the modified wave field played a role in the shoreline evolution trends witnessed. Gravens and Rosati (1994) later simulated the case using the RCPWAVE wave propagation model coupled with the GENESIS model. They found that the model was unable to predict the documented trends in shoreline evolution without using unusually high empirical coefficients within the model formulation.

Kojima et al. (1986) investigated the cross-shore beach profile evolution near five offshore borrow sites located in the Genkai Sea, Japan. The sites studied were located in a water depth ranging from 15 to 20 m located within a range of 500 to 1500 m offshore. The purpose of the study was to examine correlations between offshore dredging and shoreline erosion. Sediment tracers were used to document the change in the profile shape for each borrow site. As seen in Figure 1.3, the dimensions of the borrow pits are mostly rectangular in shape with the longshore

dimension being slightly greater than the cross-shore dimension. Although the erosional effects were mainly attributed to an abnormally high frequency of destructive storms, the authors believe that sand filling into the borrow pits from the shoreward side contributed toward some of the erosion. It was concluded that borrow sites situated in water depths larger than 35 m maintained their cross-shore profile shape with minimal sand infilling.

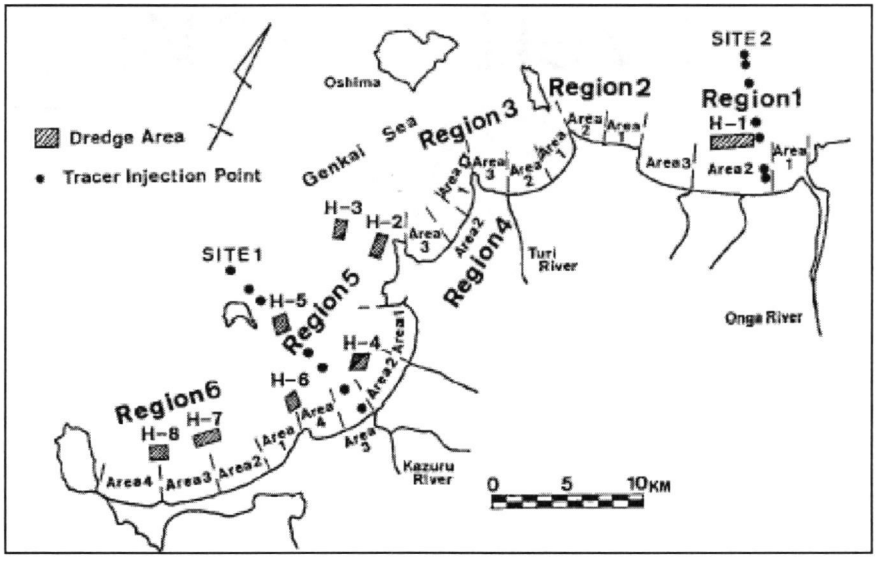

Figure 1.3: Location of borrow sites investigated at Genkai Sea, Japan (from Kojima et al. 1986)

Van Dolah et al. (1998) documents the infilling rates of five offshore borrow site locations off the coast of South Carolina and one dredge site near the Folly River mouth (illustrated in Figure 1.4). It was determined that the average refilling rate for the borrow areas in this region was 6.8 years. Near Hilton Head Island, borrow sites were dredged during the spring and summer of 1989-1990 from two offshore shoals: Gaskin Bank and Joiner Bank. The shoals were situated approximately 3.3 km and 2.4 km offshore respectively. Approximately 1.8 x 10^6 m^3 and 1.3 x 10^6 m^3 of sediment was dredged from each site. Other offshore borrow sites at Edisto Island (spring 1995), Hunting Island (spring 1991), and Seabrook Island (spring 1990) were documented. Approximately 0.2 x 10^6 m^3, 0.8 x 10^6 m^3, and roughly 0.1 x 10^6 m^3 were dredged from each respective site. However, little information about the actual borrow

site dimensions or bathymetric contours surrounding the feature were known prior to dredging. Therefore, approximate pit dimensions and locations of the dredge sites offshore were made through the aid of post-dredging surveys included in the authors report. The wave conditions for all of the sites were not reported; thus WIS hindcast data for the location during the time period of dredging can be used to determine the parameters listed in Table 1.1. The wave condition most influential on the wave field are taken as the largest wave period occurring during the year of dredging. Long wave conditions often create situations where wave reflection is prominent. Additionally, these conditions often correspond to storm wave conditions where significant erosion was documented.

Dean et al. (1999) documents another borrow site located at Anna Maria Key, FL during 1993. Approximately 1.6 million m^3 of sand was dredged from a distance ranging from 490 to 790 m offshore in a water depth of 6 m. The shape of the borrow site was rectangular with dimensions of 3050 m in the longshore, 340 m in the cross-shore, and 3.1 m below the seabed. Changes in the profile shape were documented pre-project and post-project; Figure 1.5 illustrates an area of significant erosion directly in lee of the borrow site which grew each year following the year of 1995 when Hurricanes Erin and Opal occurred. The area of erosion directly in lee of the borrow site represents the inverse of which occurred in Grand Isle, LA. This may imply that there exist pit configurations that are capable of producing different shoreline evolution trends, or that the shoreline evolution trends are highly dependent on specific site conditions and case to case generalizations about the process cannot be made.

Gravens (1997) and Fernandez (1999) document a beach nourishment project at Delray Beach, FL. The nourishment site has been part of an ongoing project since 1973. Thus, there have been multiple dredges throughout the time period of 1973-2000. In 1997, the borrow site was located approximately 760 m offshore in a water depth of 16 m. The shape of the borrow site is rectangular with dimensions of 2740 m in the longshore, 300 m in the cross-shore, and ranged from 2 to 3 m in depth below the surrounding seabed. However, there existed a 300 m longshore break in the

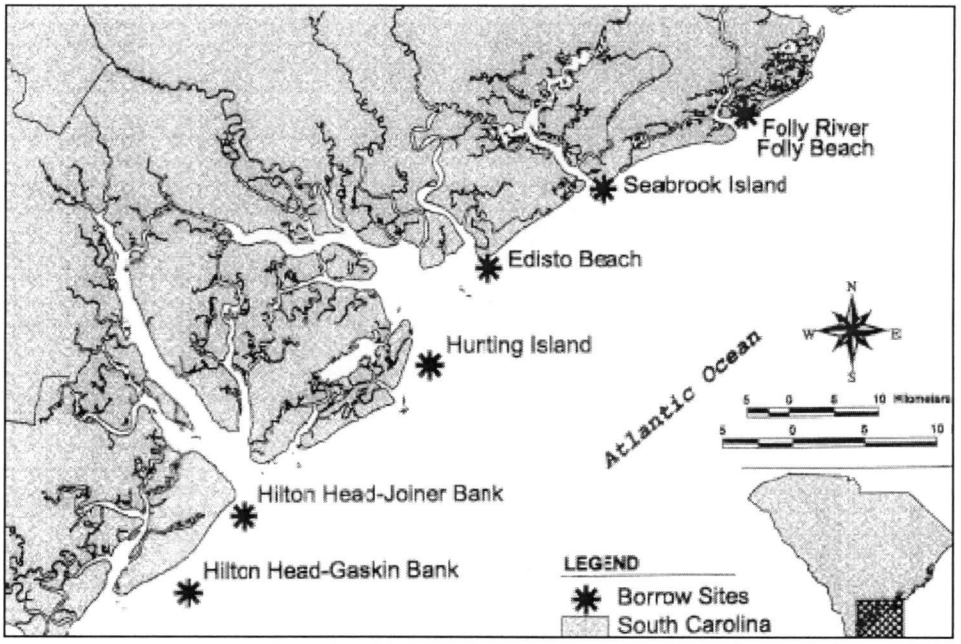

Figure 1.4: Location of borrow sites off the coast of South Carolina (from Van Dolah 1998)

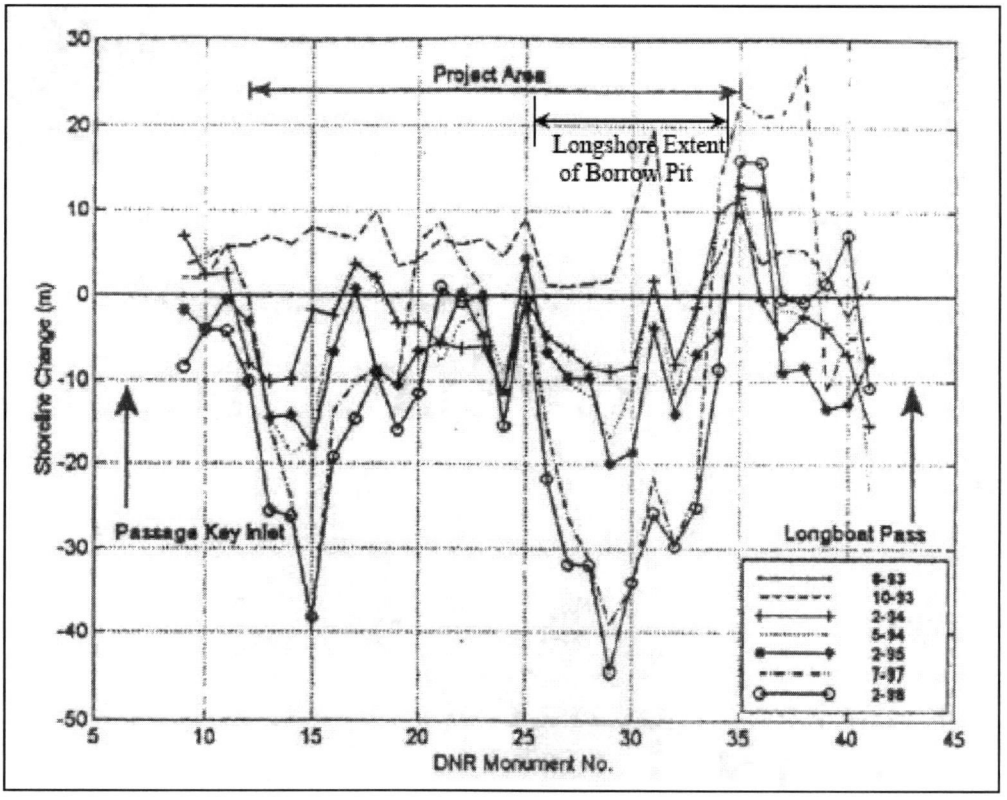

Figure 1.5: Documented shoreline change after beach nourishment at Anna Maria Key, FL where + = accretion (from Bender, 2003)

rectangular area due to a sewage outfall pipe where dredging did not take place as illustrated in Figure 1.6. This break in the borrow area was shown to correspond to an erosional hot spot on the shoreline. Therefore, the shape of the pit was somewhat more complex than other sites investigated. Nevertheless, localized erosion adjacent to the longshore edges of the borrow pit showed similar effects as those witnessed in Grand Isle, LA.

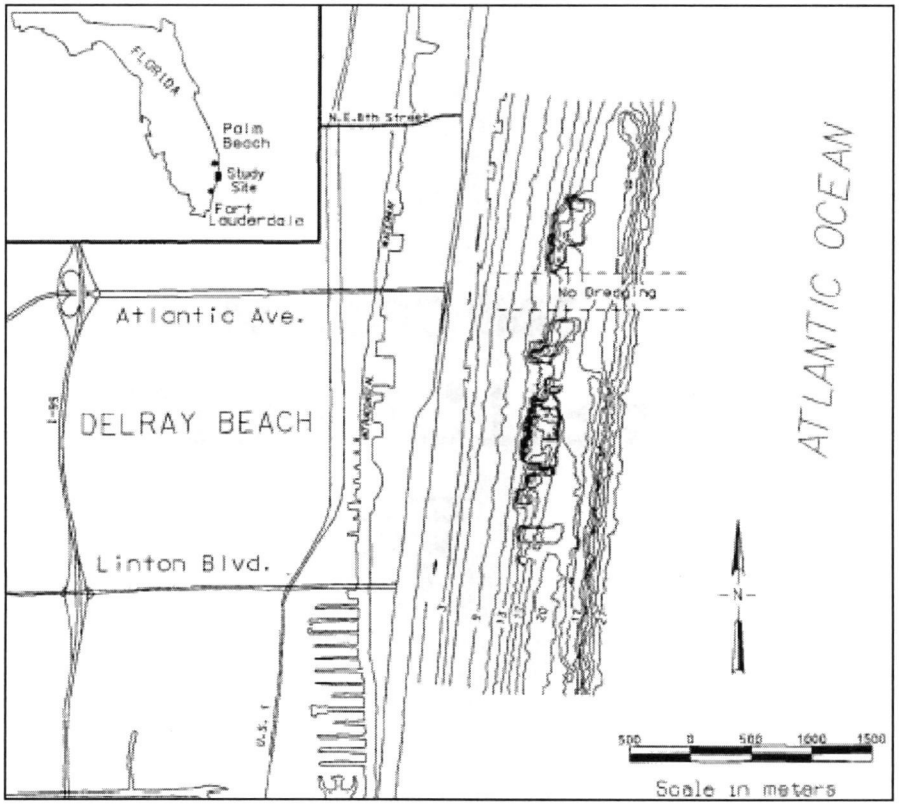

Figure 1.6: Borrow location offshore of Delray Beach, FL (from Gravens, 1997)

Another interesting case where wave field modification may be comparable to the case on an offshore borrow site are the La Jolla and Scripps canyons recently studied as part of the Nearshore Canyon Experiment (NCEX, 2003). The same questions regarding the impact of the wave transformation process on the nearshore circulation and shoreline morphology is presently being studied by multiple coastal engineers and scientists. The two canyons are located within the nearshore region with water depths outside and inside the trench being approximately h_1 = 40 m, h_2 =

175 m for Scripps canyon and $h_1 = 50$, $h_2 = 220$ m for La Jolla canyon. Additionally, the width of Scripps canyon is narrower than La Jolla canyon and hence, has steeper sidewall slopes. The bathymetry for the area is publicly available through the Coastal Data Information Program (CDIP) website. The bathymetry is shown in Figure 1.7; the grid was originally created by Mark Orzech at NPS. Approximate dimensions for the trenches are found using this data. Thereafter, the same dimensionless parameters as in the offshore borrow pit case are calculated, and are also listed in Table 1.1.

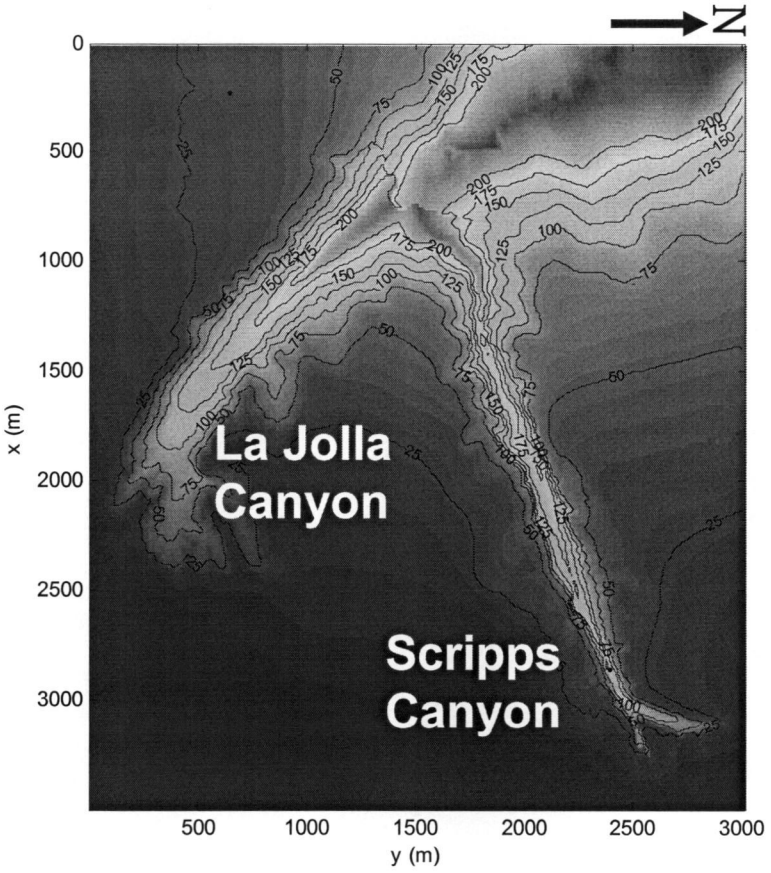

Figure 1.7: Bathymetry for NCEX trenches (data from CDIP)

Again the wave conditions are given for long wave conditions (or the ones most prone to generate a large amount of reflection). This is for the case when waves propagate directly perpendicular (or normally incident) to the two trenches. Approximate wave directions using a meteorological convention are $\theta = 226.4°$ for La Jolla and $\theta = 333.8°$ for Scripps (where true north is $\theta = 0°$). Typical swell periods for both canyons

is approximately T = 17 s. Significant changes in nearshore circulation have been known to occur as a result of the complex wave patterns around the trenches for wave conditions similar these (Long et al. 2003).

1.2.2 Review of laboratory studies

Horikawa (1977) performed an experiment in a small 6 m x 1.2 m (cross-shore x longshore) wave basin at the University of Tokyo to investigate the shoreline response from a small rectangular pit located in the active profile. A schematic of the experiment is shown in Figure 1.8. The pit was initially covered for the time period of 5.5 hours as waves were to allowed to stabilize the beach to equilibrium. Thereafter, the pit was uncovered and shoreline positions were measured following the 1, 2, and 3 hour marks after initiation of wave action. Table 1.2 lists the pit parameters and the incident wave conditions used in the experiment. Longshore measurements in wave height were also recorded at longshore transects both seaward and leeward of the pit. In the transect leeward of the pit, an area of low setup was witnessed directly behind the pit; additionally, this region was surrounded by two areas of high setup. The shoreline response consisted of the formation of a salient feature with the largest amount of accretion occurring at the centerline of the pit.

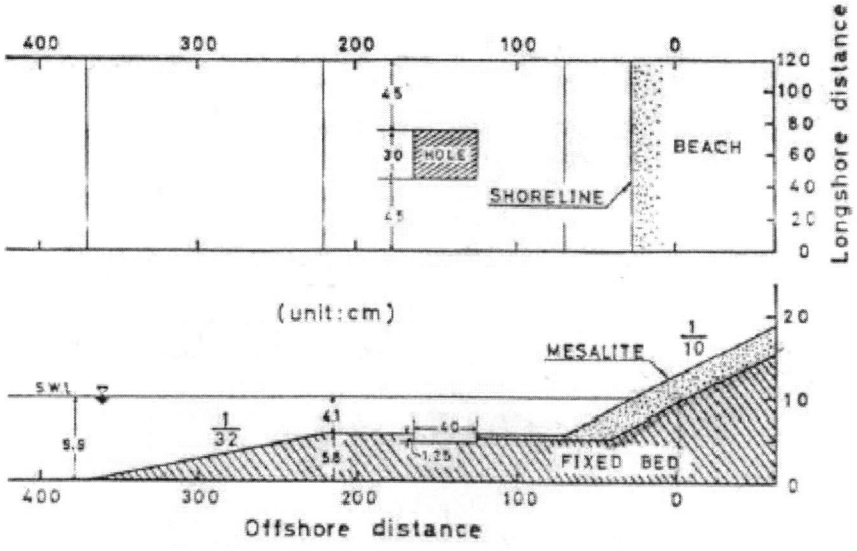

Figure 1.8: Experimental setup in wave basin (from Horikawa et al. 1977)

Williams (2002) performed a larger scale version of the experiment done by Horikawa et al. (1977). It was believed that the sidewall effects in Horikawa's experiment might have affected the shoreline response. The experiment was performed in a 15 m x 3 m (cross-shore x longshore) wave basin with a piston type wavemaker at the Coastal Engineering Laboratory at the University of Florida. The experimental setup is illustrated in Figure 1.9. The pit dimensions and wave conditions for the experiment are listed in Table 1.2. The experiment was conducted covering the pit for the first 6 hours (e.g. Horikawa et al 1977) and then uncovering the pit for the following 6 hours. For the case of the covered pit the shoreline receded directly behind the pit and was surrounded by to areas of accretion near the sidewalls. However when the pit was uncovered, shoreline advancement resulted with maximum accretion very close to the pit centerline and two areas of recession developed near the sidewalls. Two baselines (x_{pit} = 1.6 m and x_{pit} = 2 m) denoting the initial shoreline position from the leeward pit edge were also tested to investigate how the proximity of the pit to the shoreline affects the magnitude of shoreline advancement/recession. It was determined that relocating the shoreline further from the borrow pit did not have any significant affects on the magnitude or longshore limits of shoreline change.

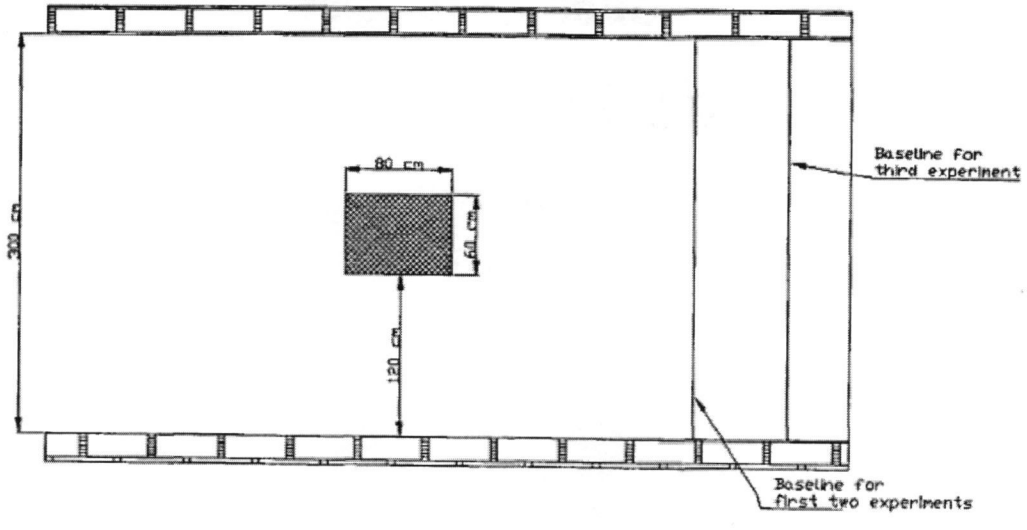

Figure 1.9: Experimental setup in large wave basin (from Williams 2002)

1.2.3 Review of model studies

Often times a general sense of how the shoreline will respond is required for areas being considered for offshore borrow material. In such cases, both mathematical and numerical models have been used to calculate the modified wave field around the proposed features. Wave predictions are then used to drive a shoreline evolution model. One common shoreline evolution model called a one-line model is often used. This model is based on a form of the diffusion equation given by Pelnard-Considère (1956) to calculate shoreline position over a specified amount of time. A general form of this equation is

$$\frac{\partial x}{\partial t} = \frac{1}{h_* + B}\frac{\partial Q_{sed}}{\partial y} \tag{1.1}$$

where x is the cross-shore position, y is the longshore coordinate, t is time, Q_{sed} is the longshore sediment transport, B is the berm height, and h_* is the depth of closure. There exist many slightly different equations for calculating the longshore sediment transport rate; however in these studies two have generally been used. The first is equivalent to the modified Scripps formula by Komar (1969) which was later adopted as the CERC formula in the Shore Protection Manual (1984). The second formulation follows Ozasa and Brampton (1979) and Gourlay (1982) and includes an additional term proportional to the longshore gradient in breaking wave $\partial H_b/\partial y$. The relations for each, respectively, are

$$Q_{sed} = \frac{K_1 H_b^{2.5}\sqrt{g/\kappa}\sin 2\alpha_b}{16(s-1)(1-p)} \tag{1.2}$$

$$Q_{sed} = \frac{K_1 H_b^{2.5}\sqrt{g/\kappa}\sin 2\alpha_b}{16(s-1)(1-p)} - \frac{K_2 H_b^{2}\sqrt{g/\kappa}\cos\alpha_b}{8(s-1)(p-1)\tan\beta}\cdot\frac{\partial H_b}{\partial y} \tag{1.3}$$

where K_1 and K_2 are empirical coefficients; H_b is the wave height at breaking; κ is the breaker index; α_b is the wave angle at breaking relative to the shoreline ($\alpha_b = \theta_b - \gamma$); θ_b

indicating the wave direction from the x-axis, and γ indicating the angle of shore normal from the x-axis; s is specific gravity of sand; p is the sand porosity; and $\tan\beta$ is the nearshore slope.

The first application of this form was for a proposed dredging site near Great Yarmouth, Great Britain. Moytaka and Willis (1974) and Price et al. (1978) used a mathematical refraction model to calculate the wave field around an idealized rectangular borrow site in order to drive their shoreline response model. The purpose of their study was to locate a minimal water depth for dredging that did not significantly impact the shoreline evolution trend. Figure 1.10 illustrates that dredge sites located in relatively shallow water affect the shoreline response more significantly than sites located in waters of larger depth. This is a direct result of increased wave scattering due to bottom features as the water depth decreases. In deeper water waves are less affected by the bathymetry, therefore the modification to the wave field is less substantial which in turn limits the impacts on the shoreline. Moytaka and Willis (1974) determined that dredging should not take place in a water depth shallower than the 18 m contour. Later, Price et al (1978) changed this restriction to 14 m. It was additionally shown that both increasing the water depth inside the borrow pit and increasing the longshore pit length will generate larger erosive trends according to the shoreline evolution model. The relation for the longshore sediment transport in their model is based on equation (1.2).

Similarly, Horikawa et al. (1977) used a mathematical refraction model to investigate the impacts of a rectangular shaped borrow site off the coast of Eastern Japan. A range of incident wave conditions, relative pit depths, and pit width/lengths were used in their study to test the sensitivity on the predicted amount of accretion or erosion associated with an initially straight shoreline. One of the main conclusions was that increasing the longshore length b of the pit results in larger magnitudes of accretion and erosion. The study also uses the CERC formulation given by equation (1.2).

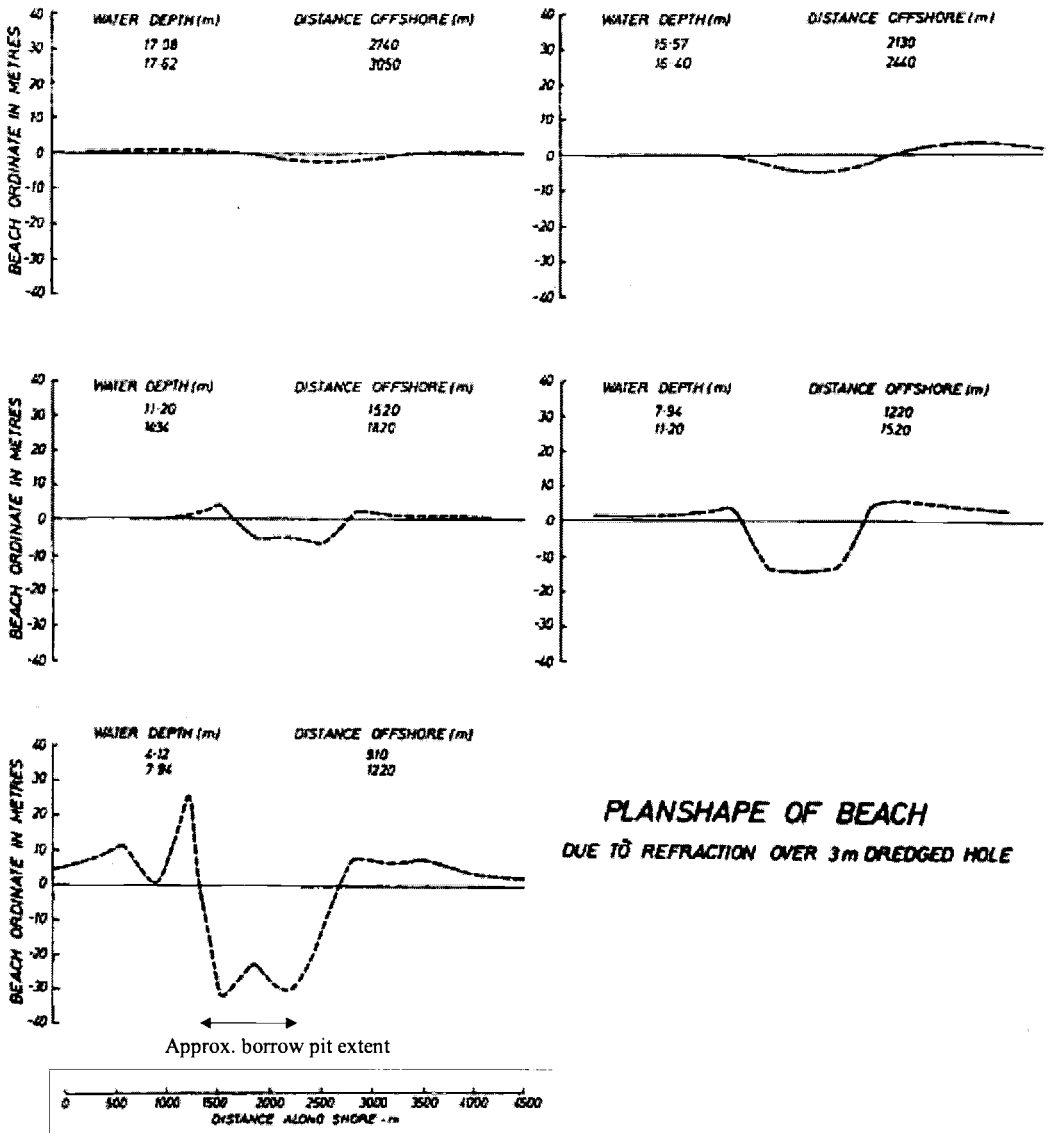

Figure 1.10: Dependency of water depth surrounding borrow site on shoreline response (modified from Moytaka and Willis 1974)

For the previous two studies, cell discretization was very coarse (Δx = 176m and Δx = 250m respectively). This limited the investigation to only rectangular borrow shapes with sidewall slopes unable to exceed a value given by the trench depth to cell size ratio. In Figure 1.10, Moytaka and Willis (1974) illustrate an area of erosion directly shoreward to the pit centerline surrounded by two areas of accretion, whereas Horikawa et al. (1977) show an area of accretion adjacent to the pit centerline surrounded by two areas of erosion.

In a more recent study, Bender and Dean (2001) use a mathematical model that includes the effects of refraction, diffraction, and reflection to determine the wave field surrounding a cylindrical pit of constant depth. It is shown that the relative pit dimensions (and/or incident wave period) play an important role in the amount of reflection generated behind the pit as illustrated by Figure 1.11; over 25% of the wave energy is being reflected at the largest peak. Furthermore, shoreline response was calculated using a different one-line model than used by Moytaka and Willis (1974) and Horikawa (1977). Instead the formulation follows that of Ozasa and Brampton (1979) or equation (1.3). By isolating the effects of each term in the sediment transport relation Q_{sed} on shoreline response, it was shown that the two terms actually have opposing properties. As shown in Figure 1.12 the first term (i.e. CERC formulation) will have a net effect toward generating erosion in lee of the pit surrounded by two areas of accretion; whereas the second term creates an area of accretion surrounded by two spots of erosion. Therefore the resultant shoreline response will depend on the weighting of each term (i.e. the magnitude of each empirical coefficient K_1 and K_2).

In recent years computing efficiency has increased significantly and numerical models have been extensively employed to simulate wave transformation over proposed borrow pits. Many of these models use Berkhoff's (1972) mild-slope equation (MSE) that allows for the effects of refraction and diffraction to be considered simultaneously. Radder (1979) developed a parabolic approximation to the MSE allowing for a less computationally intensive solution technique. The process involves splitting the wave field into transmitted and reflected components and neglecting the reflected component. The parabolic approximation governs models such as REF/DIF (e.g. Kirby and Dalrymple, 1994) and RCPWAVE (e.g. Ebersole et al. 1986).

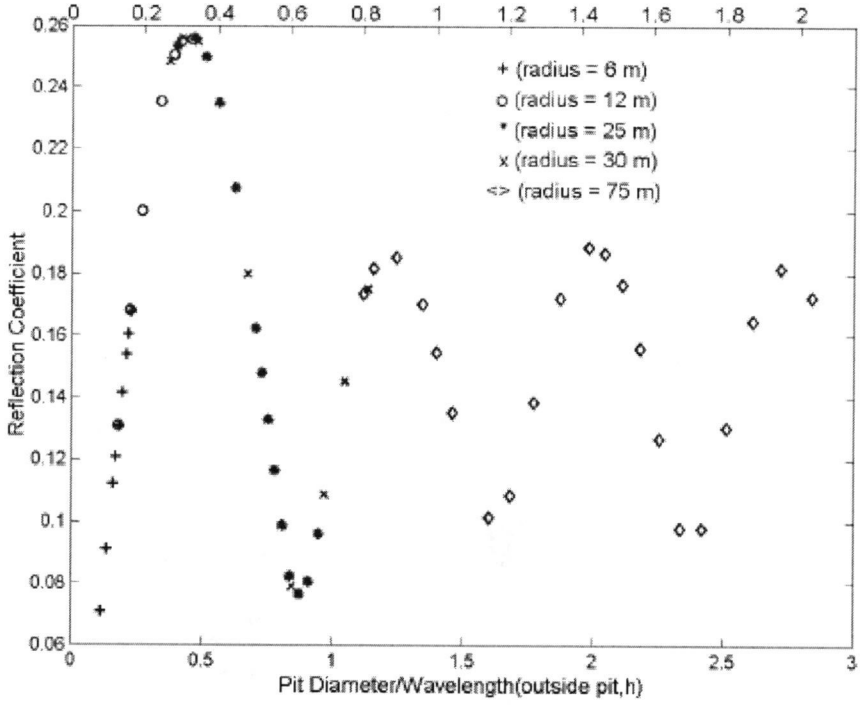

Figure 1.11: Wave reflection associated with a cylindrical pit as a function of relative pit diameter (from Bender 2003)

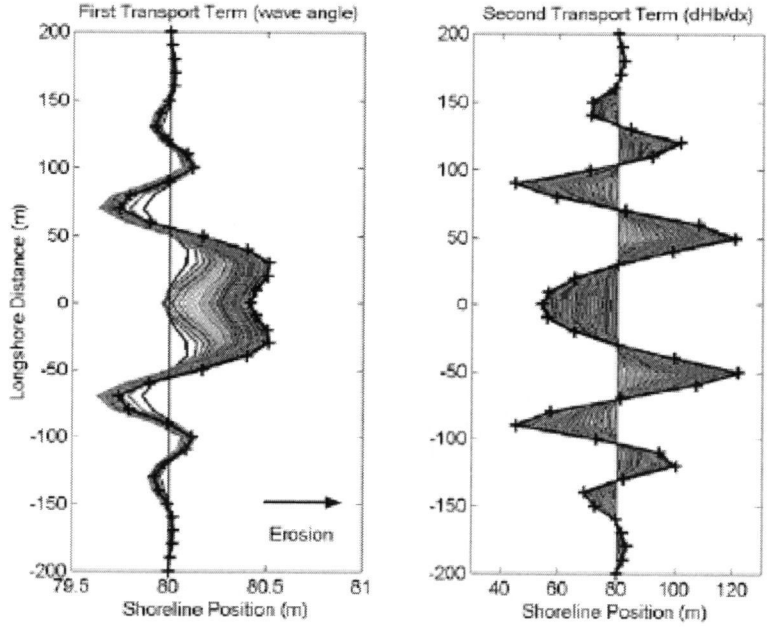

Figure 1.12: Example of the contribution of each sediment transport term on the resultant shoreline response (from Bender 2003)

Maa and Hobbs (1998) and Maa et al. (2001) investigated the potential effects of an offshore borrow site near Virginia Beach, VA. The proposed borrow site was a shoal located approximately 5 km offshore at a water depth ranging from 12 to 15 m. The important concept regarding the impact of the incident wave conditions on the modifications to the wave field is recognized: It is stated that wave refraction, diffraction, and reflection will be most significant for large waves with long periods or where the relative water depth *kh* is located near the shallow water limit. Therefore incident waves characterized by these qualities were used in the analysis. However in order to describe the wave transformation, Maa (1998) employs the RCPWAVE wave propagation model. Thus, even though wave reflection may be important for these wave conditions, its effects are being neglected in this study. Nevertheless, a shoreline evolution model following the formulation of Gourlay (1982) (i.e. eqn. 1.3) was applied to determine the impact on shoreline evolution. Based on the hypothesis that the magnitude of the longshore gradient in wave height will control the magnitude of the longshore sediment transport rate, a parameter named the Breaking Height Modulation (BHM) was devised to quantify the potential for shoreline erosion. Using the BHM, it was possible to quantitatively compare the level of impact on the shoreline for multiple dredge scenarios. Ultimately, the effects of the proposed borrow site was determined to be negligible and permission was granted for dredging at the site.

Other studies (e.g. Work et al. 2003, and Demir et al. 2004) argue that the use of wave propagation models capable of accounting for random wave patterns and wave-wave interactions results in predictions that are more representative of the conditions witnessed in the field. Demir et al. (2004) studied the potential effects of dredge holes in the Black Sea near Kilyos, Turkey, whereas Work et al. (2004) investigated an area near Folly Island, South Carolina. In both cases the SWAN model by Booij (1999) was used; SWAN is a spectral wave transformation model that accounts for shoaling and refraction of random waves. Additionally, energy transfers by means of bottom friction, wind, breaking, and wave-wave interaction may be included. However, the model neglects the effects of wave diffraction and reflection. In both studies the SWAN model is driven using hindcast data for the appropriate area.

Demir et al. (2004) suggests that the use of a long thin pit, with tapered sidewall slopes and placement of the pit in relatively deep water will minimize the indirect effects on the shoreline. Both studies predict the resultant shoreline response generated by a generic rectangular shaped borrow site using a one-line model. Demir et al. (2004) used the formulation according to Ozasa and Brampton (1979) while Work et al. (2003) used the standard CERC formula.

Most recently, Kelley et al. (2004) composed a semi-quantitative methodology to determine the potential impacts of borrow sites on a shoreline also using a coupled wave propagation/shoreline response model. The analyzed historical shoreline change data for specific sites as well as temporal changes in the wave climate. Additionally, hindcast data is used to drive another spectral wave model STWAVE (e.g. Smith et al. 2001). By computing the temporal component of sediment transport Q_{sed} (i.e. at different time periods in the hindcast record) following the CERC formula, a mean μ and a standard deviation σ of the temporal longshore sediment transport is calculated. This information is used as a gage toward estimating the natural changes in sediment transport over a designated time period. Through the same methodology, when a borrow site is introduced, a new sediment transport will be calculated over the same section of beach. If the new sediment transport exceeds a threshold of ($\pm 0.5\sigma$) about the mean of the previous temporal sediment transport, the borrow site was determined to significantly interfere with the natural fluctuations in sediment transport. Thus a standard for determining the potential side effects in the implementation of the borrow site can be issued.

Table 1.1: Relevant parameters describing incident wave conditions and geometry for each borrow pit/nearshore canyon case

Field Cases	Wave conditions				Dimensional pit characteristics				Dimensionless pit parameters				
	h_1 (m)	H_s (m)	T (s)	Θ (deg)	b (m)	a (m)	h_2 (m)	x_{pit} (km)	k_1h_1	k_2h_2	$\bar{a}/\lambda_1$	b/λ_1	$\tan\beta$
(1) Genkai Sea, Japan † Kojima et al. (1986)	13 ~ 20	4.0	9.0	-45 ~ 0	1000 ~ 3000	1000	16 ~ 25	0.5 ~ 1.5	0.901 ~ 1.195	1.028 ~ 1.403	9.5 ~ 11	9.5 ~ 33	0.03
(2) Grand Isle, LA (1983) ‡ Combe & Soileau (1987) Gravens & Rosati (1994)	4.6	0.56	14.0	18	1370	460	7.7 ~ 10.7	0.8	0.312	0.408 ~ 0.487	5.0	14.8	0.01
(3) Anna Maria Key, FL (1993) ‡ Dean et al. (1999)	6.0	4.4	11.1	-4	3050	340	9.1	0.5 ~ 0.8	0.458	0.574	4.0	37.0	0.02
(4) Delray Beach, FL (1973-99) ‡ Fernandez (1999)	16	2.4	15	-47	2740	300	19	0.8	0.562	0.618	1.7	15.3	0.02
(5) Gaskin Banks, SC (1990) ‡ Van Dolah et al. (1998)	3.1	1.2	14.0	38	600	1200	6.1	3.3	0.255	0.362	15.7	7.9	0.001
(6) Joiner Banks, SC (1991) ‡ Van Dolah et al. (1998)	2.4	1.1	14.0	26	1400	500	5.5	2.4	0.224	0.343	7.4	20.8	0.001
(7) Edisto Island, SC (1995) ‡ Van Dolah et al. (1998)	3.0	4.3	16.0	16	400	200	6.4	1.0	0.219	0.323	2.3	4.6	0.003
(8) Hunting Island, SC (1991) ‡ Van Dolah et al. (1998)	3.7	2.7	11.0	-15	600	300	8.0	2.1	0.358	0.540	4.6	9.2	0.002
(9) Seabrook Island, SC (1990) ‡ Van Dolah et al. (1998)	3.0	1.2	14.0	50	600	200	4.6	0.1	0.251	0.312	2.7	8.0	0.03
(10) Scripps Canyon (NCEX) §	40	1.0	17.0	⊥ to trench	1300	140	175	1.0	0.823	2.473	0.5	4.3	0.01
(11) La Jolla Canyon (NCEX) §	50	1.0	17.0	⊥ to trench	2100	300	220	2.0	0.945	3.077	0.9	6.3	0.01

† there exists five borrow sites therefore the lower and upper bounds of each parameter are expressed; wave conditions represent probable storm conditions
‡ wave data obtained from WIS hindcast during project year or when documented erosion occurred; correspond to storm wave conditions (i.e. T_{max})
§ Approximate trench dimensions from CDIP bathymetry and NCEX website; Wave conditions represent long period swells

(where b = longshore pit length, a = cross-shore pit width, h_1 = depth outside of pit; h_2 = depth inside pit; x_{pit} = distance offshore from leeward pit edge; S_{max} = maximum sidewall slope of pit; $\tan\beta$ = beach slope; λ_1 = wavelength, H_s = wave height, T = wave period, θ = wave direction w.r.t. shore normal, + = clockwise)

Table 1.2: Relevant parameters describing incident wave conditions and geometry for borrow pits investigated in the laboratory

Laboratory Studies	Wave conditions				Dimensional pit characteristics				Dimensionless pit parameters					
	h_1 (m)	H (m)	T (s)	Θ (deg)	b (m)	a (m)	h_2 (m)	x_{pit} (m)	k_1h_1	k_2h_2	a/λ	b/λ	S_{max}	$\tan\beta$
(1) Horikawa et al. (1977)	0.041	0.013	0.412	0	0.3	0.4	0.0535	1.25	1.177	1.425	1.8	1.4	∞	0.100
(2) Williams (2000)	0.15	0.06	1.35	0	0.6	0.8	0.27	1.6 & 2.0	0.609	0.858	0.5	0.4	∞	0.111

Table 1.3: Relevant parameters in numerical models examining the impacts of potential borrow site locations

Simulated Field Cases	Wave conditions				Dimensional pit characteristics				Dimensionless pit parameters					
	h_1 (m)	H (m)	T (s)	Θ (deg)	b (m)	a (m)	h_2 (m)	x_{pit} (km)	k_1h_1	k_2h_2	a/λ	b/λ	S_{max}	$tan\beta$
(1) Great Yarmouth, G.B. † Moytaka & Willis (1974) Price et. al (1978)	4.1 ~ 17.6	0.4 ~ 2	5 ~ 8	-10 ~ 20	880	305	5.1 ~ 21.6	0.9 ~ 3.05	0.530 ~ 2.853	0.599 ~ 3.485	3.6 ~ 10.8	10.3 ~ 31.2	0.02	0.007
(2) Eastern Japan† Horikawa et al. (1977)	20 ~ 50	0.3 ~ 2.7	6 ~ 13	-22.5 ~ 22.5	2000 ~ 4000	2000	23 ~ 53	5 ~ 22	0.750 ~ 5.592	0.815 ~ 5.927	8.7 ~ 36.3	8.7 ~ 72.6	0.01	0.002
(3) Sandbridge Shoal, VA ‡ Maa & Hobbs (1998; 2001)	10	3.0	14	0	1500	500	12	3	0.469	0.519	3.7	11.2	0.07	0.003
(4) Kilyos, Turkey (Black Sea) Demir et al. (2003)	13	5	9.5	28	3300	1300	17	1	0.843	0.997	13.4	34.1	0.06	0.010
(5) Folly Island, SC Work et al. (2003)	8	1.6	5.6	0	1000	1000	9	3	1.222	1.329	24.3	24.3	?	0.002

† there exists multiple borrow site configurations and wave conditions, therefore the lower and upper limits of each parameter are expressed

‡ wave conditions correspond to a severe sea based on wave data description by author

The present study performs a rigorous set of tests on the MSE model using borrow pit shapes which violate the mild-slope criterion in order to determine whether the impacts are large enough to warrant the use of another model type. The significance of wave reflection will be studied in a similar fashion. A numerical wave model using a form of the modified mild-slope equation (MMSE) is employed. The MMSE was derived by Massel (1993) to correct for the inaccuracies witnessed in the original MSE for bottom slopes larger than 1:3. The model is formulated using a hyperbolic system of equations in the same fashion as Copeland (1985) used for the MSE. The present study uses the hyperbolic MMSE formulation as given by Lee et al. (1998) and Suh et al. (2001). Thus, the model is able to include wave reflection in addition to correcting the MSE's inaccuracy for bathymetric features with gradients in depth larger than 1:3.

Finally, in order to obtain an estimate of the shoreline response trends initiated from the modified wave field, results from the wave model are used to input to a common one-line model that is similar in nature to the GENESIS (Hanson and Kraus, 1989) model. The coupling of a wave model with a one-line model has been the typical methodology for describing the effects of borrow sites on shoreline response. However, the assumptions in the formulation of the one-line model make it hard to make firm conclusions about the potential effects of a borrow site. This is undoubtedly a result of the high degree of empiricism is involved in the sediment transport equation (i.e the selection of coefficients K_1 and K_2). One-line models also neglect the effects of flows initiated by MWL gradients, yet these flows may be an important part in accurately representing the sediment transport and in turn shoreline location. The significance of such MWL gradient flows is tested using a two-dimensional horizontal (2DH) circulation model that is driven using the steady-state wave conditions from the MMSE wave propagation model. In summary, this study seeks to provide a better assessment on whether the known limitations in standard methodologies significantly affect the predictions in the morphology of the shoreline.

2.0 One-dimensional methods and background

The simplest representation of a borrow site may be considered a trench that is infinitely long in the longshore direction; thus the dimensions considered in the problem consists of only one horizontal coordinate (cross-shore) in addition to the vertical coordinate. Solving an exact analytic solution or has typically been the approach for describing wave transmission over such obstacles. Dingemans (1997) provides an extensive overview of the different methods and solutions formulated.

2.1 Analytical solutions for a trench

Initial approaches for quantifying the amount of reflection that occurs in the presence of an obstacle have involved analytic solutions to the linear wave boundary value problem. The simplest of these solutions consist of long wave approximations to the boundary value problem. Lamb (Article 186, 1932) originally formulated a long wave approximation to calculate the amount of reflection generated from a wave propagating over an abrupt transition (i.e. finite step). Dean (1964) extended this formulation to a transition with a linear varying slope. Later, Miles (1967) constructed a plane-wave solution to approximate the amount of reflection for monochromatic waves propagating over a trench with vertically sloping sidewalls. The solution retains only the forward propagating waves in the solution, thus the effects of evanescent (or non-propagating) waves are not considered. Later, Kirby and Dalrymple (1983) modified this plane-wave solution to include the presence of obliquely incident waves. However, the approximation was shown to break down as the relative trench depth h_2/h_1 becomes large making its applicability limited to a small number of cases. In order to investigate the significance of sidewall slope, Bender (2003) developed a long wave formulation for a trench with linearly sloping sidewalls by placing two solutions following Dean (1964) back to back. This formulation allowed the study of trenches with features more similar to what is seen in the field. However, the main constraint with long wave solutions is that they only maintain accuracy within the shallow water regime (i.e. $kh < \pi/10$) where $k = 2\pi/\lambda$ is the wavenumber, λ is the wavelength and h is the local water depth. Yet, it can be argued

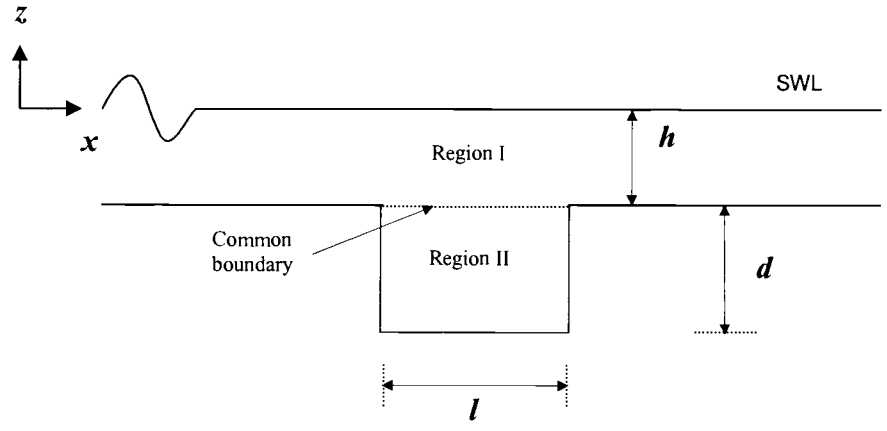

Figure 2.1: Definition sketch of domain used by Lee and Ayer (1981)

that borrow sites will only have significant impact on the wave field at small *kh*, so the approximation may be useful in some instances.

Another approach is to solve the full linear wave boundary value problem. This renders a solution that is accurate for all *kh*; but requires the solution to retain the non-propagating modes previously neglected in the long wave solutions. Lee and Ayer (1981) solve the boundary value problem for normally incident waves over a symmetric (i.e. water depth on either side equal) trench with vertical sidewall slopes. A set of matching conditions are applied along the common boundary as illustrated in Figure 2.1. Then the velocity potential for each region is solved numerically and the transmission (K_t) and reflection (K_r) coefficients are obtained. The amount of segments used to discretize the common boundary in addition to the number of evanescent modes retained in the truncated series controls the convergence of the solution. According to their definitions, *h* is the water depth outside the trench, *d* the deviation of the trench depth from the surrounding water depth, and *l* is the cross-shore width of the trench. Upon analysis of the trends in the reflection/transmission coefficient as a function of relative depth h/λ (where λ refers to the wavelength outside the pit) a series of conclusions were made. First, the effect of the trench is shown to become negligible as wave frequency increases. Second, as width $l \rightarrow 0.5\lambda_l$, only one significant peak exists in a plot of the reflection coefficient versus h/λ

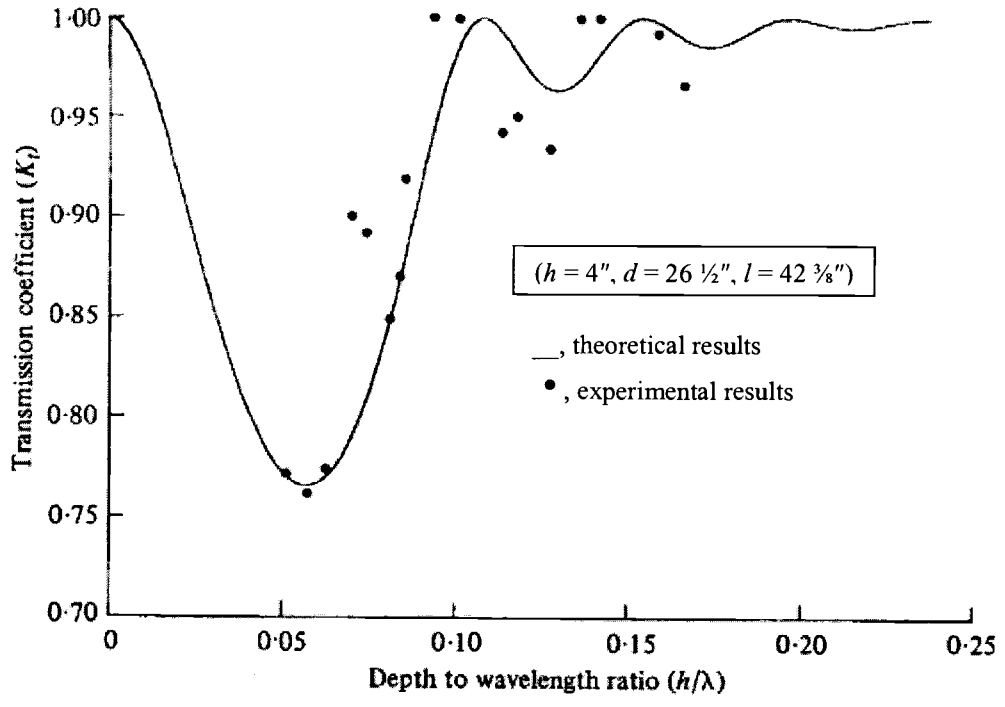

Figure 2.2: Transmission coefficient as a function of dimensionless water depth for trench width l = 42⅜″ (modified from Lee and Ayer 1981)

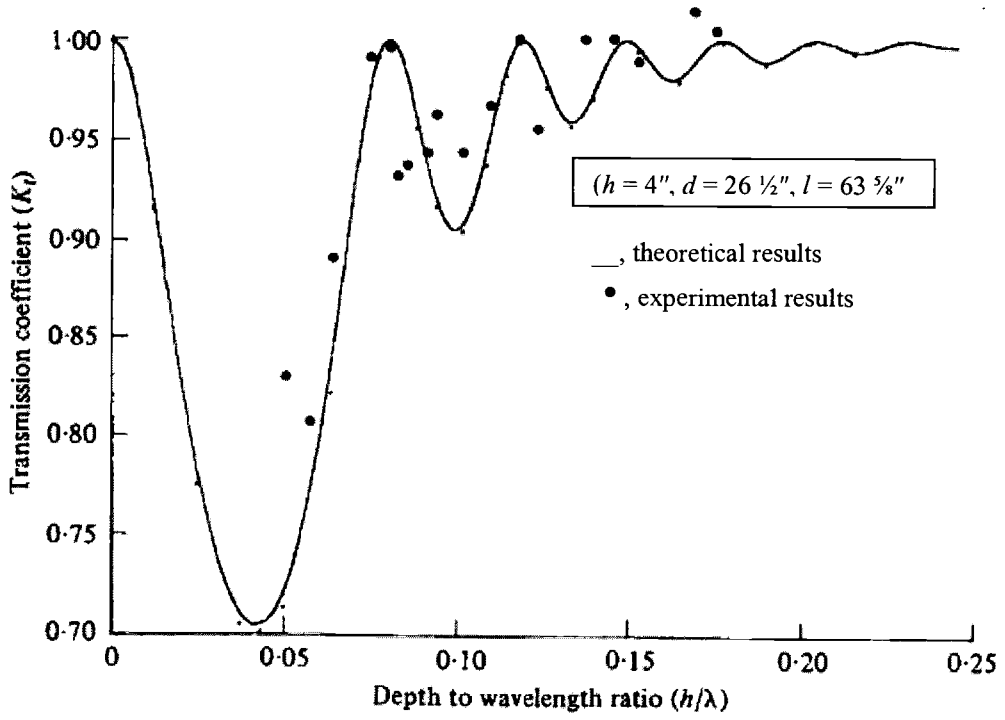

Figure 2.3: Transmission coefficient as a function of dimensionless water depth for trench width l = 63⅝″ (modified from Lee and Ayer 1981)

Conversely, as width l of the trench is increased, there exist more frequencies capable of producing reflection (i.e. peaks in K_r); however the magnitude of K_r decays as the frequency is increased. This effect is shown in Figures 2.2 and 2.3 as l is increased from 42⅜″ to 63⅝″.

Similarly, Takano (1960) solves the boundary value problem for normally incident, monochromatic waves over finite rectangular sill. A solution for a trench can be found through the modification of the boundary conditions and has since been the basis for many of the recent analytical solutions involving a trench. This solution technique involves constructing solutions for three regions as in Figure 2.4 (seaward of the trench, directly over trench, and leeward of trench). Eigenfunction expansions of the velocity potential for each sub region are constructed and matching conditions are applied at the two vertical boundaries separating each region; the solution is then solved numerically. Kirby and Dalrymple (1983) extend this methodology to include the influence of oblique incident waves and asymmetric trenches (i.e. $h_1 \neq h_3$). The effect of obliquely incident waves was shown to significantly reduce the transmittance of wave energy (or conversely increase the reflection) for specific combinations of wave frequency and trench width. This is demonstrated in Figure 2.5 which plots the transmission coefficient K_t versus relative water depth k_1h_1 for a normally incident wave and an obliquely incident wave (e.g. $\theta = 45°$).

Bender (2003) later extended this type of solution to solve for sloping trench sidewalls as illustrated in Figure 2.6. By representing a transition in depth though a series of steps, a sloping sidewall was approximated. The convergence of the solution is a function of the number of steps representing the slope in addition to the number of evanescent modes retained in the solution. It was concluded that the use of 10 steps and 16 evanescent modes was sufficient for transitions with slopes less than or equal to 1:1 (rise:run). Figure 2.7 illustrates that reflection is most prominent for steeply sloping trenches. The magnitude of K_r becomes substantially smaller as sidewall slope becomes milder and kh increases. For this comparison, the cross-sectional area of the trench, depth inside, and outside of the trench were all fixed. The figure also demonstrates how the number of peaks in K_r increases when the slope becomes milder

(or equivalently as the width of the pit at the top increases and the width at the bottom decreases).

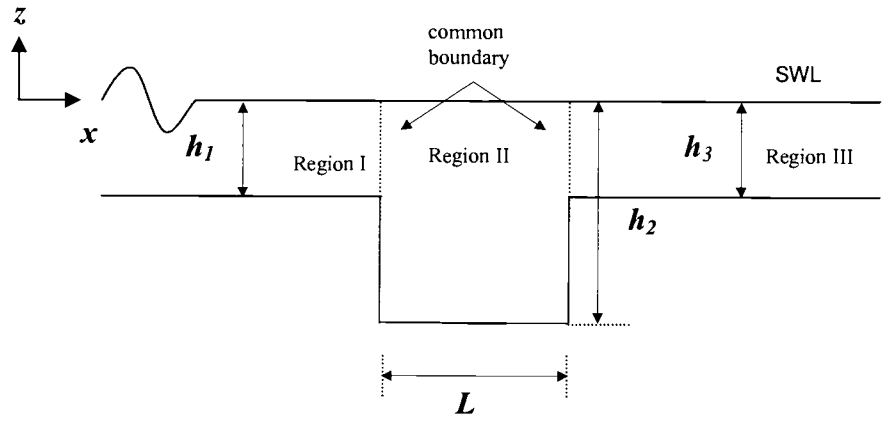

Figure 2.4: Definition sketch of domain used by Takano (1960) and Kirby and Dalrymple (1983)

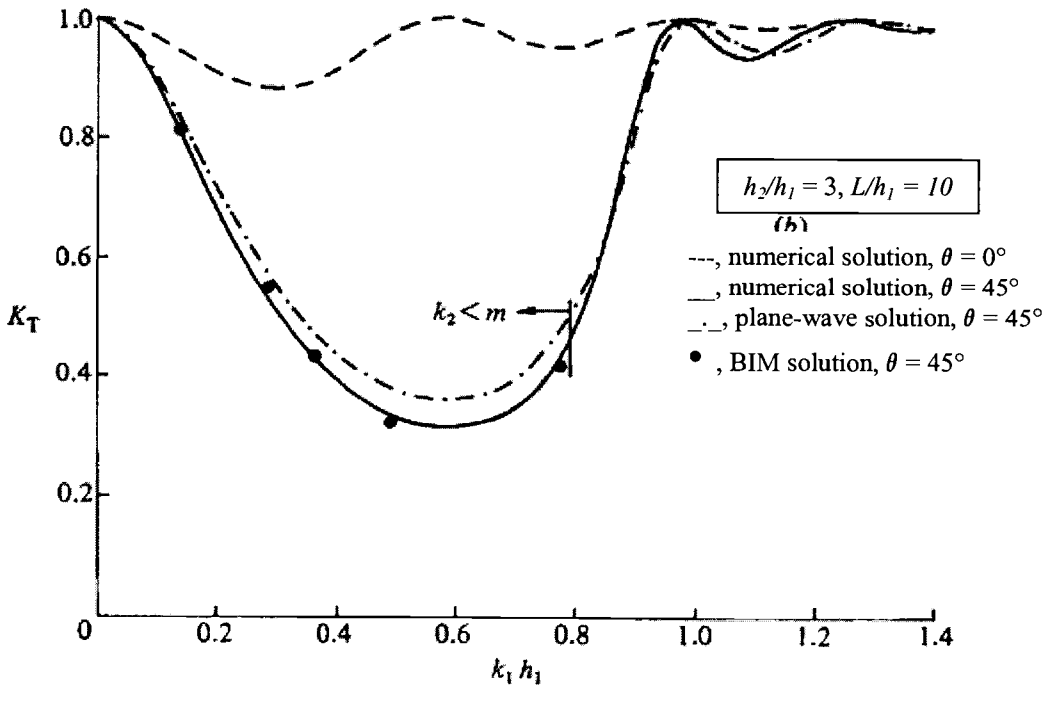

Figure 2.5: Transmission coefficient for normally incident waves, $\theta = 0°$; and obliquely incident waves, $\theta = 45°$ (modified from Kirby and Dalrymple 1983)

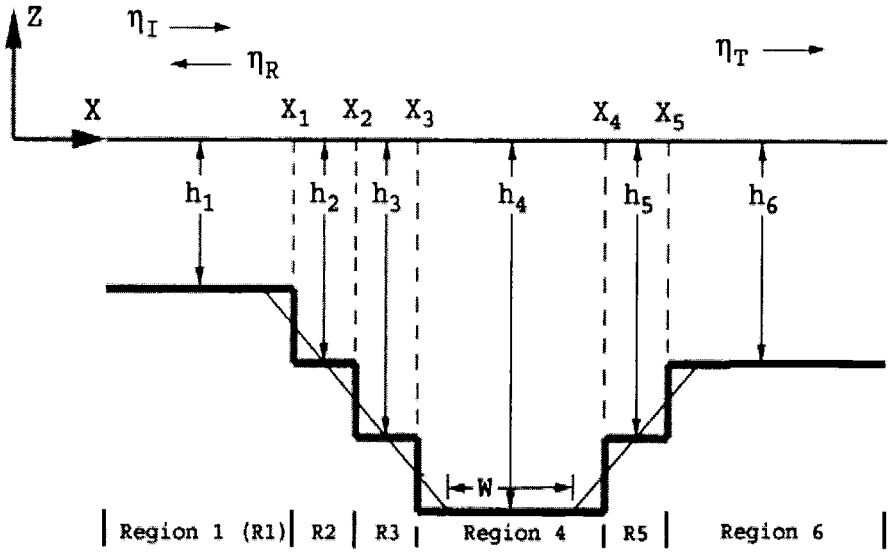

Figure 2.6: Definition sketch of trench with sloping sidewalls in Bender's (2003) step method (from Bender 2003)

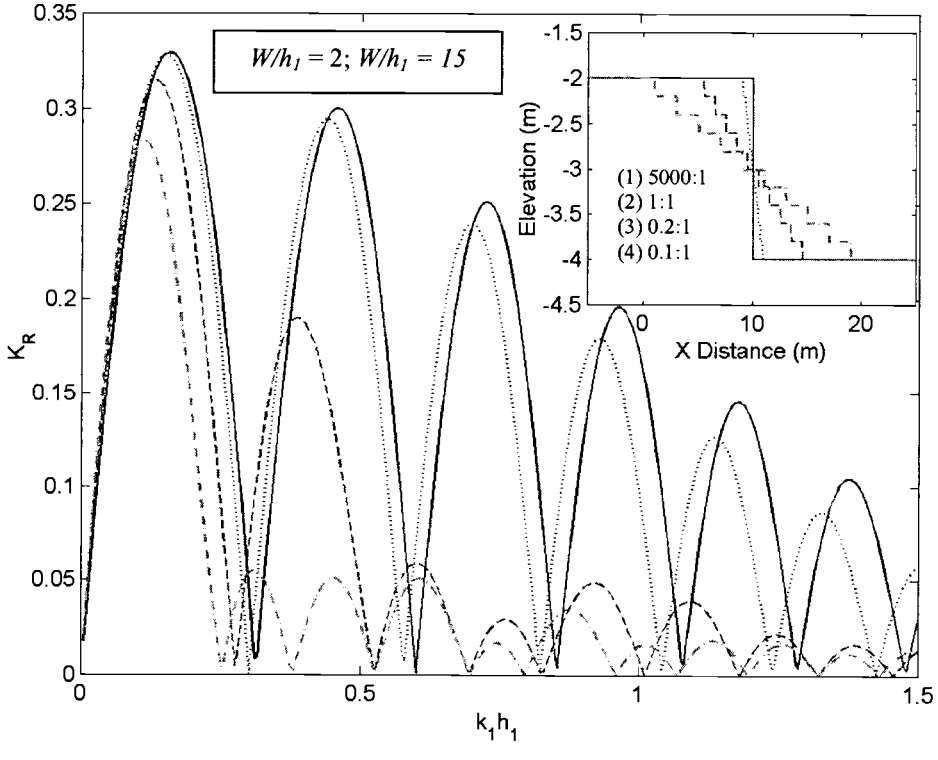

Figure 2.7: The effect of sidewall slope on the reflection coefficient (modified from Bender 2003)

2.2 The mild-slope equation for rapidly varying bathymetry

Analytical solutions provide great insight into the physics involved in wave propagation over anomalies with large gradients in depth such as trenches. However, the solutions require simplistic geometrical shapes and constant bathymetry surrounding the anomaly. Therefore, the numerical models have become an important tool for describing wave propagation over arbitrary bathymetry. Assuming an inviscid and incompressible fluid with irrotational motion, Berkhoff (1972) derived a simplification to the three-dimensional problem for progressive water waves propagating over an irregular bathymetry. Through vertical integration the three-dimensional problem is condensed into a two-dimensional refraction-diffraction equation. The resulting equation is commonly referred to as the mild-slope equation (MSE). The equation is elliptic in form and follows

$$\nabla \cdot (CC_g \nabla \tilde{\phi}) + \omega^2 \frac{C_g}{C} \tilde{\phi} = 0 \tag{2.1}$$

where $\tilde{\phi}$ is the complex velocity potential at the still water level and is related to the free-surface elevation η through

$$\tilde{\phi} = -\frac{ig}{\omega}\eta \tag{2.2}$$

and C the phase speed, C_g the group velocity, k the wavenumber, h the water depth, and ω the angular frequency related to k and h by the dispersion relation

$$\omega^2 = gk \tanh kh \tag{2.3}$$

However, the formulation makes the assumption of slowly varying topography or

$$\frac{\nabla_h h}{kh} << 1, \quad \nabla_h = \left\{ \frac{\partial h}{\partial x}, \frac{\partial h}{\partial y} \right\} \tag{2.4}$$

Booij (1983) later quantified this limit on the variation in depth for an accurate prediction of reflection generated from a linear slope. It was determined the MSE becomes significantly inaccurate for gradients in depth larger than 1:3. The MSE was compared against a three-dimensional finite element model (FEM) solution for multiple slopes as shown in Figure 2.8.

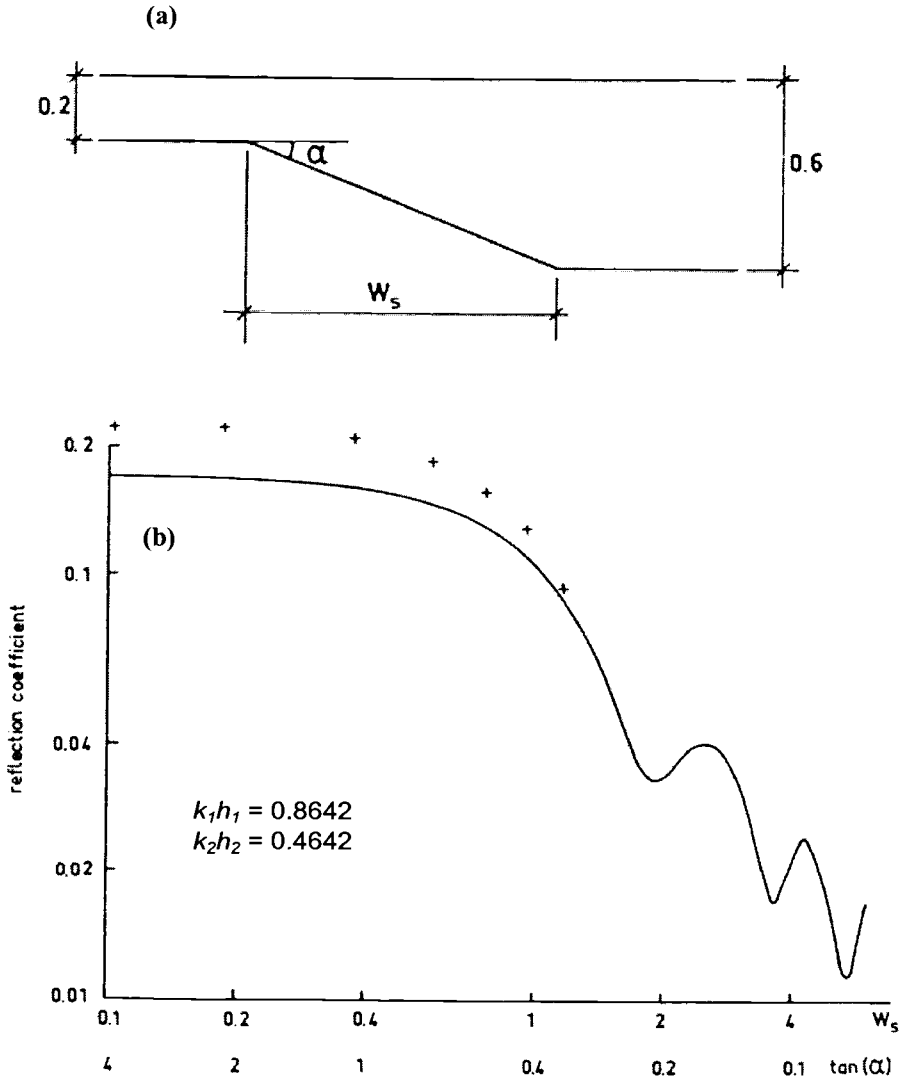

Figure 2.8: Inaccuracies in predicting wave reflection; **(a)** planar slope **(b)** reflection coefficient __ = MSE, + = 3D finite element model (modified from Booij 1983)

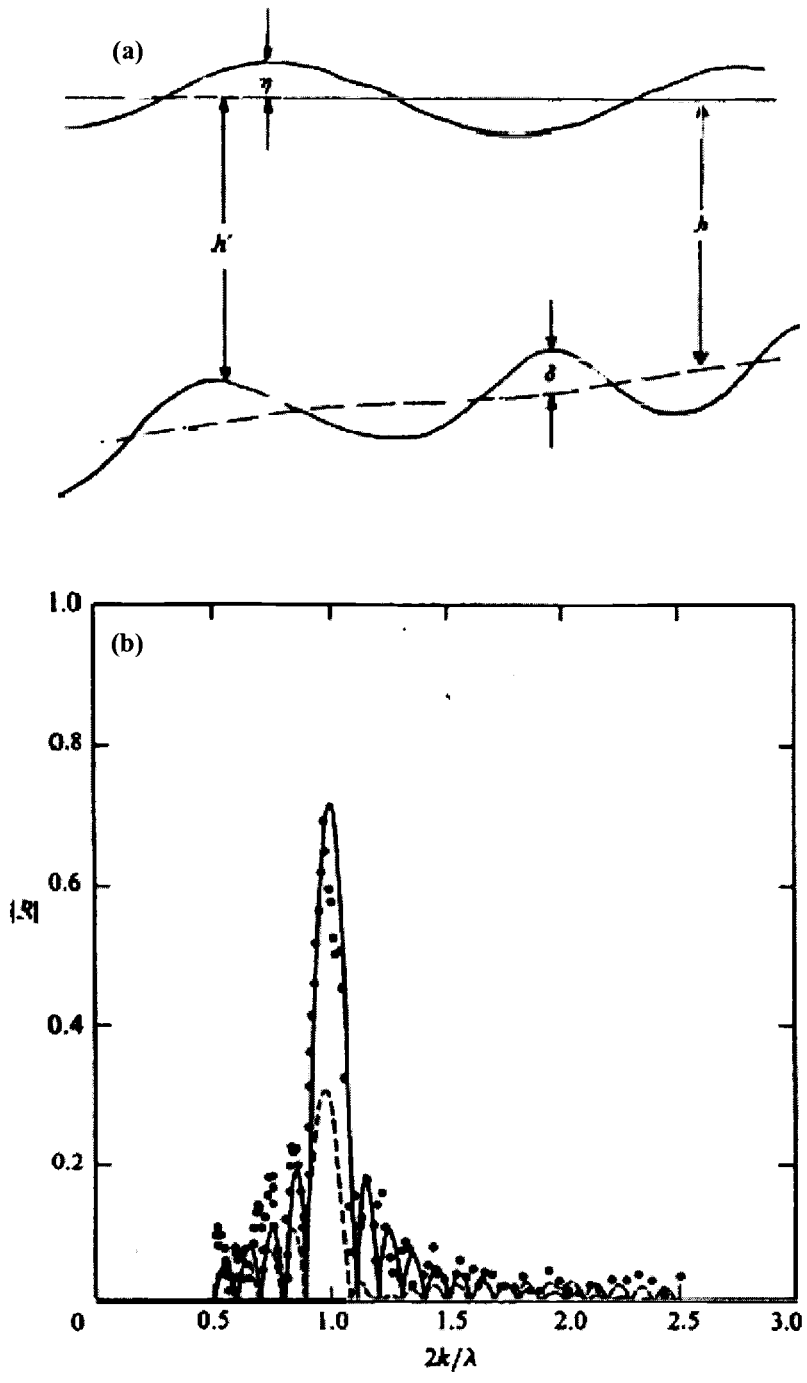

Figure 2.9: Inaccuracies in predicting wave reflection from a rapidly varying ripple bed; **(a)** definition sketch of ripple bed **(b)** reflection coefficient. --- = MSE, __ = EMSE, • = experimental data (modified from Kirby 1986)

Kirby (1986) went further to retain one of the higher order terms proportional to the bottom curvature $\nabla^2 h$ while investigating the wave propagation over rapidly varying small amplitude ripple beds. The original MSE was unable to accurately

predict the reflection coefficient for the phenomenon known as Class I Bragg resonance as illustrated in Figure 2.9. However, the inclusion of the curvature term was shown to correct for the MSE shortcomings. The new formulation of Kirby (1986) is referred to as the extended mild-slope equation (EMSE).

Massel (1993) also notes the inaccuracy of Berkhoff's (1972) original formulation in situations where the bottom slope is steep. Using a Galerkin-Eigenfunction Method and retaining higher order terms proportional to the bottom curvature $\nabla^2 h$ and the bottom slope squared $(\nabla h)^2$ it was shown that the solution performed much better than the MSE. The results using this formulation were shown to match very well with Booij's (1983) three-dimensional FEM solution. The equation formulated by Massel (1993) is now commonly referred to as the modified mild-slope equation (MMSE). In the original form proposed by Massel (1993), the equation retained the evanescent (non-propagating) modes in the solution. However, the MMSE for plane-waves can be represented as

$$\nabla \cdot (CC_g \nabla \tilde{\phi}) + \omega^2 \left\{ \frac{C_g}{C} - R_1 (\nabla h)^2 - R_2 \nabla^2 h \right\} \tilde{\phi} = 0 \tag{2.5}$$

in which the only difference between Berkhoff's MSE are the two higher order terms proportional the bottom curvature and slope squared. This equation is equivalent to the modified mild-slope equation given by Chamberlain and Porter (1995). The evolution of these higher order terms R_1 and R_2 from shallow water to deep water is illustrated in Figure 2.10 in dimensionless form with

$$E_1 = -\frac{C}{C_g} R_1 \tag{2.6}$$

$$E_2 = -\frac{k_o C}{C_g} R_2 \tag{2.7}$$

From this figure it is seen that both E_1 and E_2 have little significance in deep water, however they play a significant role in the intermediate depth region ($\pi/10 < kh < \pi$). Additionally, in the shallow water regime, the slope squared term is at its largest in absolute magnitude. Therefore the differences between the MSE and the MMSE will be most pronounced in the nearshore region (i.e intermediate and shallow water regions) for features that break the mild-slope criterion.

In order to investigate the effects of random waves over ripple beds, Suh et al. (1997) derives two equivalent time-dependent forms of the MMSE excluding the evanescent modes using both a Green's formula method and a Lagrangian formulation. Through comparing the incident and transmitted spectra the amount of reflection associated with different frequency bands was quantified. The amount of reflection generated by the ripple patch for Class I Bragg resonance was shown to produce very similar results to that witnessed in the case of monochromatic waves.

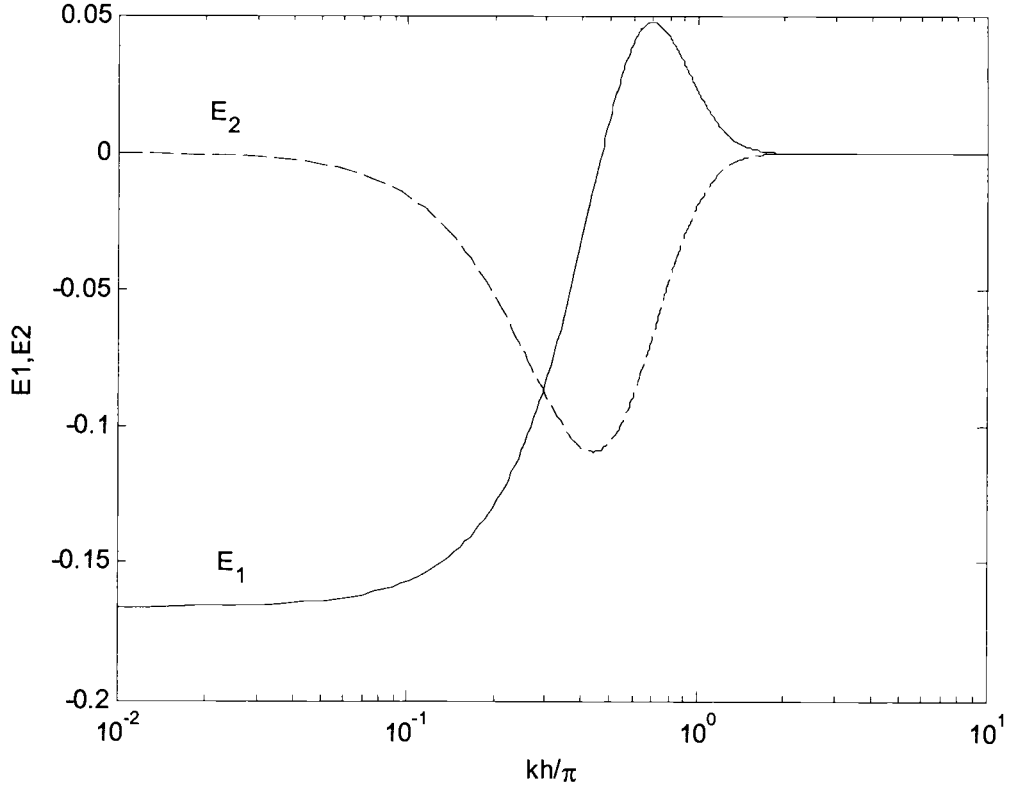

Figure 2.10: Evolution of higher order terms R_1 and R_2 (calculation following Lee et al. 1998)

2.2.1 Numerical model applications of the modified mild-slope equation

Arguments can be made that current generation Boussinesq models are more accurate than mild-slope equation based models in predicting wave propagation in the nearshore region. For example, these models incorporate the non-linear properties of waves as shoaling occurs. However, these models are computationally intensive and current generation formulations have been shown by Madsen et al. (2002) to have convergence problems due to the formulation of the kinematic bottom condition, which creates inaccuracies beyond certain wavenumbers k. The inaccuracy is shown in Figure 2.11 by comparing the results generated from a traditionally formulated Boussinesq model against the MMSE equation and the FEM solution given by Suh et al. (1997). The example shown in the figure is for the reflection generated by a single-slope originally investigated by Booij (1983). Therefore, in order to most accurately and efficiently model wave field modification around steep bathymetric features, the MMSE presently seems to hold the most potential for this application.

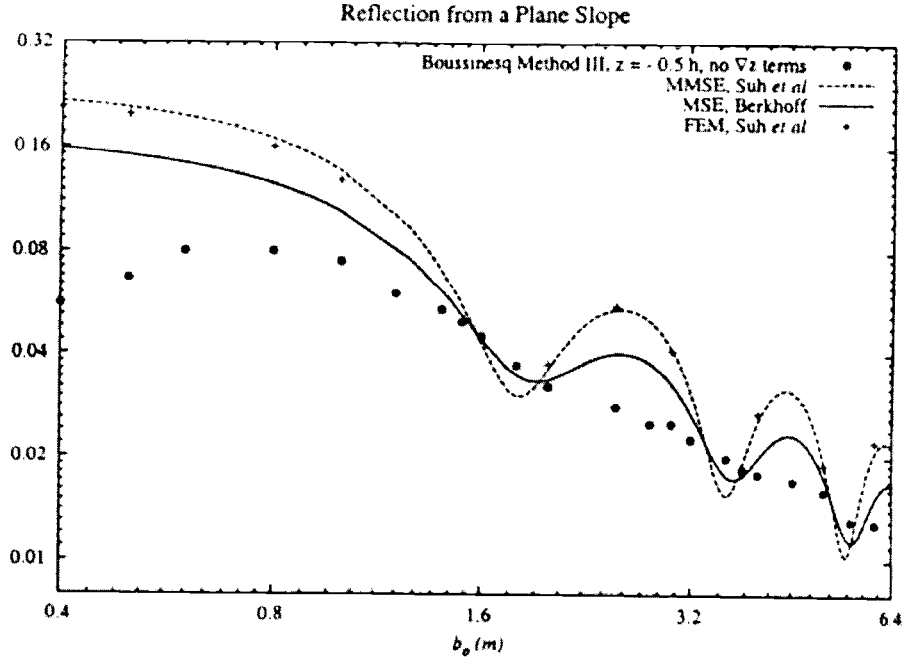

Figure 2.11: Current generation Boussinesq models inability to accurately predict reflection generated from the single slope case (from Madsen et al. 2002)

In order to solve the modified-mild slope equation for arbitrary bathymetry Lee et al. (1998) and Suh et al. (2001) extend Copeland's (1985) hyperbolic solution to the MSE by retaining the higher order terms proportional to the bottom curvature and slope squared. The structure of the formulation follows a hyperbolic system of equations which relates the free-surface elevation with the depth-integrated volume flux as a function of time; the model is run to steady-state to achieve the solution for the given domain.

Another numerical application of the MMSE is used in the RIDE wave model by Maa (2002) which solves equation (2.5) in its full elliptic form. The solution to the fully elliptical equation is computationally intensive. However, the author has optimized the model using a Gaussian Elimination technique. The use of this model may not be practical for cases other than harbors. Here the effects of resonance are very complicated and the full elliptical equation does best at representing the problem.

3.0 One-dimensional analysis

Although the accuracy of the modified mild slope equation (MMSE) has been confirmed for the case of a single slope with a large gradient in depth, its accuracy for a trench has not been investigated. By successfully comparing the results against analytical solutions, justification for its extension to more generalized bathymetries can be made. Additionally, the ability to represent a surf zone by including the effects of wave shoaling and wave breaking give the model significant promise for future applications. The following sections step through the formulation and numerical implementation of the MMSE in one horizontal dimension.

3.1 Implementation of modified mild-slope equation model

The MMSE given by Massel (1993) in its elliptic form, neglecting the evanescent modes is given in equation (2.5). The parameters representing the second order bottom effects are given by

$$R_1 = \frac{1}{\cosh^2 kh}(W_1 I_1 + W_2 I_2 + W_3 I_3 + W_4 I_4 + W_5 I_5 + W_6) \tag{3.1}$$

$$R_2 = \frac{1}{\cosh^2 kh}(U_1 I_1 + U_2 I_2 + U_3 I_3) \tag{3.2}$$

where W_i, U_i, and I_i can be found in Appendix A. W_i and U_i represent weighting functions which depend on k and h and I_i correspond to depth integrals of various hyperbolic functions. The MMSE was recast into a hyperbolic set of two first-order equations by Lee et al. (1998). The formulation for these set of equations follows Copeland (1985) but now retains the higher order terms that are associated with the MMSE formulation. The resulting set of equations are given by

$$\frac{\partial \eta}{\partial t} + \frac{1}{\frac{C_g}{C} - R_1(\nabla h)^2 - R_2 \nabla^2 h} \nabla \cdot \mathbf{Q} = 0 \tag{3.3}$$

$$\frac{\partial \mathbf{Q}}{\partial t} + CC_g \nabla \eta = 0 \tag{3.4}$$

The vertically integrated volume flux in the cross-shore direction $\boldsymbol{Q}$ is given by Copeland (1985) as

$$\mathbf{Q} = \frac{CC_g}{g} \nabla \tilde{\phi} \tag{3.5}$$

For one horizontal dimension, the cross-shore component of the vertically integrated volume flux is referenced to as $Q = \{\mathrm{P}\}$

3.1.1 Finite difference method implementation

Equations (3.3) and (3.4) are discretized using a leap-frog method staggered in both time and space. The equations in the numerical model follow as

$$\frac{\eta_i^{n+1/2} - \eta_i^{n-1/2}}{\Delta t} + \frac{\frac{P_{i+1}^n - P_i^n}{\Delta x}}{\left[\frac{C_g}{C} - R_1\left(\frac{dh}{dx}\right)^2 - R_2 \frac{d^2 h}{dx^2}\right]_i} = 0 \tag{3.6}$$

$$\frac{P_{i-1/2}^{n+1} - P_{i-1/2}^n}{\Delta t} + \left[CC_g\right]_{i-1/2} \frac{\eta_i^{n+1/2} - \eta_{i-1}^{n+1/2}}{\Delta x} + \omega \left[D_s\right]_{i-1/2} P_{i-1/2}^n = 0 \tag{3.7}$$

where the superscript n defines the time step and subscript i defines the spatial step in the cross-shore direction.

The bottom slope squared and bottom curvature terms are represented using standard central differencing procedures. The relations for each respectively with j = 1 are

$$\left[\left(\frac{dh}{dx}\right)^2\right]_i = \left(\frac{h_{i+j} - h_{i-j}}{2j \cdot \Delta x}\right)^2 \tag{3.8}$$

$$\left[\frac{d^2h}{dx^2}\right]_i = \frac{h_{i+j} - 2h_i + h_{i-j}}{(j \cdot \Delta x)^2} \tag{3.9}$$

However, a problem that arises with these relations when the denominator of equation (3.3) becomes negative (i.e. $\{C_g/C - R_1(\nabla h)^2 - R_2\nabla^2 h\} \leq 0$), which occurs when sharp transitions in depth, notably corner points (or where the curvature approaches infinity). As an empirical fix, Lee et al. (1998) recommends the use of the smallest possible integer j in equations (3.8) and (3.9) that avoids this problem. This reduces the magnitude of curvature term enough to achieve a positive denominator in equation (3.3). The minimum j value is proportional to the number of points discretizing the slope N as well as inversely proportionate to the specified grid size Δx. This is because the maximum curvature approaches its infinite value as the grid size becomes small. Therefore, the controlling factor for a positive denominator in equation (3.3) is dominated by the product of $j\Delta x$. Lee et al. (1998) does not give further guidance on how the approximation of the curvature and slope squared terms affect the solution, therefore this will be one of the preliminary tests in the current study.

There have been multiple techniques for the internal generation of waves numerically. Examples include, the technique following Larsen and Dancy (1983) for Boussinesq equations. Also, the techniques by Madsen and Larsen (1987) and Lee and Suh (1998) have been tailored for Copeland's (1985) hyperbolic solution to the MSE. The technique described by Madsen and Larsen (1987) is employed in the present model. For one horizontal coordinate (i.e. cross-shore), waves are generated within the model boundaries at a single point. In addition, backscattered waves are allowed to pass freely through the source without re-reflecting. At the generation

point a specified amount of water is added at each time step. Here, a free surface elevation η^* is added to the free surface elevation of the incident wave η^I for each time step Δt following the relation

$$\eta^* = 2\eta^I \frac{C\Delta t}{\Delta x} \tag{3.10}$$

where Δx is the spatial grid size. For a gradual start of wave generation, the left hand side of equation (3.10) is multiplied by $\tanh(0.5t/T)$, where T is the wave period. Additionally, for numerical stability the time step is chosen according to the Courant number $C_r = C\Delta t/\Delta x = 0.2$. For an in-depth study of the internal generation of waves in various time-dependent models, the reader is referred to Lee and Suh (1998). For steady-state conditions to be achieved, it is necessary to damp the wave energy before reaching the lateral boundaries in the model. Therefore two sponge layers are placed at both cross-shore boundaries. This prevents inaccuracies resulting from numerical reflection occurring at the model boundaries. The inclusion of the sponge layer modifies equation (3.4) to the following

$$\frac{\partial \mathbf{Q}}{\partial t} + CC_g \nabla \eta + \omega D_s \mathbf{Q} = 0 \tag{3.11}$$

where the damping coefficient is defined as

$$D_S = \begin{cases} 0, & \textit{outside sponge layer} \\ \dfrac{e^{d/S} - 1}{e - 1}, & \textit{inside sponge layer} \end{cases} \tag{3.12}$$

where d is the distance away from the initiation of the sponge layer; and S is the thickness of the sponge layer. Suh et al. (2001) advises for the thickness to be 2.5 times the local wavelength. This has been shown to be adequate in damping the wave amplitude to a negligible magnitude by the time the wave reaches the lateral boundary.

3.2 Comparison to Booij (1983)

The reflection from a single slope with constant depth on either side is found using both the MSE and the MMSE form of the model. Copeland's (1985) original MSE solution may be obtained by setting the parameters R_1 and R_2 in equation (3.3) to zero. The results of each model are compared with the FEM solution used by Suh et al. (1997). Booij (1983) illustrates the inaccuracy of the MSE at large gradients in depth by quantifying the amount of reflection received from a single slope of variable width W. Lee et al. (1998) repeats the problem comparing Copeland's (1985) hyperbolic MSE to the MMSE counterpart. The present study uses an identical model formulation; therefore, a confirmation of the numerical implementation is preformed.

An incident wave with a period of $T = 2$ sec is generated from the cross-shore location $x = 0$. The water depth in the region upwave of the slope is $h_1 = 0.6$m ($k_1h_1 = 0.8642$), while the water depth downwave of the slope is $h_2 = 0.2$m ($k_2h_2 = 0.4642$). The definition sketch is identical with that of Figure 2.8 (a), other than the inclusion of the two sponge layers at each boundary. The model is considered to have achieved steady-state after a time of $t = 30T$. After these conditions are reached, the reflection coefficient K_r is calculated in a cross-shore region from $x = \lambda_1$ to $x = 2\lambda_1$ (or one wave-length behind the up-wave slope corner). In order to separate the incident and reflected waves, wave envelope theory is followed. Calculating the maximum and minimum free surface elevation $(\eta_i)_{max}$ and $(\eta_i)_{min}$ at each grid point in time allows the upper and lower envelope to be found. The envelope is represented by the dark line encasing multiple snapshots of η_t in time in Figure 3.1. Subsequently, the maximum $(\eta_t)_{max}$ and minimum $(\eta_t)_{min}$ of the envelope over the entire region is found and the incident H_i and reflected H_r wave heights are found through the following relations

$$H_i = (\eta_t)_{max} + (\eta_t)_{min} \tag{3.13}$$

$$H_r = (\eta_t)_{max} - (\eta_t)_{min} \tag{3.14}$$

Additionally, the reflection coefficient may then be obtained by

$$K_r = \frac{H_r}{H_i} \tag{3.15}$$

The wave envelope corresponding to a slope width of W = 0.1 m (or 4:1 slope) is shown in Figure 3.1. Following Lee et al. (1998), the discretization for adequate spatial resolution corresponds to a ratio of local wavelength to grid size of $(\lambda_l/\Delta x)_{min}$ = 60. For this problem, this is equivalent to a grid size Δx = 0.0727 m. The reflection coefficient is plotted versus the cross-shore slope width W in Figure 3.2. The results are identical with those generated by Lee et al. (1998) giving confidence that the present implementation of the numerical model is correct. The results also illustrate the inaccuracy of the MSE model as first pointed out by Booij (1983). It is seen that the MSE significantly underpredicts the magnitude of K_r for steep slopes (or small W). Lee et al. (1998) points out the statement by Booij (1983) that the MSE remains accurate until slopes of 1:3 is somewhat unconvincing since his FEM solution did not predict reflection coefficients for slopes milder than 1:3. Comparing the FEM solution of Suh et al. (1997) to the two numerical models at milder slopes (or large W) shows that the MSE still remains inaccurate in predicting K_r. However, the error here is minimal since the reflection coefficient is only 2-3% in absolute magnitude. This may be the reason for the limit of 1:3 by Booij (1983). It should be noted that this test is only performed for one wave period. Thus only one wave condition corresponding to k_1h_1 = 0.8642 is studied. In addition to the slope of the transition, wave frequency (or correspondingly k_1h_1) will influence the reflection coefficient. However, the present study is more interested in the reflection generated by a trench or pit so no further tests were investigated.

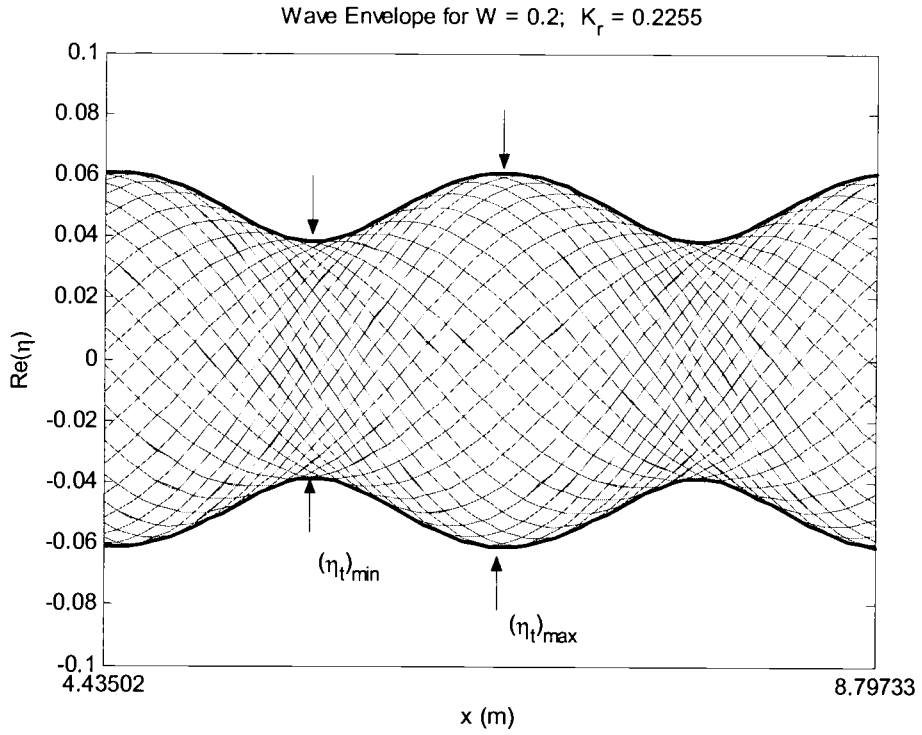

Figure 3.1: Wave envelope over $x = \lambda_l$ to $x = 2\lambda_l$ for $W = 0.2$m

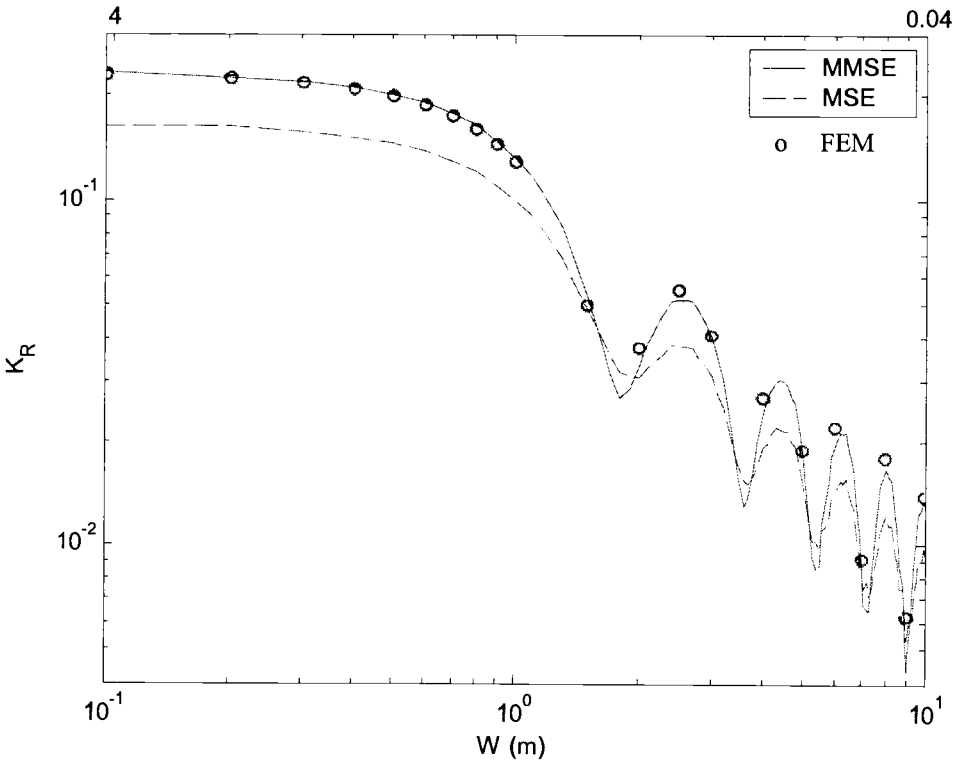

Figure 3.2: Reflection coefficient K_r versus cross-shore slope width W.
--- = MSE; ___ = MMSE; o = FEM solution of Suh et al. (1997)

3.2.1 Sensitivity test on bottom curvature and sloped squared terms

As the desired slope to be modeled is increased, the curvature term also increases. As pointed out previously, problems arise in the model formulation if this term becomes too large. Therefore, it is of interest to determine whether the empirical fix by Lee et al. (1998) (i.e. increasing j in equations 3.8 and 3.9) will significantly affect the magnitude of K_r. If this proves to alter the results considerably, than a limitation on the slope must be made. Table 3.1 demonstrates the impact of increasing the integer j on the reflection coefficient K_r for a 2:1 slope (or W = 0.2m) in the previous problem. This is the steepest slope that could be modeled with j = 1. As shown in the table, the most significant jump in K_r occurs when j is increased from 1 to 2, also corresponding to the largest reduction in the maximum curvature and slope squared. Although j should never be defined larger than the minimum integer required for a positive denominator in equation (3.3), Table 3.1 illustrates that significant errors do not arise until j = 10. The maximum curvature occurs at the corners of the slope (in reality this is infinity for corner points), while the maximum slope occurs at the midpoint of the slope. The effect of increasing j is shown to dampen the magnitude of both terms, while spreading a value to cross-shore locations designated by the value of j as illustrated in Figure 3.3. This produces an artificial smoothing of the slope sidewalls, making the slopes influence on $\nabla^2 h$ and $(\nabla h)^2$ extend to a larger range of cross-shore points than is strictly valid for this idealized bathymetry. It should be noted that the smoothing is only for these two terms and the actual bathymetry used in the model remains unchanged from the original input. The number of grid points defining the slope for this case is N = 2. Since Δx is not a multiple of W (when based on the criterion $\lambda_l/\Delta x$ = 60), the corner points are not exactly represented. As the width of the slope W becomes narrower, the corners are discretized more roughly. A preliminary test showed this to have negligible effects on the magnitude of K_r. Therefore, the criterion imposed by Lee et al. (1998) on $\lambda_l/\Delta x$ is kept the same for this test. However, this creates the asymmetry witnessed in the curvature and slope squared in Figure 3.3.

Finally, as an exercise, it is demonstrated that if j is increased to a large enough value ($j > 40$ for this case) both the curvature and slope squared terms approach zero and K_r approaches value calculated using the MSE solution. Another point to be made is that there is a limit on the maximum curvature that is allowed by the model. This is controlled by the value of j_{min} which is proportional to the slope (i.e. j_{min} is larger for steeper slopes). Thus, the bottom curvature used by the model will actually have a similar magnitude to that of a milder slope in order to keep a positive denominator in equation (3.3). Therefore, as slope is increased, the model can become inaccurate after a certain gradient in depth is exceeded. Although in this example, 2:1 is the steepest slope that can be modeled without increasing j > 1, the prediction in K_r is shown in Figure 3.2 to remain adequate for slopes as steep as 4:1 ($W = 0.1$ m). The problem with accurately representing the curvature is strictly a result in attempting to match analytical solutions which often solve bathymetries having sharp corner points. In reality, these transitions are much smoother and these problems are unlikely to develop.

Table 3.1: Impact of j on K_r for a trench with sidewall slope = 2:1, $\lambda_f/dx = 60$

	$j\Delta x$	$(\nabla h)^2_{max}$	$(\nabla^2 h)_{max}$	K_r (MMSE)†	K_r (MSE)†
$j = 1$	0.0727	4.00	20.65	0.2255	0.1622
$j = 2$	0.1454	1.89	12.04	0.2302	--
$j = 3$	0.2181	0.84	8.41	0.2306	--
$j = 4$	0.2908	0.47	4.73	0.2289	--
:	:	:	:	:	--
$j = 10$	0.727	7.57×10^{-2}	7.57×10^{-1}	0.1989	--
$j = 40$	2.908	4.73×10^{-3}	4.73×10^{-2}	0.1637	--
$j = 80$	5.816	1.18×10^{-3}	1.18×10^{-2}	0.1627	--

† $K_r = 0.228$ in FEM solution for limiting case; $W = 0$ (from Suh et al. 1997)

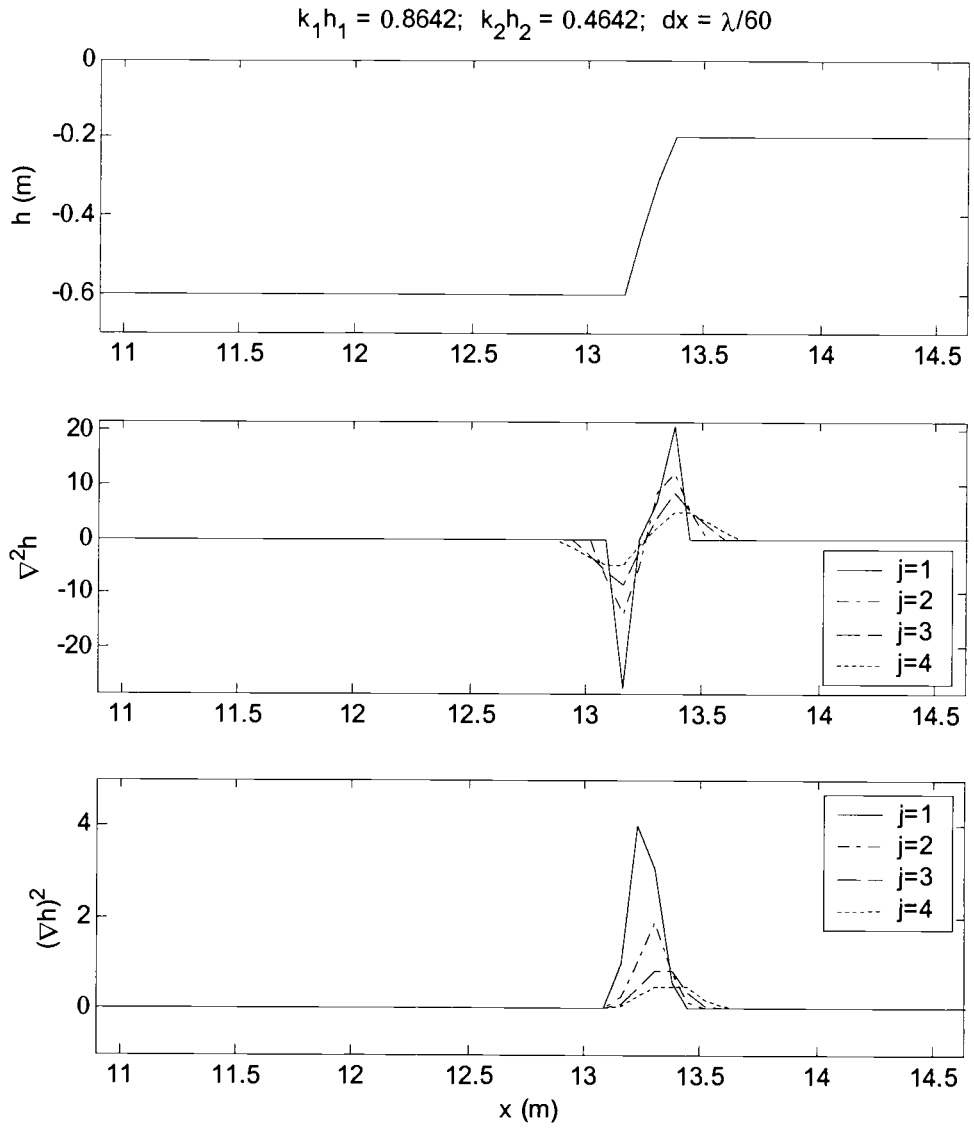

Figure 3.3: Water depth, curvature, and slope squared for different *j* values; Domain shows $0.5L_1$ upwave and $0.5L_2$ down wave of slope; slope = 2:1

3.3 Comparison to analytical solutions for a vertical trench

As previously stated the simplest form of a bathymetric anomaly solved analytically has been an infinitely long vertical trench with cross-shore width a (e.g. Lee and Ayer 1981, Kirby and Dalrymple 1983). However, representing a true rectangular trench in a numerical model is impossible using a standard finite difference scheme no matter how fine the discretization. In a finite difference grid the trench will actually have two cross-shore widths a_1 and a_2 as illustrated by Figure 3.4. Yet as cell discretization becomes finer (i.e. $a_1 \approx a_2$) the solution may converge toward the vertical trench solution; this is the first hypothesis tested. However, the model can be more appropriately compared to the recent work of Bender (2003) who solves for a trench with linearly sloping sidewalls. This allows for a direct comparison of the model with an analytical solution.

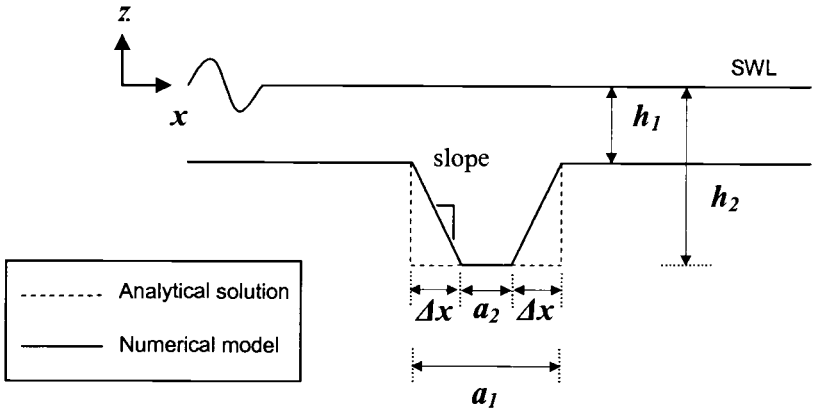

Figure 3.4: Definition sketch of demonstrating the difference between an analytical solution and a numerical models representation of a trench

3.3.1 Convergence test on vertical trench approximation

Naturally it may be expected that as the number of cells discretizing the trenches sidewall slope N increases the trend in the solution will converge with minimal variability in K_r. Although this occurs in the present model, the end result is somewhat misleading. This is because problems occur in representing the curvature term $(\nabla h)^2$ as N increases. As shown in the previous section, the product $j\Delta x$ is the

controlling factor for maintaining a positive denominator in equation (3.3). For instance, as N increases (or Δx decreases) j is required to increase. This in turn modifies the magnitudes of $(\nabla h)^2$ and $\nabla^2 h$ in equations (3.8) and (3.9) creating values which actually correspond to those of more gradually sloping trenches. In effect there is a limit on the maximum $(\nabla h)^2$ and $\nabla^2 h$ that can be calculated for a fixed grid size Δx. As a result, the converged solution is somewhat different than if the true curvature and slope terms (j =1) were able to be used. This leaves two options as viable paths for future analysis. Either require $j = 1$ and sacrifice the requirement of $\lambda/\Delta x \geq 60$ or keep the restriction on grid size and allow $j > 1$. Both methods were tested and the latter proved most comparable to the analytical work performed by Bender (2003).

The exclusion of the non-propagating (or evanescent) modes in equation (2.5) additionally plays a role in the accuracy of the solution. The impact has been shown by Kirby and Dalrymple (1983) to be most apparent when h_2/h_1 is large. The result is apparent in the reflection coefficient K_r which shifts to smaller k_1h_1 values as h_2/h_1 becomes large. Dingemans (1997, § 2.6) goes further by setting a quantitative limit for when the inclusion of the evanescent modes is important. It is stated that when the length/height ratio of the transition in depth is smaller than 2 their effects will alter the prediction in the reflection coefficient. This effect can be demonstrated through the use of the plane-wave solution in the long wave limit given by Kirby and Dalrymple (1983). This solution was originally formulated for a step by Lamb (1932) and was later proven by Miles (1967) to be equivalent to neglecting the evanescent modes at $k_2h_2 \leq \pi/10$. Figures 3.5 and 3.6 illustrate the deficiency of the plane wave solution for relative depths $k_2h_2 \geq \pi/10$ as well as when h_2/h_1 becomes large. The long wave limit in each of the figures is specified by the dashed line. Although the magnitude of the first peak in K_r is fairly accurate, the location in kh becomes significantly displaced. For the case of $h_2/h_1 = 7.625$ the shift in kh is significantly larger than in the case when $h_2/h_1 = 3.0$. This demonstrates the importance of the evanescent mode effect on the solution as the relative trench depth increases. However as a practical limit for applications, h_2/h_1 will rarely exceed 3. Evidently, this effect is important to recognize when comparing the numerical model to previous analytical solutions which include non-propagating modes in the formulation. As a general rule, there will

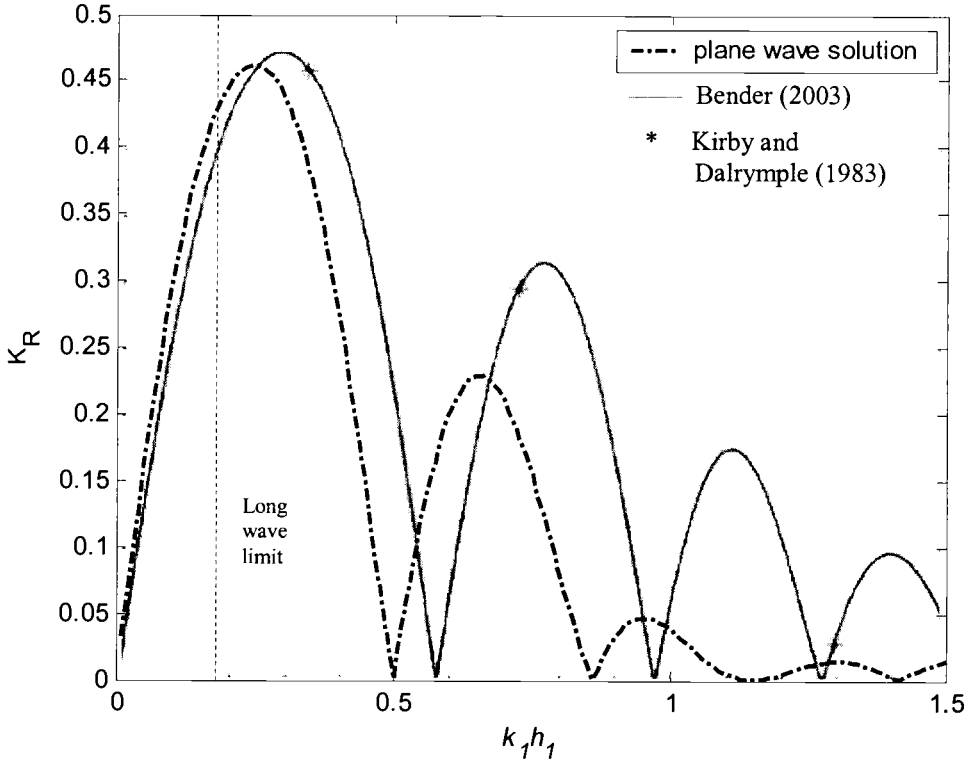

Figure 3.5: Reflection coefficient for $h_2/h_1 = 3$; $a/h_1 = 10$. __ = step method (from Bender 2003, Fig. 5-7), _._ = plane-wave approximation.

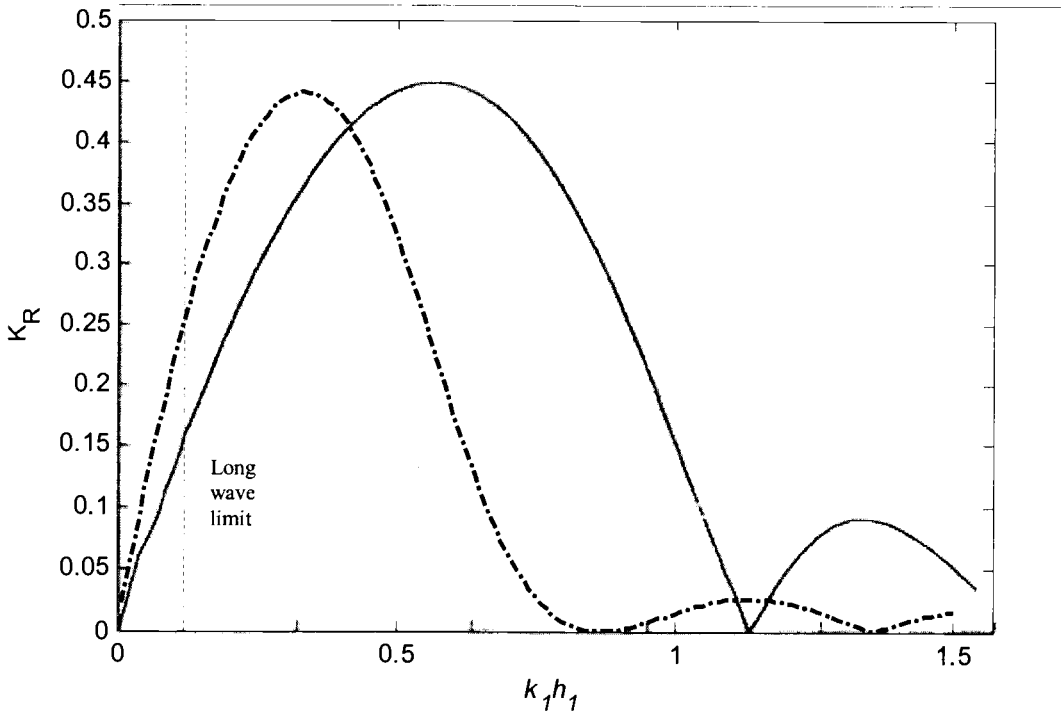

Figure 3.6: Reflection coefficient for $h_2/h_1 = 7.625$; $a/h_1 = 5.28$ (modified from Lee and Ayer, 1981)

always be some degree of shift in kh as a result of neglecting the non-propagating modes; and the severity of the shift will depend on the sidewall slopes of the trench and the relative depth h_2/h_1.

The analytical solution provided for a rectangular trench with dimensions $\bar{a} = a_1 = a_2$; $h_2/h_1 = 3$; $\bar{a}/h_1 = 10$ from Kirby and Dalrymple (1983) is used to compare four different trenches with varying sidewall slopes. Sidewall slopes of 1:1, 2:1, 4:1, and 8:1 with $h_1 = 1$ m are used by the numerical model as an approximation to the rectangular trench. Consequently as the sidewall slope gets milder, a_2 becomes much smaller. The definition sketch for the implementation into the numerical model is given in Figure 3.7. These slopes were determined to have the least variability in K_r for a similar grid size to wavelength requirement of $(\lambda/\Delta x)_{min} \geq 60$ imposed by Lee et al. (1998) for the single slope case. Figure 3.8 illustrates the stability of the solution for various values of $\lambda_1/\Delta x$ using four different sidewall slopes. The reflection coefficient is given for relative depths $k_1h_1 = 0.341$, 0.723, and 1.296 by (Kirby and Dalrymple 1983; Table 1) and again for a full range of k_1h_1 values in Bender (2003, Fig. 5-7). Based on the trend in K_r, the solution tends to hold stable for $\lambda/\Delta x \geq 60$ and for sidewall slopes $\leq$ 4:1. The standard deviation in K_r for all slopes $\leq$ 4:1 is less than 1% for grid sizes $\lambda/\Delta x \geq 40$. Note that the solution for trench sidewall slopes of 8:1 has a high variability (standard dev. > 2%) for the case of $k_1h_1 = 1.296$.

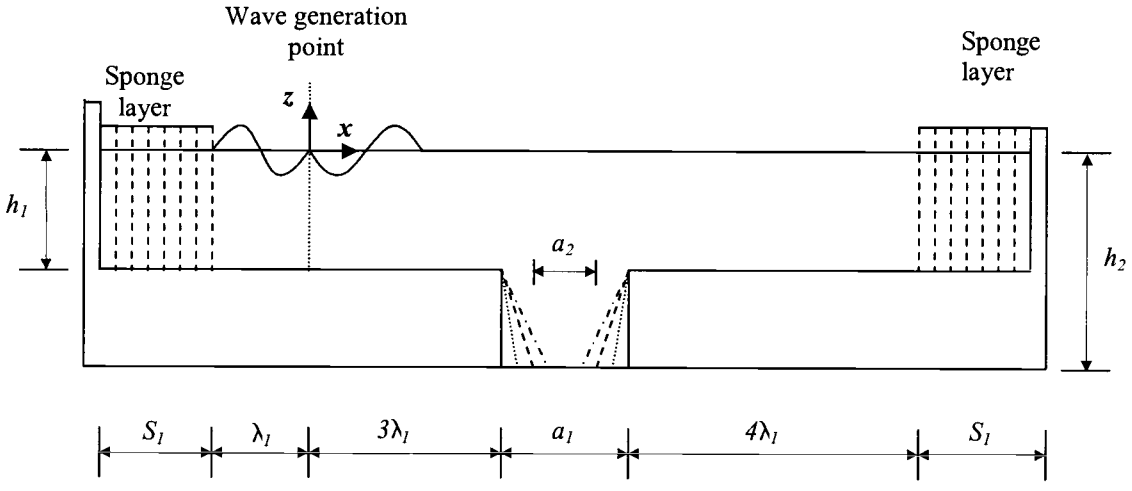

Figure 3.7: Domain considered in numerical model for rectangular trench approximation; __ slope = 8:1, slope = 4:1, --- slope = 2:1, _._ slope = 1:1 (rise:run)

This test considers only three values of k_1h_1 and does not give a very good illustration of how accurate the model predicts the maxima and minima of K_r, thus the model is run for multiple conditions. In this study, calculations of $k_1h_1 = 0$ to 1.5 with a step size of 0.02 are found. For the case when $k_1h_1 < 0.14$ a grid size of $\Delta x = \lambda_1/60$ is not sufficient in discretizing the trench sidewalls with sidewall slopes of 4:1. Using this criterion without making the width of the trench a a multiple of Δx also inhibits the grid from fully defining the trench corners. To fix both issues the smallest common multiple of the trench length that satisfies $\Delta x \geq \lambda_1/60$ at $kh = 1.5$ is used to determine the grid spacing for all kh values. This ensures that the trench is fully represented in the grid, as well as satisfying the wavelength to grid size requirement imposed in the convergence test. Figure 3.9 shows K_r as a function of relative water depth outside the trench k_1h_1 for the sidewall slopes 1:1, 2:1, and 4:1 along with the analytical solution (e.g. Bender 2003, Fig. 5-7). K_r is calculated in the same manner as in the single slope case; by defining the maximum and minimum of the wave profile upwave of the first trench corner in the cross-shore region from $x = \lambda_1$ to $x = 2\lambda_1$.

From the figure it is apparent that the prediction of K_r for a sidewall slope of 1:1 is closest to approximating the analytical solution for a rectangular trench (e.g. Kirby and Dalrymple 1983; Table 1). As the model attempts slopes larger than this, the prediction of K_r is seen to shift leftward in k_1h_1. This is somewhat expected since the non-propagating modes play a more important role in the solution as the sidewall slopes are increased. In addition the integer used for representing the curvature and slope squared terms needs to increase to $j > 1$ for stability. Therefore, the result is really a combination of both effects. For comparison purposes, the plane-wave solution following Kirby and Dalrymple (1983) is plotted along with both the numerical model and analytical solution results. One interesting comparison is that for the first peak in K_r, the shift in kh for a trench with a sidewall slope of 4:1 is nearly identical to that predicted using the plane wave solution. This gives confidence that the shift is occurring in the MMSE model as a result of neglecting the evanescent modes in the governing equation. However, there also exist inaccuracies in the magnitude of K_r at higher frequencies, particularly for the case with a 4:1 slope. This most likely is related to the approximation of the curvature and bottom slope squared

terms. These terms become significantly altered for steep sidewall slopes. For instance, for the 4:1 sidewall slope the minimum value of j ranges from 7 to 15. The parameter j is not constant over all k_1h_1 because the terms in the denominator in equation (3.3) are dependent on kh in addition to $(\nabla h)^2$ and $\nabla^2 h$. For this reason as $kh \rightarrow 0$, a larger integer j is required to maintain a positive sum in the denominator. Thus the upper limit of the minimum j value is referred to as j_{max} while the lower limit is j_{min}. Due to both of these complications, the hypothesis that the model can accurately approximate the rectangular trench problem if the sidewall slope is steep enough is disproved. However, it should be taken into consideration that the likelihood of actual features having vertical sidewall slopes is minimal.

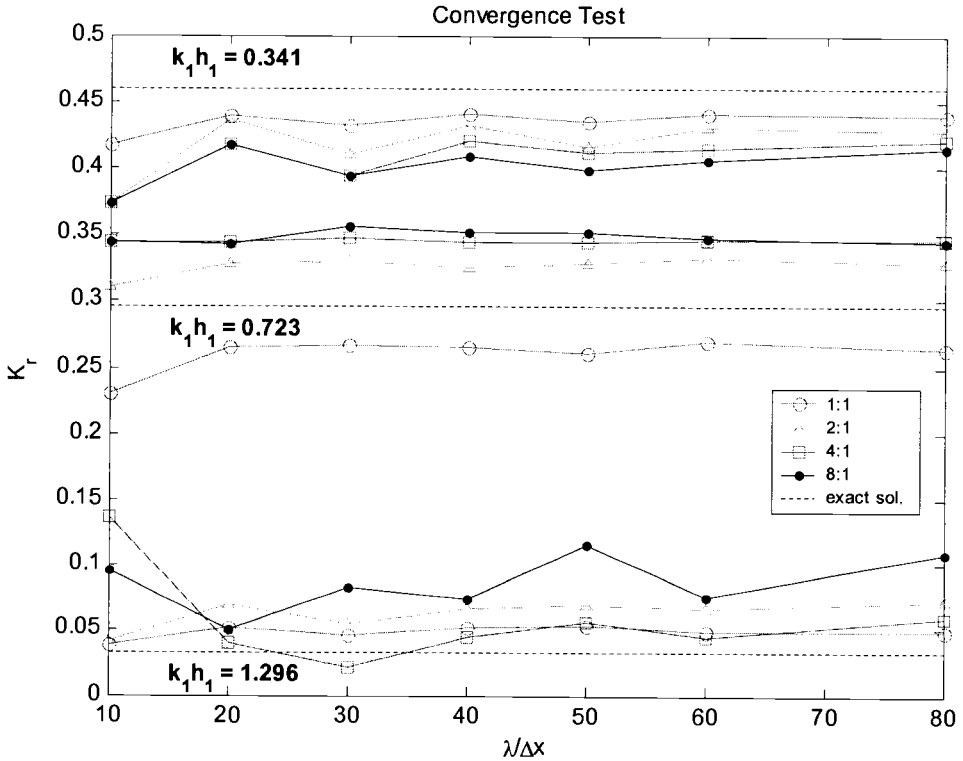

Figure 3.8: Convergence test for k_1h_1 = 0.341, 0.723, and 1.296 for various sidewall slopes; --- = Kirby and Dalrymple (1983) solution

Table 3.2: Vertical trench MMSE results, h_1 = 1m, h_2 = 3m, $\bar{a}$ =10m, Δx = 0.05m

Slope	a_1 (m)	a_2 (m)	N (# *pts.*)	$(K_r)_{max}$	$kh_{@\ max}$	j_{min}/j_{max}
1:1	10	8.0	41	0.4663	0.26	2/4
2:1	10	9.0	21	0.4818	0.24	4/9
4:1	10	9.5	11	0.4876	0.24	7/15

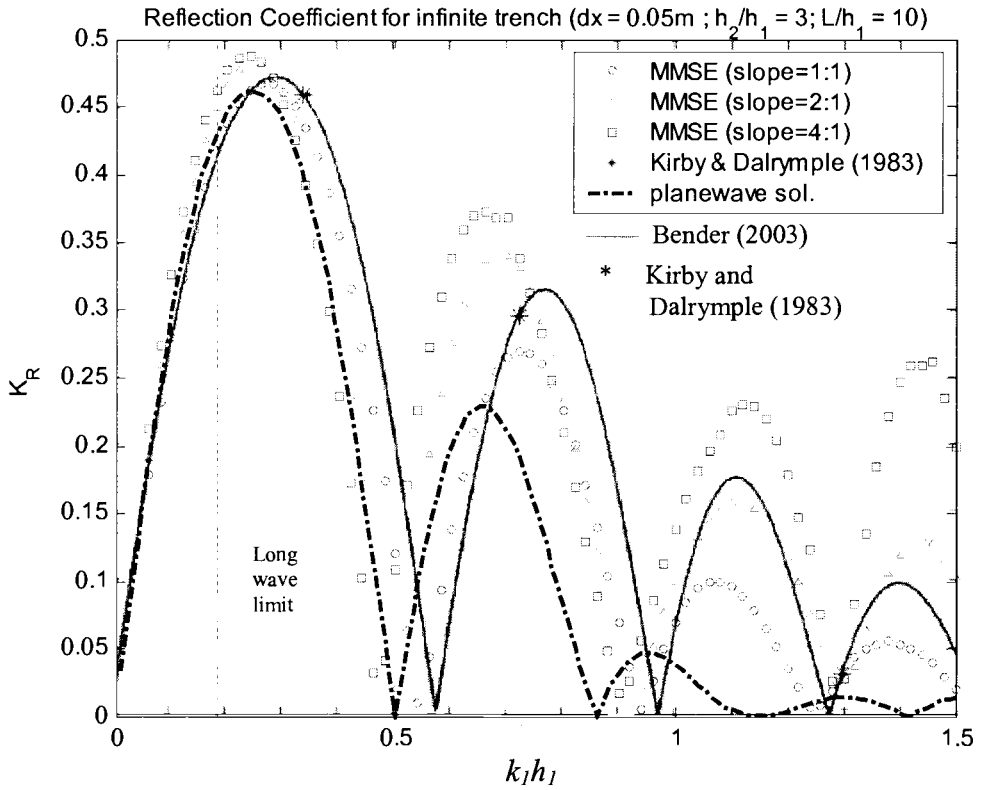

Figure 3.9: MMSE model results for slopes: o = 1:1, Δ = 2:1, and □ = 4:1; __ = Bender 2003 (step method); --- = plane wave solution

3.4 Comparison to trench with gradually sloping sidewalls

In order to test the models effectiveness more efficiently, the results are compared to the recent "step method" by Bender (2003). This solution is able to solve for sloping sidewalls, therefore a direct comparison between the numerical model and the analytical solution is made. Solutions are provided for sidewall slopes of 5000:1, 1:1, 0.2:1, and 0.1:1. The relative trench dimensions consist of the following: h_2/h_1 = 2, $\bar{a}/h_1$ = 15 (e.g. Bender 2003, Fig 5-7). A definition sketch for the numerical implementation is shown in Figure 3.10. The only change from the previous case is that a constant cross-sectional area is maintained inside the trench as the sidewall slope is changed. Thus the two trench widths a_1 (top) and a_2 (bottom) are the only dimensions which change. As a result the mean trench width $\bar{a}$ = ½ (a_1 + a_2) remains constant. The exact trench dimensions used in the numerical simulation are given in Table 3.3.

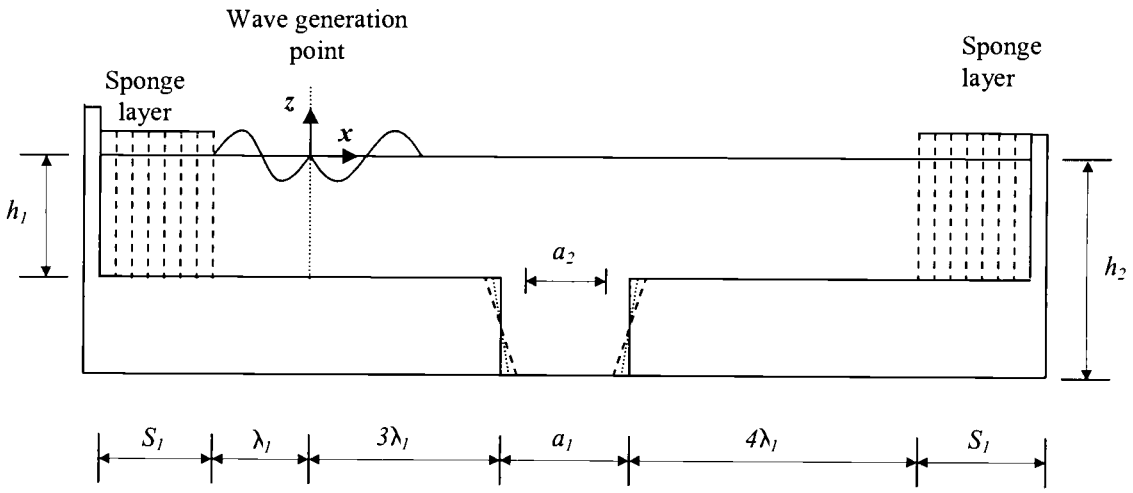

Figure 3.10: Domain considered in numerical model for Bender problem; ... slope = 1:1, --- slope = 0.2:1 (rise:run)

The first issue that needs to be addressed is the influence of approximating the curvature and bottom slope squared in the solution, in order to determine a limitation on the sidewall slope in the model. As in the previous case, it is found that discretizing the corners of the trench in addition to satisfying the grid size criterion $\Delta x \geq \lambda/60$ produces the most accurate solution. In order to satisfy both conditions in this example, a grid size of $\Delta x = 0.1$ m is employed. For the case of the trench with sidewall slopes of 1:1, the integer j required in equations (3.8) and (3.9) ranges from $j_{min} = 2$ to $j_{max} = 4$. Table 3.4 lists the dependency of j on the higher order bottom terms and reflection coefficient at a relative depth $k_1 h_1 = 1.5$. The change in the reflection coefficient with respect to the bottom slope and curvature terms is comparable to the single slope case. As in the single slope case, the change is not significant enough to question the accuracy of the solution. Additionally, Figure 3.11 illustrates the effect on the curvature and slope squared terms as j is increased from 1 to 4. The fact that all the trench corners are discretized properly results in the symmetry of the curvature and slope squared terms.

Table 3.3: Non-vertical trench MMSE results: h_1 = 2m, h_2 = 4m, $\bar{a}$ =30m, Δx = 0.1m

Slope	a_1 (m)	a_2 (m)	*N (# pts.)*	$(K_r)_{max}$	$kh_{@\ max}$	j_{min}/j_{max}
0.2:1	40.0	20.0	101	0.3100	0.12	1/1
1:1	32.0	28.0	21	0.3262	0.14	2/4

Table 3.4: Impact of increasing j for k_1h_1 = 1.5 (Δx = 0.1 m; slope =1:1)

	$j\Delta x$	$(\nabla h)^2_{max}$	$(\nabla^2 h)_{max}$	K_r
$j = 1$	0.1	1.000	10.0	--
$j = 2$	0.2	0.563	5.00	0.0598
$j = 3$	0.3	0.444	3.33	0.0586
$j = 4$	0.4	0.391	2.50	0.0569

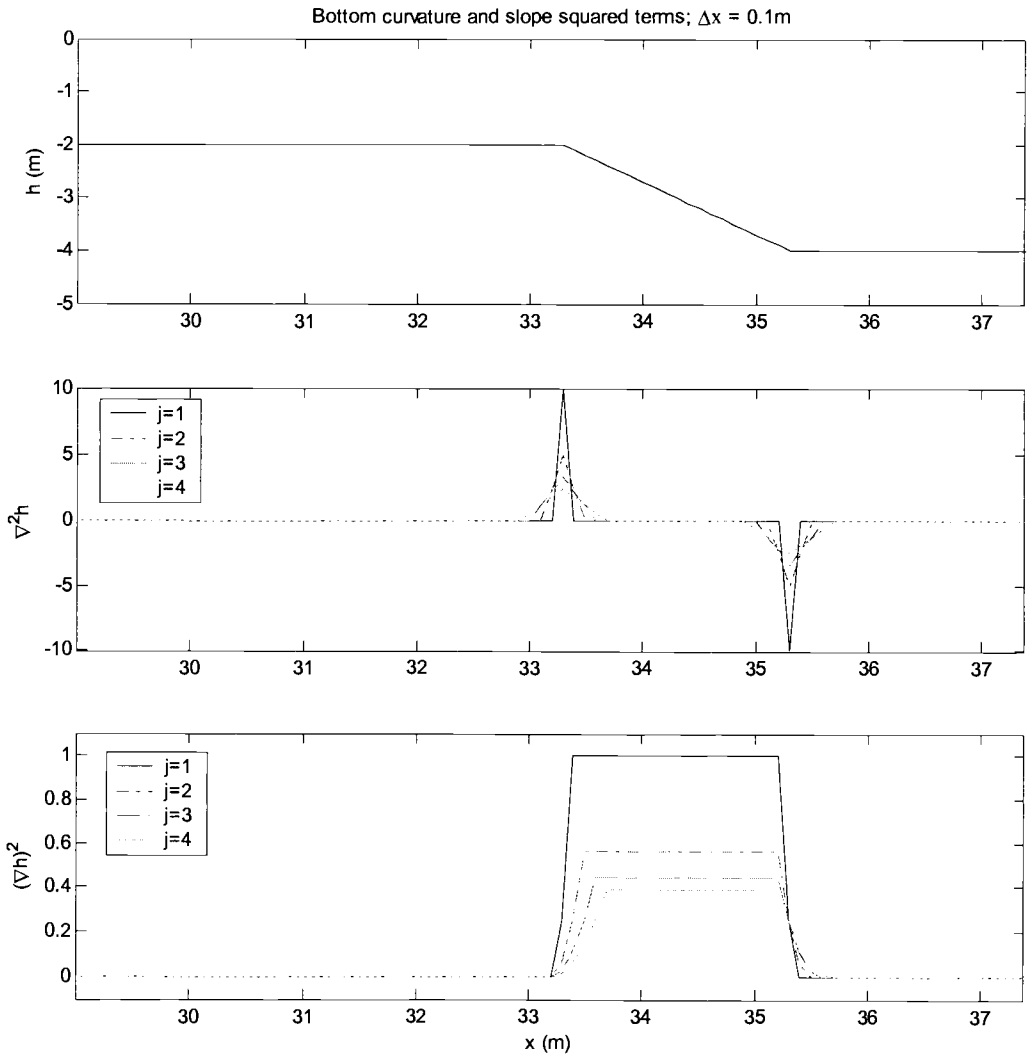

Figure 3.11: Water depth, curvature, and slope squared for different j values; Cross-shore domain: $0.5\lambda_1$ upwave and downwave of the upwave trench corner; slope = 1:1

Figures 3.12 and 3.13 compare the results predicted for a trench with 0.2:1 and 1:1 sidewall slopes using the MMSE model. The results are also plotted versus the data taken from figures in Bender (2003; Fig. 5-7). For the trench with mildly sloping sidewalls, the model produces very similar results. However, for the case of the 1:1 slope, there occurs a slight leftward shift in k_1h_1 in the predicted K_r. The magnitude of this shift seems to become larger in the high wave frequency region (i.e. large kh). This is most likely due for the same reasons found when trying to represent the rectangular trench with vertical sidewall slopes. Since the slope is fairly steep, the evanescent modes may start to contribute to the shift. Additionally, $j_{min} = 2$ is required, thereby creating an approximation in the terms $(\nabla h)^2$ and $\nabla^2 h$. Figures 3.14 and 3.15 display the MMSE models results along with Bender's (2003) long wave approximation (i.e. slope method) for a rectangular trench. Rather than comparing the numerical results to the plane-wave solution that is only capable of describing vertical sidewalls, this solution can accurately predict the reflection for linear sloping trench sidewalls within the range $k_2h_2 \leq \pi/10$. Additionally, since the approximation neglects the evanescent modes from the solution, the claim about its effect on the resultant shift in kh can be tested. In the long wave limit, the location and magnitude of K_r in the two solutions are nearly equal, even for the 1:1 sidewall sloped trench. This helps justify the claim that the absence of the evanescent modes in the solution contributes to the noticeable shift in kh, even for gradually sloping trench sidewalls. The results for the reflection coefficient calculated using the equivalent of Berkhoff's MSE can be obtained by setting the higher order terms in equation (3.3) to $R_1 = R_2 = 0$. The results using the MSE model are also included in Figures 3.14 and 3.15. According to Booij's statement, the MSE should predict an accurate solution for slopes milder than 0.33:1. From the results, it seems that the MSE does fairly well in representing the first peak in K_r for both cases. However, for the steeper trench of 1:1, the MSE model fails to accurately predict the magnitude and location of the subsequent peaks in K_r. For the third peak (i.e. $k_1h_1 = 0.88$) the MSE solution predicts $K_r = 0.0335$ versus the prediction by the MMSE of $K_r = 0.1860$. Figure 3.16 shows the cross-shore wave profile for the $k_1h_1 = 0.88$ using both the MSE

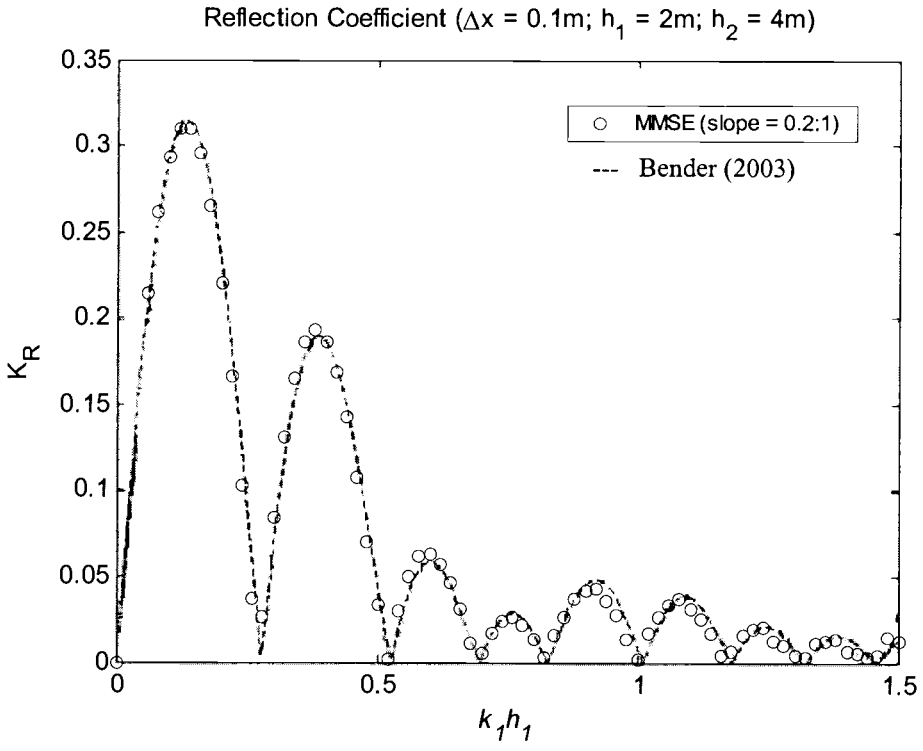

Figure 3.12: Reflection coefficient for trench with 0.2:1 sloped sidewalls; --- = Bender (2003); o = MMSE with $\Delta x = 0.1$m (Modified from Bender 2003)

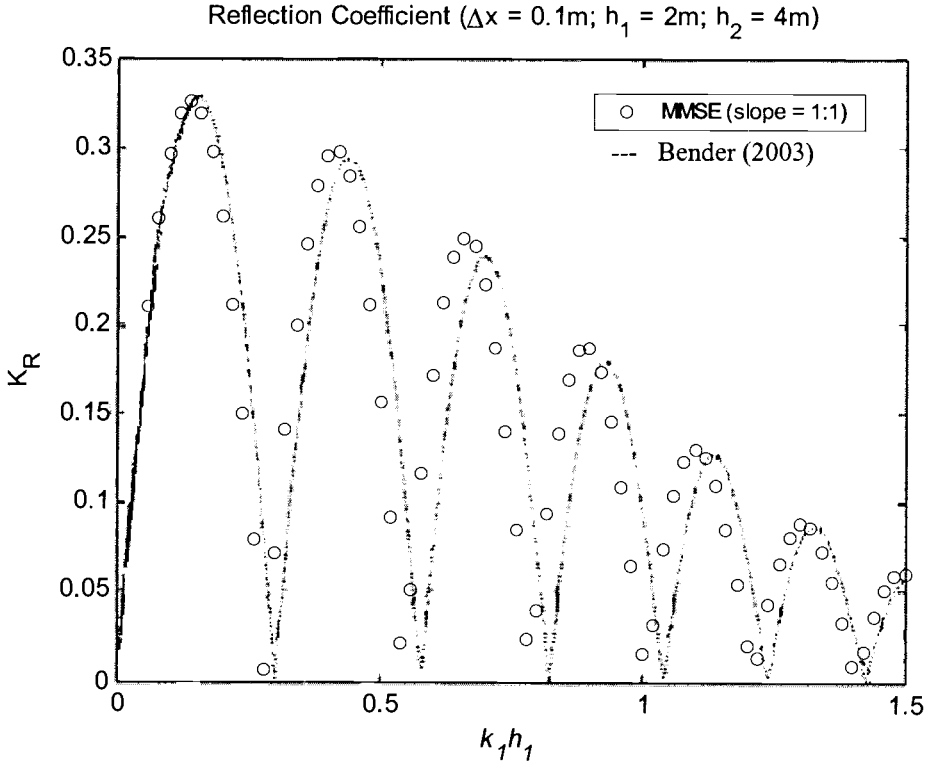

Figure 3.13: Reflection coefficient for trench with 1:1 sloped sidewalls; ... = Bender (2003); o = MMSE with $\Delta x = 0.1$m (Modified from Bender 2003)

and the MMSE models. This demonstrates how the MSE predicts larger transmitted wave heights leeward of the trench. When this difference is large, the result may influence the prediction of shoreline response. However, an infinitely long trench does not introduce the effects of diffraction or refraction created by longshore finiteness. The presence of diffraction may alter the magnitude of the transmitted wave in cases where a trench is finite in the longshore direction; the effects of this are considered in the following sections.

Another important concept to notice from the analysis is the dependency of the sidewall slope on K_r. The higher peaks of K_r still have a significant magnitude even in the intermediate depth range ($\pi/10 < k_1 h_1 < \pi$). Thus, the trenches influence on the wave field would persist over many different varieties of wave conditions. On the other hand as the slope of the trench sidewalls becomes more gradual such as for the 0.2:1 case, less than 5% reflection occurs for $k_1 h_1 > 0.5$. Therefore, by reducing the sidewall slopes of a borrow pit, only one or two possible wave conditions capable of producing significant reflection would exist.

The mean cross-shore width of the pit $\bar{a}$ is also demonstrated to control the number of maxima and minima in K_r, or the number of succeeding harmonics after the first peak. Qualitatively, this can be visualized by determining how many wavelengths will fit into the trench. As the width of the trench increases, the number of peaks in K_r will also increase. Using a normalized trench width $\bar{a}/h_1$ illustrates this effect. The trench in the case following Kirby and Dalrymple (1983, Table 1) is representative of a trench with $\bar{a}/h_1 = 10$ and exhibits 5 distinct peaks in K_r for $0 \leq k_1 h_1 \leq 1.5$; whereas the trench studied by Bender (2003, Fig. 5-7) with $\bar{a}/h_1 = 15$ has 6 peaks. Through the definition of $\bar{a}$, the selection of a_1 and a_2 allows for multiple sidewall slopes to be investigated. For example, using Bender's (2003) convention, the mean cross-shore width $\bar{a}$ occurs at the midpoint of the sidewall slope in depth. Thus, for gradually sloping sidewalls, the width at the top of the trench a_1 is larger than the top width for a steeper varying sidewall slope would be. This subsequently allows for a larger trench cross-sectional width with respect to the wavelength. This effect is illustrated by referring back to Figures 3.12 and 3.13 where the number of

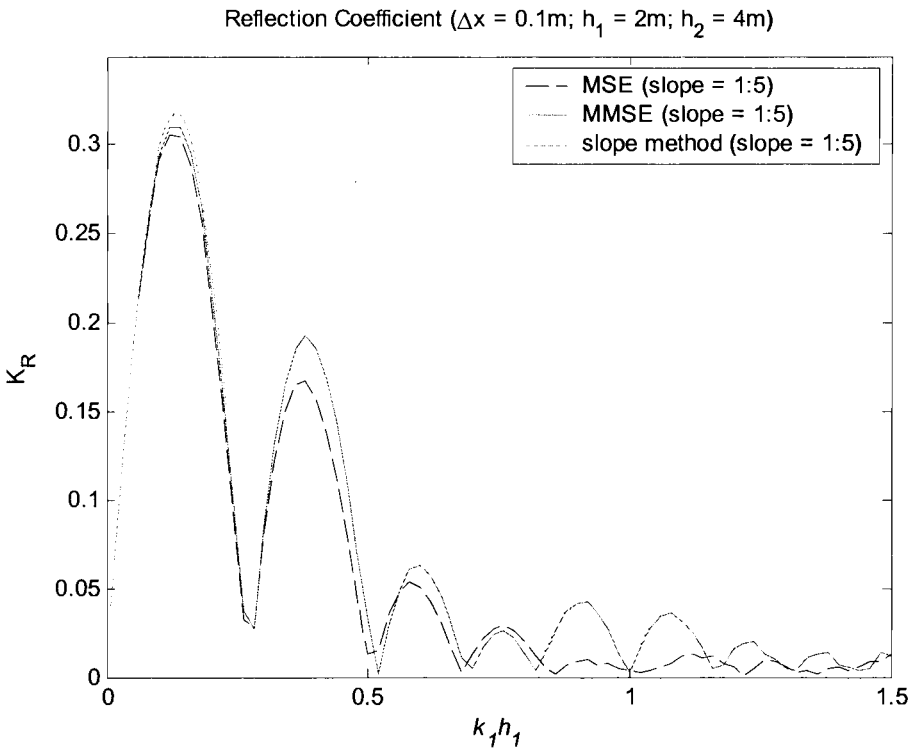

Figure 3.14: Comparison in reflection coefficient for a slope = 0.2:1; Δx = 0.1m
__ = MMSE model; --- = MSE; ... = Bender 2003 (slope method)

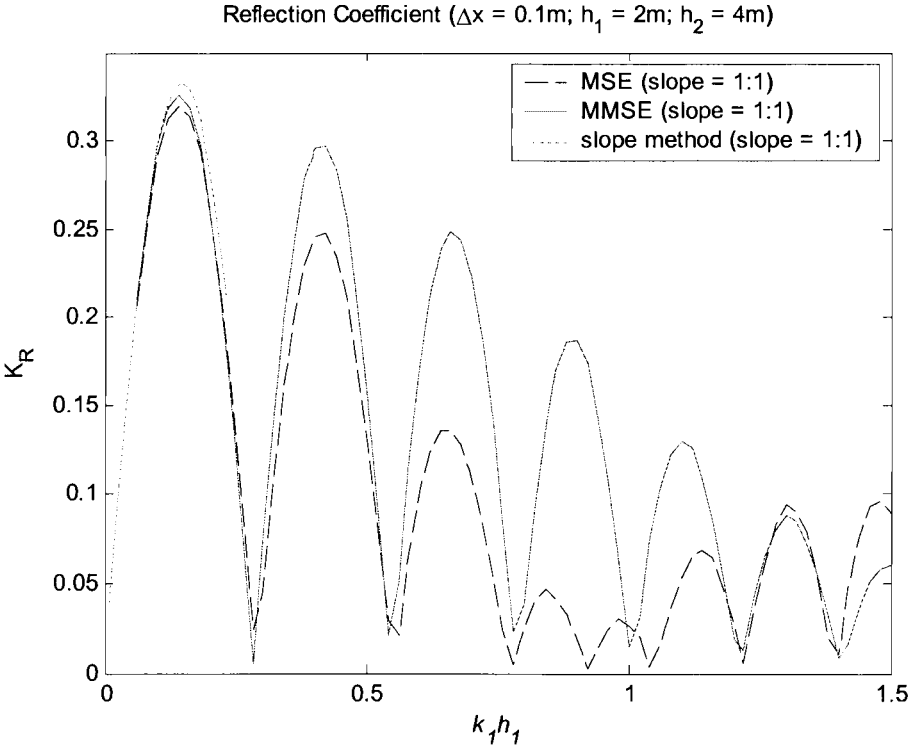

Figure 3.15: Comparison in reflection coefficient for a slope = 1:1; Δx = 0.1m
__ = MMSE model; --- = MSE; ... = Bender 2003 (slope method)

peaks in K_r is greater for the trench with a sidewall slope of 0.1:1 than for the sidewall slope of 1:1.

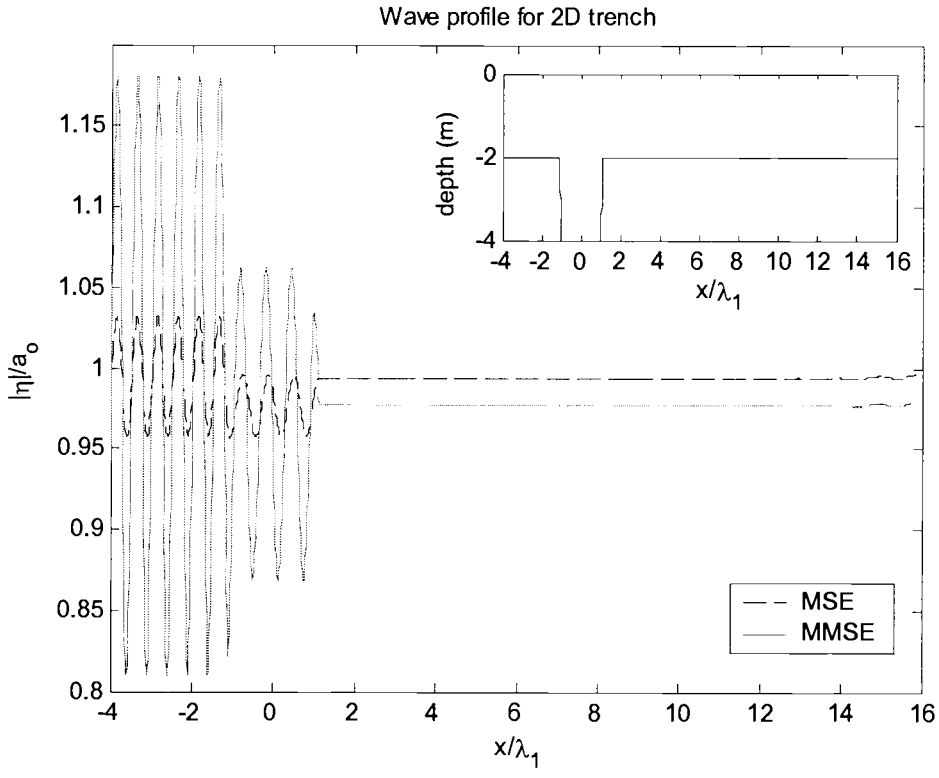

Figure 3.16: Cross-shore wave profile for trench with 1:1 sloping sidewalls using the MMSE and MSE model types. $k_1h_1 = 0.88$, $\bar{a}/h_1 = 15$, $h_2/h_1 = 2$

3.5 Comparison to trench with sidewalls of non-constant slope

The last two-dimensional application of the numerical model is for a trench with exponentially varying sidewall slopes, or a cross-section of a Gaussian shaped pit as illustrated in Figure 3.17. This bathymetry has a smoother transition in depth and can be considered a trench shape that is more representative of a practical dredge site. The bathymetry of the pit cross-section is defined using the following relation

$$h(x) = h_1 + (h_2 - h_1) \cdot e^{-\frac{(x-x_c)^2}{2*\beta_1^2}} \tag{3.16}$$

where x_c is the cross-shore location denoting the center of the trench, a_1 is the top cross-shore width of the trench, and β_1 is a shape parameter controlling the sidewall slopes. The value of β_1 additionally controls the cross-shore extent of the trench. For comparison purposes, the model results are plotted against data taken from Bender (2003, Fig. 5-18) in Figure 3.18. The value of β_1 = 12 results in an equal cross-sectional area as that used in § 3.4.

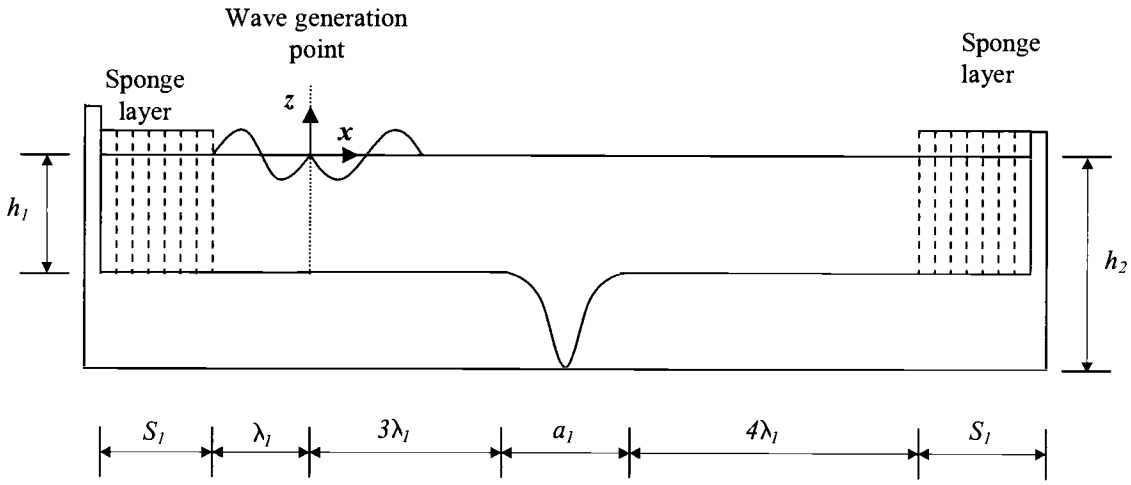

Figure 3.17: Domain considered in numerical model for Gaussian trench shape

Table 3.5: Gaussian trench MMSE results; h_1 = 2m, h_2 = 4m, Δx = 0.1 m

β	$(\nabla h)^2_{max}$	$(\nabla^2 h)_{max}$	$(K_r)_{max,MMSE}$	$kh_{@\,max}$	j_{min}/j_{max}	*Max Slope*
12	1.02×10^{-2}	6.40×10^{-3}	0.2493	0.09	1/1	0.1: 1
2	3.67×10^{-1}	2.24×10^{-1}	0.2237	0.48	1/1	0.6:1

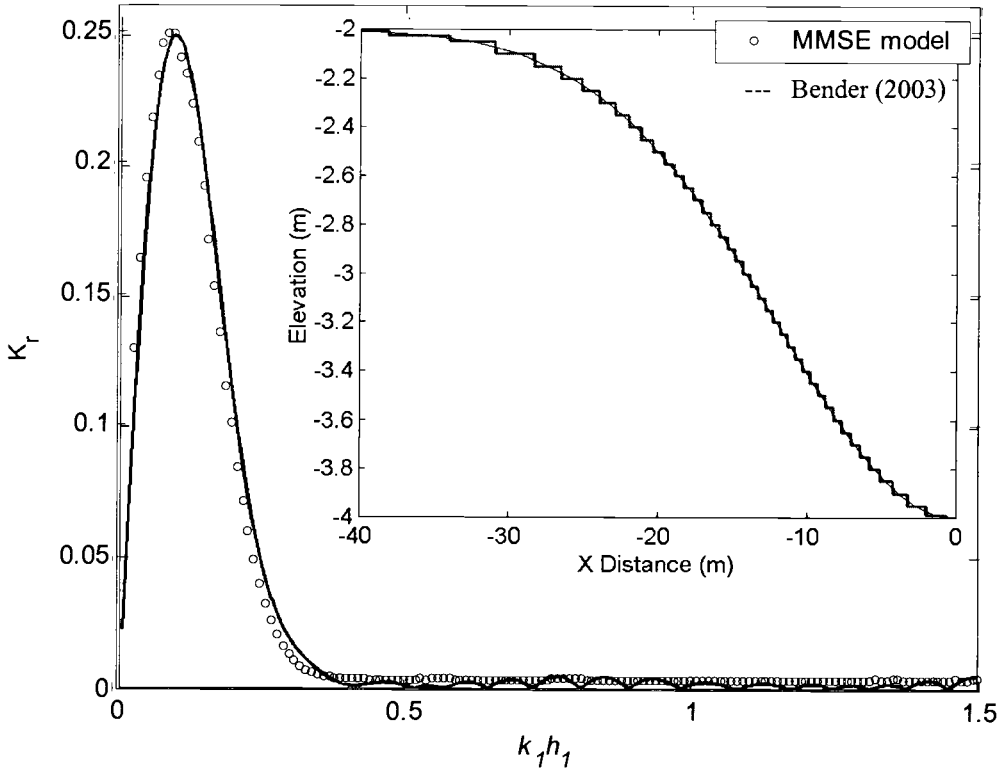

Figure 3.18: Gaussian trench with shape parameter β_1 = 12. o = MMSE model, __ = step method (modified from Bender 2003, Fig. 5-18)

The model matches directly with the results from Bender (2003). For this case only one distinct broad peak in K_r results; reflection for the higher frequency waves ($k_1h_1 > 0.5$) is negligible. In addition, the MMSE formulation is compared with its MSE counterpart (i.e. $R_1 = R_2 = 0$) for two different Gaussian trench shape parameters β_1 = 12 and β_1 = 2. Figure 3.18 shows that the MSE does an adequate job in predicting the amount of reflection generated for a Gaussian shaped trench that is gradually varying (i.e. β_1 = 12). This can be attributed to the bottom curvature and sloped squared terms holding such a small magnitude for this trench as listed in Table

3.5. However, when the trench becomes more narrow in width (i.e. $\beta_1 = 2$), the sidewall slope increases and the higher order bottom terms play a more important role in the solution. For $\beta_1 = 12$ the maximum sidewall slopes of the trench are 0.1:1, whereas for $\beta_1 = 2$ the maximum slopes steepens to 0.6:1. The differences in wall steepness lead to noticeable differences in the solutions of the MMSE and MSE models.

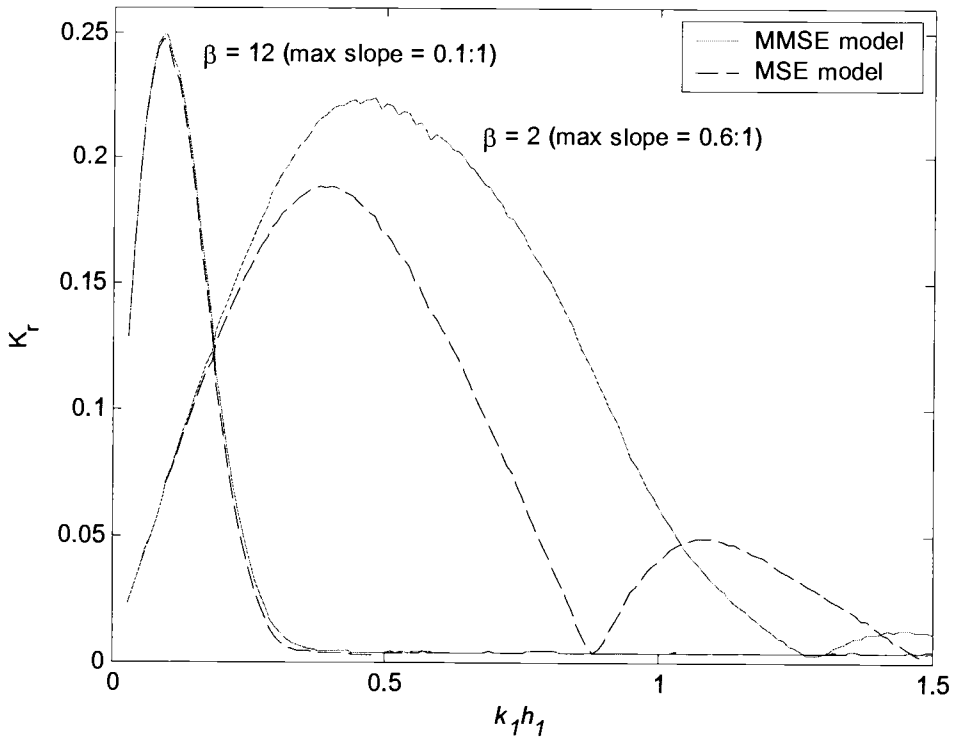

Figure 3.19: Comparison between the MMSE and MSE predictions for a Gaussian trench with $\beta_1 = 12$ and $\beta_1 = 2$; $h_2/h_1 = 2$, and $\bar{a}/h_1 = 15$

The two-dimensional analysis in this section serves as a test on the limitations of the numerical model, particularly the limitation on the sidewall slope that the model can accurately represent. Since the numerical implementation creates problems when trying to discretize trenches that have sharp corner points, it is hard to compare the model with previous analytical work. However, it is shown that the model produces adequate results in the reflection coefficient for a trench with sidewall slopes as large as 1:1. Therefore a sidewall slope of 1:1 is considered the sidewall slope limit for a trench/pit in the remaining analysis.

3.6 Application of model to idealized field cases

3.6.1 Offshore borrow sites

Having a general sense on the capabilities and limitations of the model allows its application to actual scenarios. In reality, the maximum sidewall slope for an offshore borrow site in the field is limited by the angle of repose of the sediment at the site. However in the case of nearshore canyons (i.e. NCEX), since these features are often rocky the slope could possibly be larger. Nevertheless, the main focus of the study is the offshore borrow site. Allen (1970) lists the angle of repose for sediment in water for various grain sizes of typical quartz beach sand. The angle of repose ranges from $\phi = 44.6°$ to 53.1°, which is approximately a slope of 1:1. Therefore, having the limitation on the sidewall slope of 1:1 for a trench in the numerical model is not unreasonable. Referring back to the offshore borrow pits listed in Table 1.1, the model is used to estimate the amount of reflection that would occur for the given wave conditions. Generally, longer wave periods produce the most amount of reflection since they correspond to the lower k_1h_1 values, which is consistent with the preceding analysis. Additionally, reflection is also a function of the top and bottom cross-shore widths of the trench a_1 and a_2. This is shown to shift where the peaks in the reflection coefficient occur in k_1h_1.

Since the exact bathymetry for the cases is not readily available and reflection is mainly influenced by the cross-shore dimension of the trench, the simplification of the problem to two-dimensions is justified. The MMSE and MSE models are run for each field case listed in Table 1.1 for trench sidewall slopes of 0.1:1 and 1:1. This serves as a general set of bounds for the sidewall slopes that most likely would occur. Tables 3.6 and 3.7 provide the results for each respective sidewall slope scenario. For the given conditions, many of the relative water depths fall close to the shallow water limit (i.e. $k_1h_1 = \pi/10$). For the gradually sloping sidewall (slope = 0.1:1) the reflection coefficient is seen to be relatively small in magnitude with the exception of the cases at Grand Isle, LA and Edisto Island, SC which both exhibit reflection coefficients over 15%. The differences between the MMSE and MSE models are not predominantly significant for any of the cases which can be attributed to the fact that the bathymetry

can be considered as slowly varying topography according to Booij (1983). In addition, the relative water depth k_1h_1 is near the shallow water limit, which is shown to produce similar results between the MMSE and MSE.

For the set of runs using sidewall slopes of 1:1, the magnitude in the reflection coefficient exceeds 30% for Grand Isle, LA, Gaskin Banks, SC, and Hunting Island, SC. This amount of reflection would affect the wave climate significantly, and is an event that should be included by any wave model being used to simulate the process. For most of the cases the MSE model predicts a very similar K_r, the largest difference is approximately 4% in absolute magnitude. The reason why this occurs is because many of the borrow pits have relative water depths values k_1h_1 which correspond to the first peak in K_r. Referring back to Figure 3.15 the differences between the MMSE and MSE in K_r were most apparent for the subsequent peaks (i.e. intermediate depth region). However, even though the two models agree relatively well using the present hyperbolic solution, the use of a parabolic MSE model (neglecting reflection entirely) would be in error. The reason Grand Isle, LA, Gaskin Banks, SC, and Hunting Island, SC are special is because the k_1h_1 associated with each borrow pit happens to fall relatively close to the peak in K_r. Thus reflection is more significant for these cases than for the others listed. From a more practical sense, this demonstrates the importance of the features geometry and the incident wave conditions on the resultant wave field.

Table 3.6: Results for idealized trenches using dimensionless parameters (slope = 0.1:1, Δx = 0.1m, j = 1)

	k_1h_1	k_2h_2	$\bar{a}/h_1$	$\bar{a}/\lambda_1$	h_2/h_1	K_r (MMSE)	K_r (MSE)
(1a) Genkai Sea, Japan (lower limit) Kojima et al. (1986)	0.901	1.028	76.9	9.5	1.2	0.0365	0.0133
(1b) Genkai Sea, Japan (upper limit) Kojima et al. (1986)	1.195	1.403	50	11.0	1.3	0.0045	0.0020
(2a) Grand Isle, LA (1983) – (channel) Combe & Soileau (1987)	0.312	0.408	100	5.0	1.7	0.1815	0.1741
(2b) Grand Isle, LA (1983) – (bells) Combe & Soileau (1987)	0.312	0.487	100	5.0	2.3	0.0662	0.0599
(3) Anna Maria Key, FL (1993) Dean et al. (1999)	0.458	0.574	56.7	4.0	1.5	0.0126	0.0074
(4) Delray Beach, FL (1973-99) Fernandez (1999)	0.562	0.618	18.8	1.7	1.2	0.0225	0.0174
(5) Gaskin Banks, SC (1990) Van Dolah et al. (1998)	0.255	0.362	387.1	15.7	2.0	0.1306	0.1218
(6) Joiner Banks, SC (1991) Van Dolah et al. (1998)	0.224	0.343	208.3	7.4	2.3	0.0433	0.0449
(7) Edisto Island, SC (1995) Van Dolah et al. (1998)	0.219	0.323	66.7	2.3	2.1	0.1567	0.1505
(8) Hunting Island, SC (1991) Van Dolah et al. (1998)	0.358	0.540	81.9	4.6	2.2	0.0410	0.0374
(9) Seabrook Island, SC (1990) Van Dolah et al. (1998)	0.251	0.312	66.7	2.7	1.5	0.1485	0.1408

Table 3.7: Results for idealized trenches using dimensionless parameters (slope = 1:1, Δx = 0.1m, j = 2)

	k_1h_1	k_2h_2	$\bar{a}/h_1$	$\bar{a}/\lambda_1$	h_2/h_1	K_r (MMSE)	K_r (MSE)
(1a) Genkai Sea, Japan (lower limit) Kojima et al. (1986)	0.901	1.028	76.9	9.5	1.2	0.0605	0.0252
(1b) Genkai Sea, Japan (upper limit) Kojima et al. (1986)	1.195	1.403	50	11.0	1.3	0.0508	0.0144
(2a) Grand Isle, LA (1983) – (channel) Combe & Soileau (1987)	0.312	0.408	100	5.0	1.7	0.2329	0.2225
(2b) Grand Isle, LA (1983) – (bells) Combe & Soileau (1987)	0.312	0.487	100	5.0	2.3	0.3293	0.3146
(3) Anna Maria Key, FL (1993) Dean et al. (1999)	0.458	0.574	56.7	4.0	1.5	0.0651	0.0556
(4) Delray Beach, FL (1973-99) Fernandez (1999)	0.562	0.618	18.8	1.7	1.2	0.0371	0.0260
(5) Gaskin Banks, SC (1990) Van Dolah et al. (1998)	0.255	0.362	387.1	15.7	2.0	0.3152	0.2957
(6) Joiner Banks, SC (1991) Van Dolah et al. (1998)	0.224	0.343	208.3	7.4	2.3	0.1014	0.0970
(7) Edisto Island, SC (1995) Van Dolah et al. (1998)	0.219	0.323	66.7	2.3	2.1	0.2510	0.2383
(8) Hunting Island, SC (1991) Van Dolah et al. (1998)	0.358	0.540	81.9	4.6	2.2	0.3376	0.2953
(9) Seabrook Island, SC (1990) Van Dolah et al. (1998)	0.251	0.312	66.7	2.7	1.5	0.1778	0.1678

3.6.2 NCEX trenches

Another application of the model is used to investigate the reflection generated from the nearshore trenches studied in the NCEX experiment. The Scripps canyon is approximated to have sidewall slopes of 1.1:1, while the La Jolla canyon approximately has sidewall slopes of 0.6:1. Figure 3.20 shows two transects approximately perpendicular to the two trenches. The depth profiles for these transects are shown in Figure 3.21 which also includes the idealized trench used to represent each in the numerical model. The dimensions used for the idealized trench are listed in Table 3.8. In order to illustrate the differences between the MMSE and MSE for multiple wave conditions, K_r is plotted versus k_1h_1 for each canyon in Figures 3.22 and 3.23. It is seen that for the swell conditions ($k_1h_1 = 0.823$ and $k_1h_1 = 0.945$), the prediction of K_r is considerably different. For La Jolla canyon, the peak in K_r at $k_1h_1 = 0.823$ using the MMSE almost lines up with the minima in K_r using the MSE model; here a 7% difference between the models is shown. Conversely, the MSE over predicts the amount of reflection by 6% for Scripps canyon. The results also illustrate that for certain wave conditions and trench sidewall slope combinations, wave reflection can be important (particularly long waves). Therefore, numerical models neglecting reflection may substantially over predict the amount of wave energy in lee of the feature.

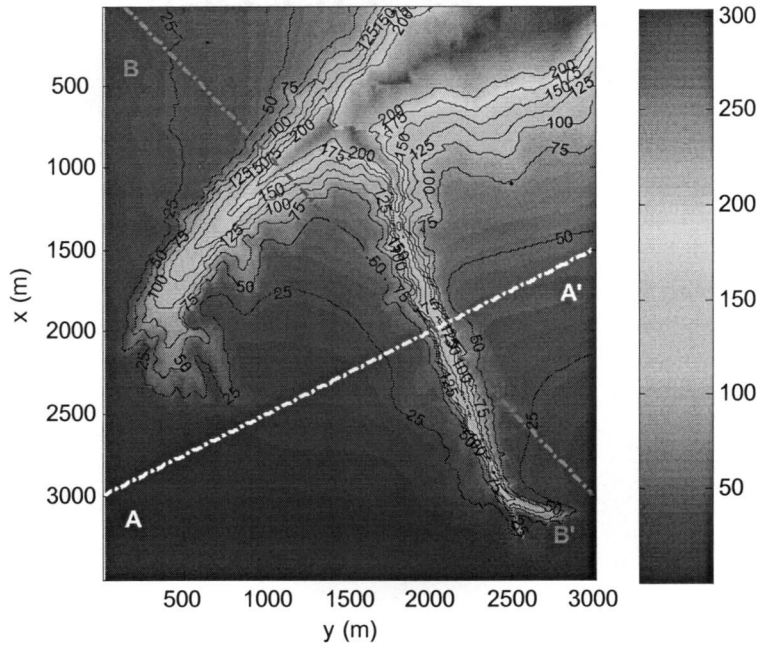

Figure 3.20: Planform showing cross-sections used to represent NCEX trenches

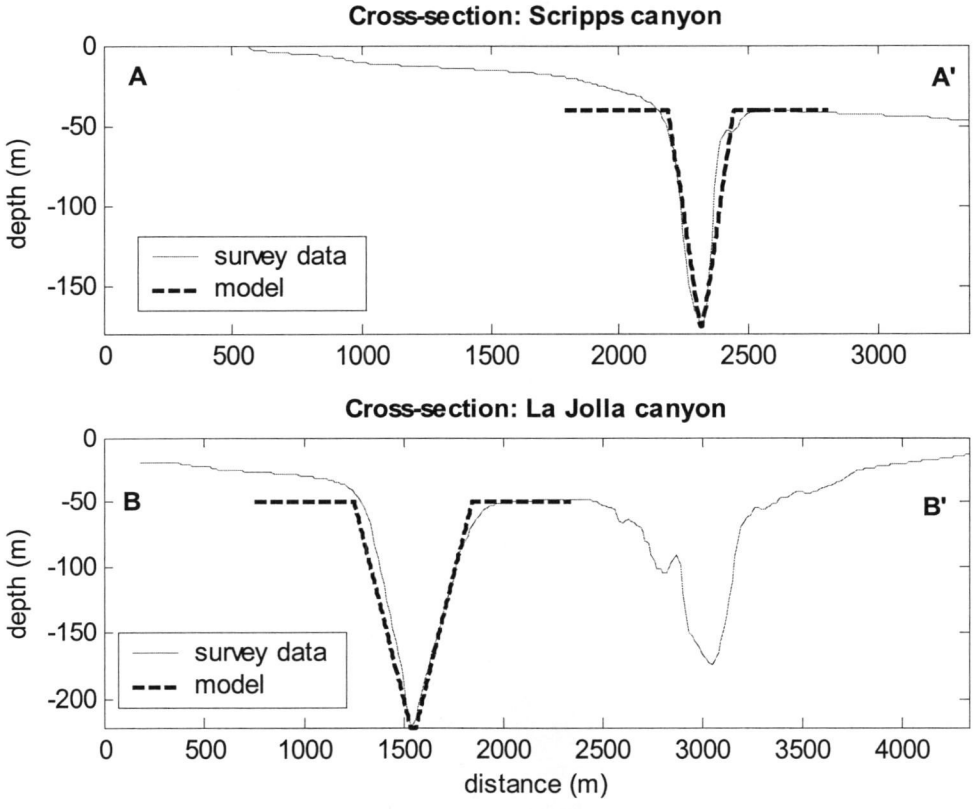

Figure 3.21: Trenches used to represent profile data in numerical model. Cross section through **(a)** A—A' Scripps canyon **(b)** B—B' La Jolla canyon

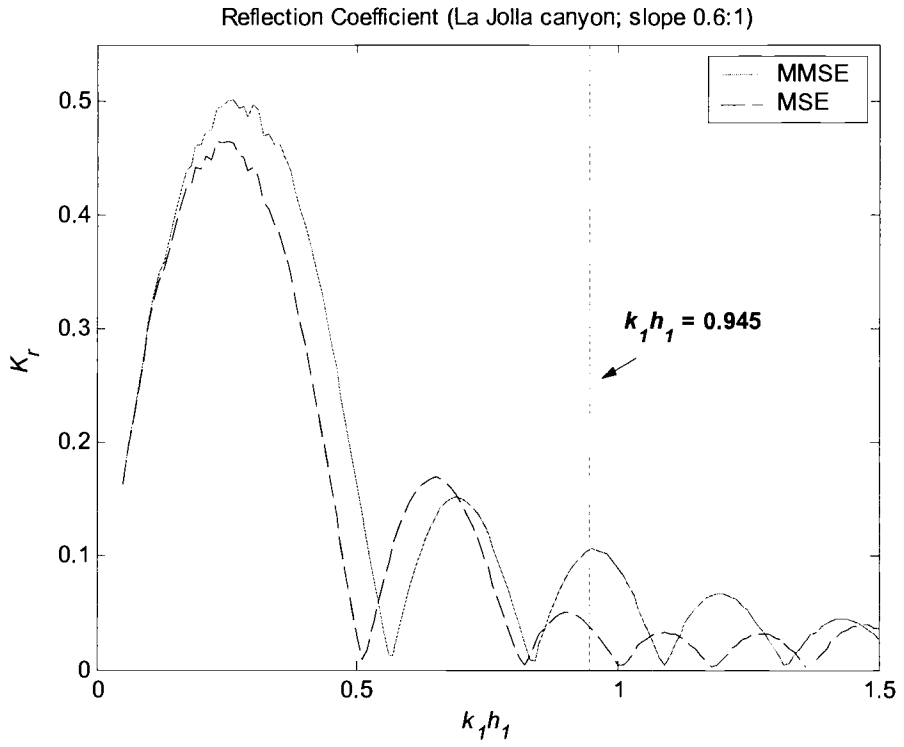

Figure 3.22: Theorized reflection generated from La Jolla canyon; __ = MMSE model, — — = MSE model

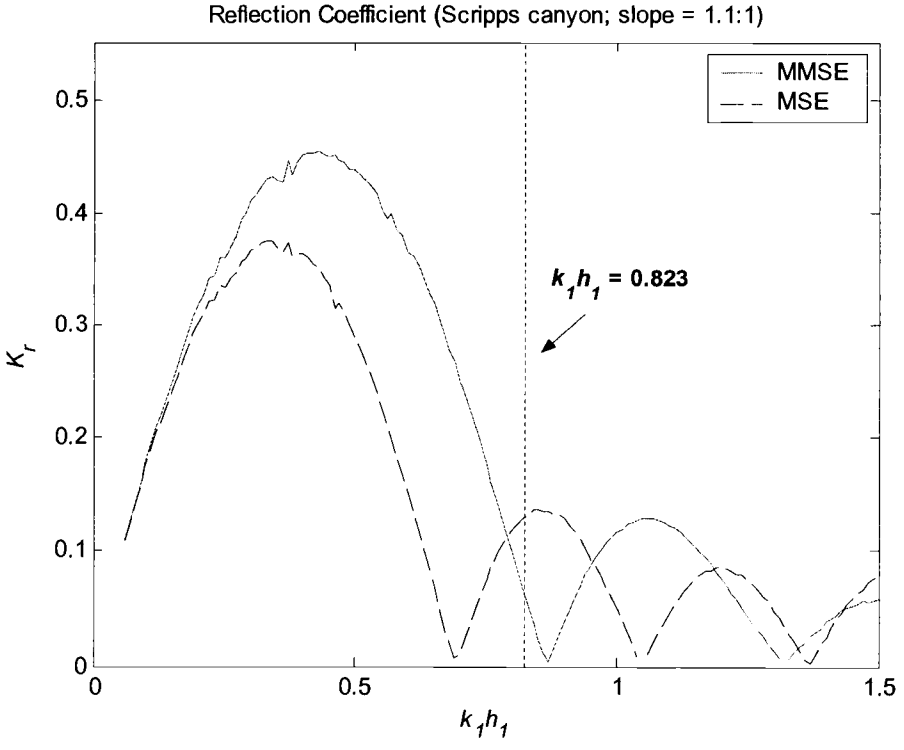

Figure 3.23: Theorized reflection generated from Scripps canyon; __ = MMSE model, — — = MSE model

Table 3.8: Results for idealized NCEX trenches using dimensionless parameters ($\Delta x = 0.1\text{m}, j = 1$)

	Slope (rise:run)	k_1h_1	k_2h_2	$\bar{a}/h_1$	$\bar{a}/\lambda_1$	h_2/h_1	K_r (MMSE)	K_r (MSE)
(1) Scripps Canyon (NCEX)	1.1:1	0.823	2.473	3.3	0.5	4.4	0.0674	0.1271
(2) La Jolla Canyon (NCEX)	0.6:1	0.945	3.077	6.2	0.9	4.4	0.1065	0.0365

3.7 Parameterization analysis

Another interest of the current study is to quantify the importance of reflection in terms of dimensionless geometric properties. As demonstrated in the previous analysis, wave reflection is dependent on the dimensionless relative water depth *kh*. For the case of an infinitely long trench, the magnitude of the reflection coefficient is shown to fluctuate over *kh*. The location of the maxima and minima of K_r in *kh* are further influenced by the trench width, sidewall slopes, and relative depth. The variable nature of K_r over *kh* is analogous to previous studies looking at Bragg resonance over ripple beds (i.e. sinusoidal shaped sandbars) placed one after another (e.g. Davies and Heathershaw 1984; Mei 1985; Kirby 1986). Davies and Heathershaw (1984) show that specific wave frequencies associated with peaks in reflection exist. For a sinusoidal ripple bed, the theoretical peak reflection coefficient occurs at l/λ_l = 0.5, where l is the wavelength of the ripple bed and λ_l is the surface wavelength. Additionally, the reflection coefficient is oscillatory about the ratio of the total cross-shore width of the ripple bed patch to the surface wavelength. An illustration of this is shown in Figure 2.9. In the current study a similar relation describing the resonant nature of wave propagation over a trench with sloping sidewalls is sought. Like the ripple bed case, the peaks in the reflection coefficient occur at regular intervals in *kh*, and therefore ought to be related by some form of dimensionless parameterization. For a trench, the dimensionless parameters considered to represent the resonant nature in K_r, are the ratio of the mean cross-shore pit width to the surface wavelength outside the pit ($\bar{a}/\lambda_1$) as well as the ratio of the width to wavelength associated with the water depth inside the pit ($\bar{a}/\lambda_2$). These parameters may be backcalculated following the calculation of K_r as a function of k_1h_1 or k_2h_2. Using the analysis in § 3.6 an estimated range of practical trench geometries can be inferred. From Table 2.6, an approximate upper and lower limit of the relevant parameters describing the trench geometry is: $20 \leq \bar{a}/h_1 \leq 400$ and $1.2 \leq h_2/h_1 \leq 2.4$. Figures 3.24 to 3.26 illustrate the dependency of the relative trench depth as well as the trench sidewall slope on $\alpha_1 = \bar{a}/\lambda_1$, $\alpha_2 = \bar{a}/\lambda_2$, and $(K_r)_{max}$ using three different relative trench widths $\bar{a}/h_1 = 20$, 100, and 400.

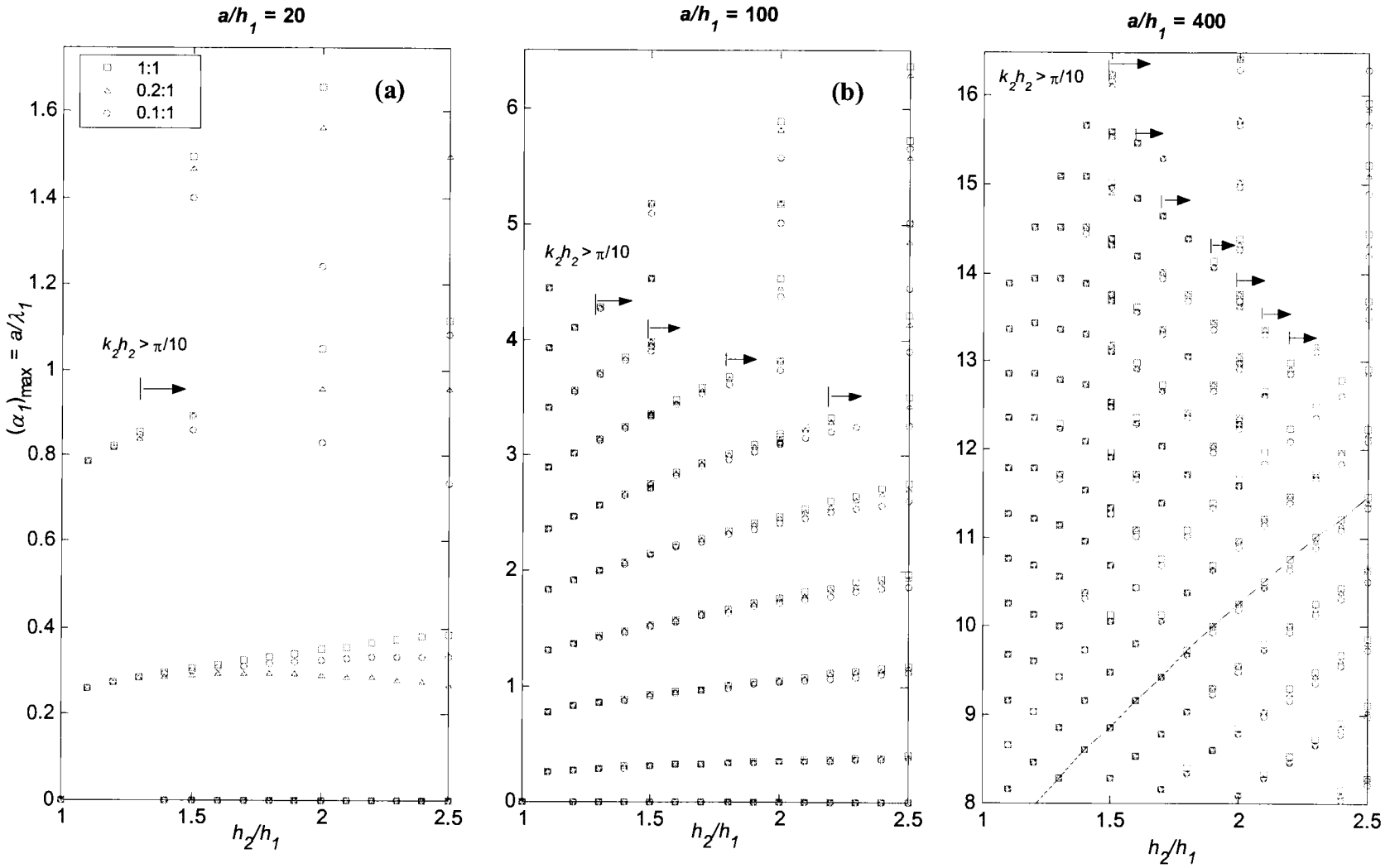

Figure 3.24: Evolution of $\alpha_1 = \bar{a}/\lambda_1$ in the transition from shallow to intermediate depth; $\bar{a}/h_1 =$ **(a)** 20 **(b)** 100 **(c)** 400

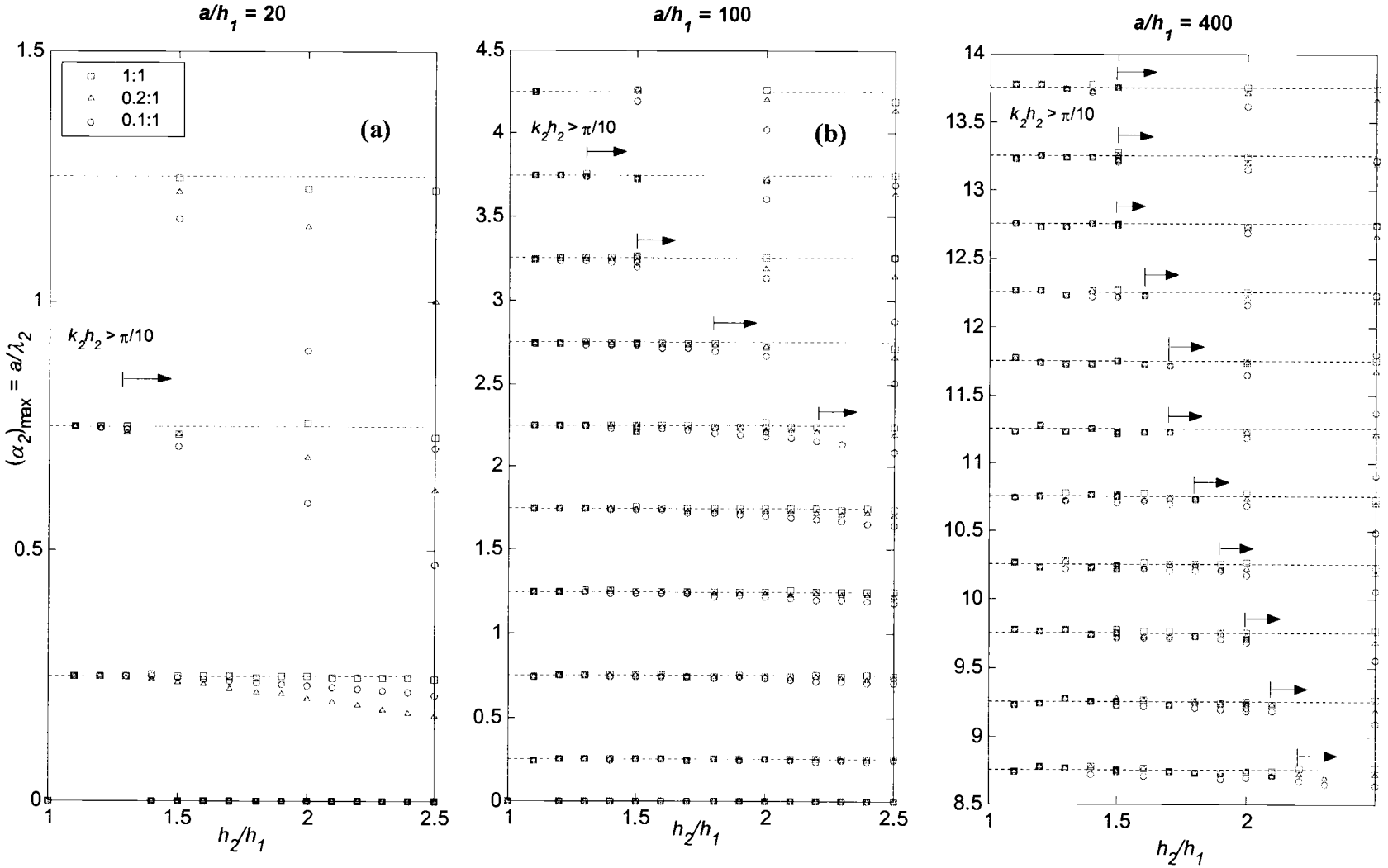

Figure 3.25: Evolution of $\alpha_2 = \bar{a}/\lambda_2$ in the transition from shallow to intermediate depth; $\bar{a}/h_1 =$ **(a)** 20 **(b)** 100 **(c)** 400

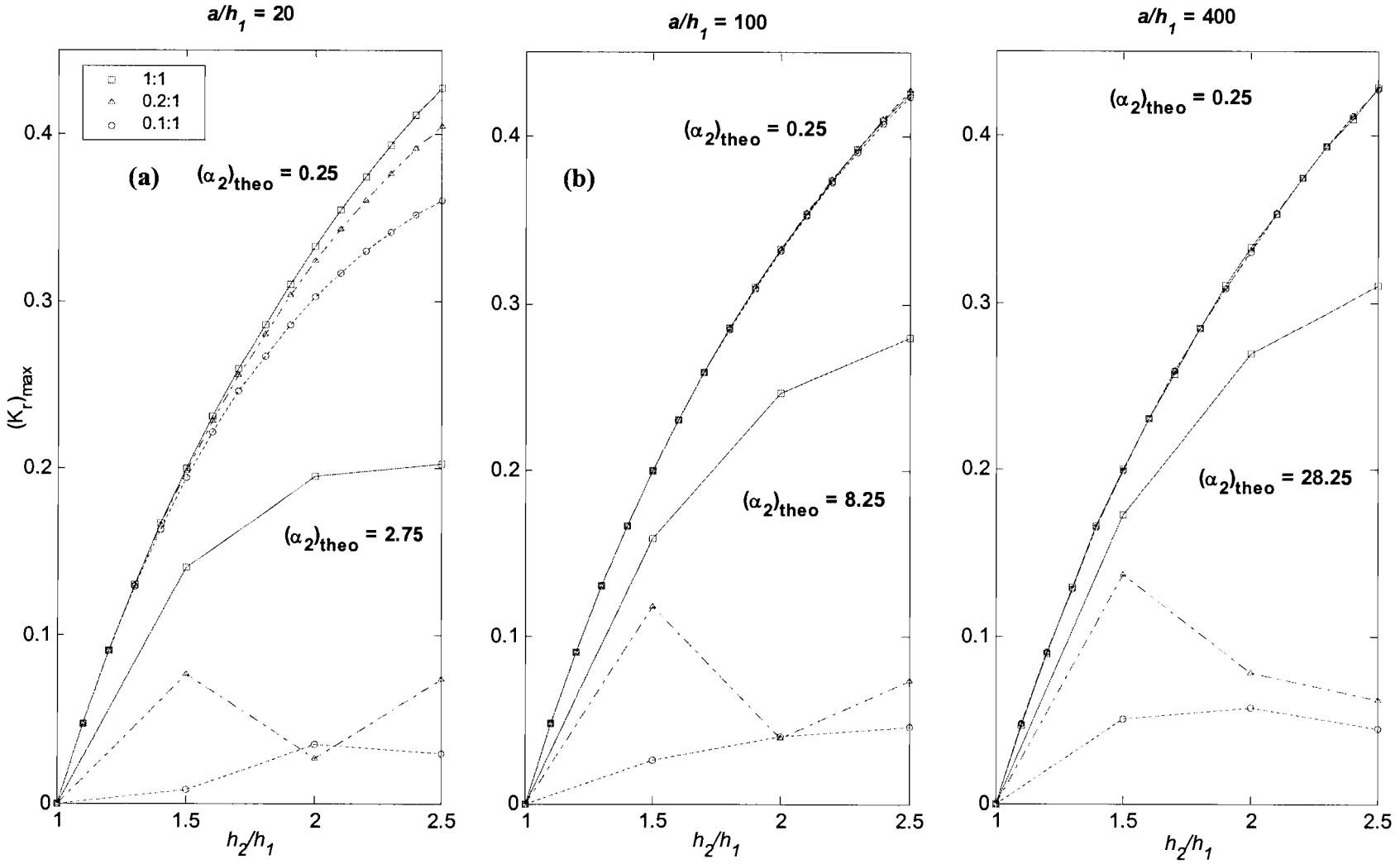

Figure 3.26: Peak reflection coefficient versus relative trench depth for various sidewall slopes; $\bar{a}/h_1$ = **(a)** 20 **(b)** 100 **(c)** 400

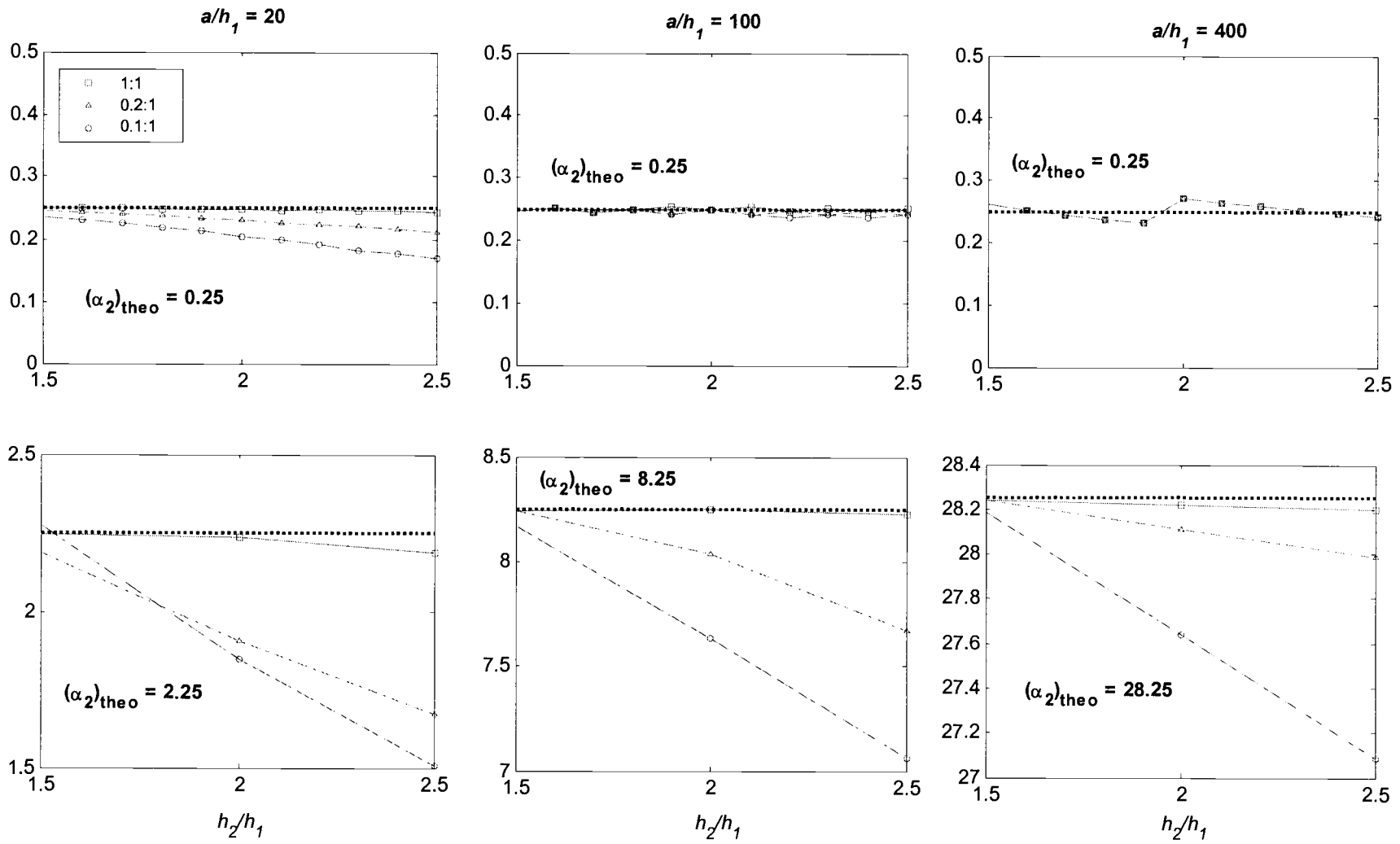

Figure 3.27: α_2 enlarged for upper and lower bounds given in Figure 3.25; $\bar{a}/h_1$ = **(a)** 20 **(b)** 100 **(c)** 400

Trenches with sidewall slopes of 0.1, 0.2, and 1:1 are used in the analysis. In the shallow water region of $k_2h_2 \leq \pi/10$ the long wave approximation or "slope method" from Bender (2003) is implemented. Here the results from the MMSE numerical model and those using the slope method compare very well and since the computational time required by the analytic solution is significantly smaller, this solution is employed to calculate α_1, α_2, and $(K_r)_{max}$ in the shallow water region. The use of the solution allows for the calculation of these parameters at more h_2/h_1. The numerical model is then implemented for three relative trench depths $h_2/h_1 = 1.5$, 2.0, and 2.5 for $k_2h_2 < \pi$. The results using this model extend the results into the intermediate depth region (i.e. $\pi/10 \leq k_2h_2 \leq \pi$). The arrows in Figures 3.24 and 3.25 designate the specific relative trench depth h_2/h_1 where the intermediate depth region begins.

The constant value of α_2 in Figure 3.25 illustrates that there exists specific resonant conditions where in k_2h_2 the peaks in the reflection coefficient $(K_r)_{max}$ occur. The resonant conditions in shallow water closely follow the relation

$$\alpha_2 = 0.25 + 0.5n; \quad n = 1...\infty \tag{3.20}$$

where integer n designates the number of subsequent peaks following the first peak in K_r. These theoretical values are denoted by the dotted lines in Figure 3.25. This corresponds to the $(\alpha_2)_{theo}$ for the case of a rectangular trench with vertical sidewalls in shallow water. The number n over a specific range in k_1h_1 is proportional to the relative trench width $\bar{a}/h_1$ (or in other words, there exist more peaks in K_r for wider trenches). It is evident that characteristics describing the trench influence the value of α_2. For one, the sidewall slope has a significant influence on α_2 as h_2/h_1 is increased, especially for narrow trench width ($\bar{a}/h_1$) as shown in Figure 3.25 (a). A sidewall slope of 1:1 is shown to maintain a relatively constant magnitude in α_2 with only a slight deviation from the theoretical value even in the transition to intermediate depths. Yet, as the trenches sidewall slope becomes more gradual, a significant deviation from the theoretical value is witnessed.

The magnitude of reflection is the main reason for the analysis. Therefore tracking the magnitude in K_r associated with each peak is important. If reflection is below 5%, the influence of the trench on the wave field is most likely minimal. However, in cases with larger K_r the wave field will be substantially modified and the impacts from this on shoreline morphology may be evident. Figure 3.26 illustrates the magnitude of K_r for the largest peak and the smallest peak within the range of $k_1h_1 \leq 1.5$ as a function of relative trench depth h_2/h_1. The figure shows the dependency of the trench width $\bar{a}/h_1$ on the α_2 required to achieve minimal reflection. For wider trenches, α_2 is much larger in a defined range of k_1h_1 than for narrower trenches. This is because many more peaks in K_r exist for wider trenches within the same range of k_1h_1. This effect is demonstrated in Figure 3.28 for a trench with sidewall slopes of 0.2:1 and relative trench widths of $\bar{a}/h_1 = 20$ and $\bar{a}/h_1 = 400$.

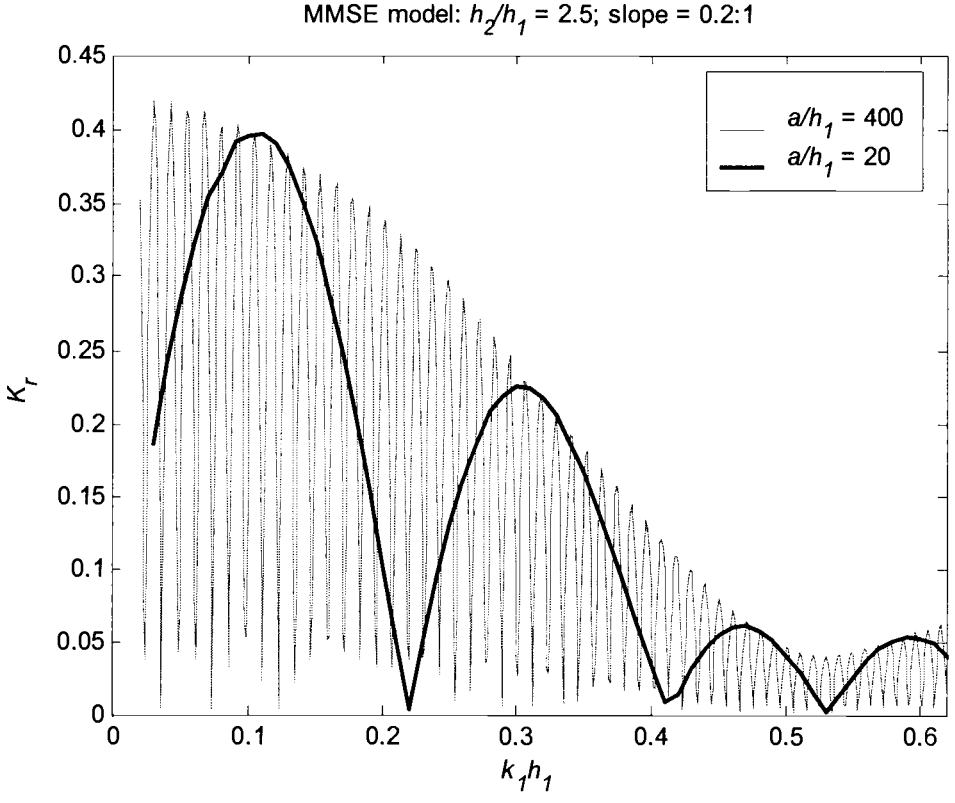

Figure 3.28: Resonance of reflection coefficient over k_1h_1 for narrow ($\bar{a}/h_1 = 20$) versus wide ($\bar{a}/h_1 = 400$) trench

It is interesting to note that the peaks in K_r for $\bar{a}/h_1 = 20$ have the same magnitude in K_r as the peaks in K_r for $\bar{a}/h_1 = 400$. However for $\bar{a}/h_1 = 400$, there are many more possible k_1h_1 values capable of producing reflection. In the other limiting case, as the trench becomes very narrow one broad peak in K_r exists. This was originally pointed out by Lee and Ayer (1981). Therefore as a general rule of thumb for avoiding the presence of reflection, it would be easiest to implement a pit with cross-shore width somewhere in between the two extremes. Here the peaks in K_r are spaced adequately enough to select a k_1h_1 value that produces minimal reflection.

The curves in Figure 3.26 (a) through (c) bound a region that represents possible cases where reflection would significantly affect the wave field. The top curves represent the largest peak in reflection $(K_r)_{max}$ that is generated in all k_1h_1 (i.e. at $\alpha_2 = 0.25$). It is seen that the trench sidewall slope only affects the top curves for the narrow trench case with $\bar{a}/h_1 = 20$. The lower set of curves represents the value α_2 when the peak in reflection $(K_r)_{max} < 0.05$ for a trench with sidewall slopes of 0.1:1. For each set of curves the value of α_2 in Figure 3.27 is enlarged. From this figure it is easier to see the effect of the sidewall slope as h_2/h_1 increases. Another point this analysis demonstrates is that increasing the cross-shore width of the trench does not make the magnitude of reflection coefficient negligible. In fact, since more waves fit in a trench with a wider cross-section, the possibilities of reflection for wider trenches is increased. This can be seen again in Figure 3.26. For example, for $\bar{a}/h_1 = 100$ ($\alpha_2 = 8.25$) there exist almost four times as many wave conditions capable of producing significant reflection then for the case with $\bar{a}/h_1 = 20$ ($\alpha_2 = 2.75$). This increases to over ten times for the case of $\bar{a}/h_1 = 400$ ($\alpha_2 = 28.25$).

In summary, in order to use this analysis for a practical design of a borrow pit, the values of α_2 given in Figure 3.25 should be avoided. The frequency of the waves for a certain area is the fixed parameter, thus the selection of the cross-shore width, sidewall slope, and relative trench depth must be tailored to accomplish the criterion. If this is unachievable, Figure 3.26 can be used to determine an approximate estimate of the reflection that is associated with the parameter α_2. For larger values of α_2, reflection may be minimal and its effects on the wave climate may be considered unsubstantial based on the reasoning of the designer.

4.0 Two-dimensional methods and background

The extension of the model to two horizontal dimensions allows the study of more representative borrow pit geometries. Williams (1990) and McDougal et al (1996) show the important effect of the anomaly having a finite longshore extent influencing the amount of refraction and diffraction that occurs. The longshore discontinuity of a pit is shown to refract waves away from the trench centerline creating a depressed shadow region with significantly smaller wave heights than found in the incident wave directly leeward of the pit. Bender (2003) goes further to investigate the impacts of gradually sloping pit sidewalls and Gaussian shaped pits. Although these studies provide exact solutions for the wave field around finite anomaly shapes, the solutions require highly idealized borrow pit shapes as well as a constant depth surrounding the anomaly. Therefore in cases where bathymetry is arbitrary these solutions are not applicable. In this section the MMSE model will be used to simulate the wave field around practical borrow pit geometries by studying geometries similar to those documented in the field.

4.1 Analytical solutions for a finite pit

In order to more accurately represent an offshore borrow pit, two horizontal dimensions must be included in the solution. Williams (1990) and Williams and Vazquez (1991) utilized a Green's function approach to analyze the wave transformation over a rectangular pit in water of otherwise constant depth. The first study formulated a shallow water approximation, whereas the second removed the long-wave restriction to study pits located in all water depths. As in the two dimensional case the fluid in the boundary was separated into two regions: one inside the pit and one outside the pit. However, in this case the common boundary between the two regions consists of a rectangular projection (instead of a line) denoted as Γ in Figure 4.1. The velocity potential in each region is depth-averaged, rendering a solution in two-horizontal dimensions that does not include the true vertical dependency. The solution is found by applying standard matrix techniques. Bender

(2001) later employed this solution to study pits of cylindrical shape through the modification of the boundary conditions.

The results using these solution types showed that a shadow region of low wave energy (relative to the incident wave energy) is created leeward of the anomaly and is surrounded by alternating areas of high and low wave energy. The ratio of the incident wave height to the wave height elsewhere (i.e. relative amplitude) is referred to as the diffraction coefficient by McDougal et al. (1996). A partial standing wave seaward of the pit also results from the wave reflection off the pit sidewalls. Utilizing the properties of the resultant wave field, McDougal et al. (1996) applied the approach of Williams (1990) and presented design guidance for the use of multiple pits as a new type of breakwater. For a single pit, Figure 4.2 illustrates the scattering of wave energy off the longshore pit edges producing a longshore fluctuation in relative wave amplitude. The shadow region exhibits the smallest magnitude directly behind the pit, while wave heights become slightly larger at a further distance from the pit due to the presence of diffraction seeping energy back into the region. The convention of the parameters describing the pit dimensions are consistent with those used in Tables 1.1 through 1.3.

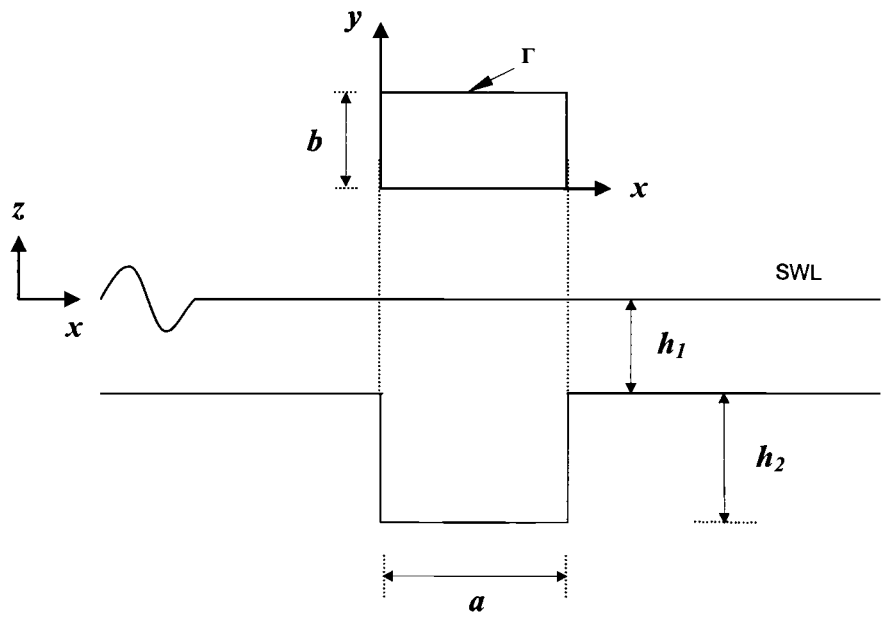

Figure 4.1: Definition sketch for rectangular pit

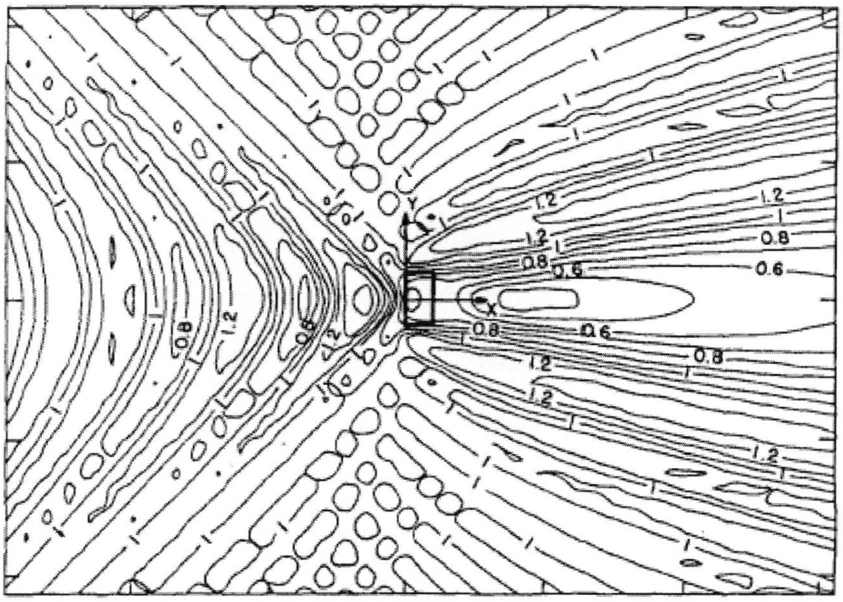

Figure 4.2: Diffraction coefficient for rectangular pit with dimensions: $a/\lambda = 0.5$, $b/\lambda = 1.0$, $h_2/h_1 = 3$, $k_1h_1 = 0.167$ (from McDougal et al. 1996)

Lee et al. (2002) further investigated the influence of multidirectional random waves on rectangular pits using Williams (1990) long-wave solution. It was shown that in the case of random wave patterns, the shadow region was less significant. Figures 4.3 (a) and (b) demonstrate the dependency of the minimum and maximum diffraction coefficient on cross-shore pit width a and longshore pit length b, respectively. The minimum diffraction coefficient always occurs directly behind the pit in the shadow region, whereas the maximum value occurs near the longshore edges of the pit as a result of the scattered waves refracting away from the pit. For the case of random waves, the change in magnitude of this coefficient is less pronounced. Additionally, the degree of directional spreading S_{max} seems to only significantly affect the maximum diffraction coefficient for pits widths larger than half the incident wavelength.

These studies illustrate that wave transformation over finite pits is much more complicated than for an alongshore uniform trench. However, most of the studies apply the shallow water approximation (Williams, 1990; McDougal et al., 1996; Lee et al., 2002), limiting the applicability of the conclusions to a small set of cases.

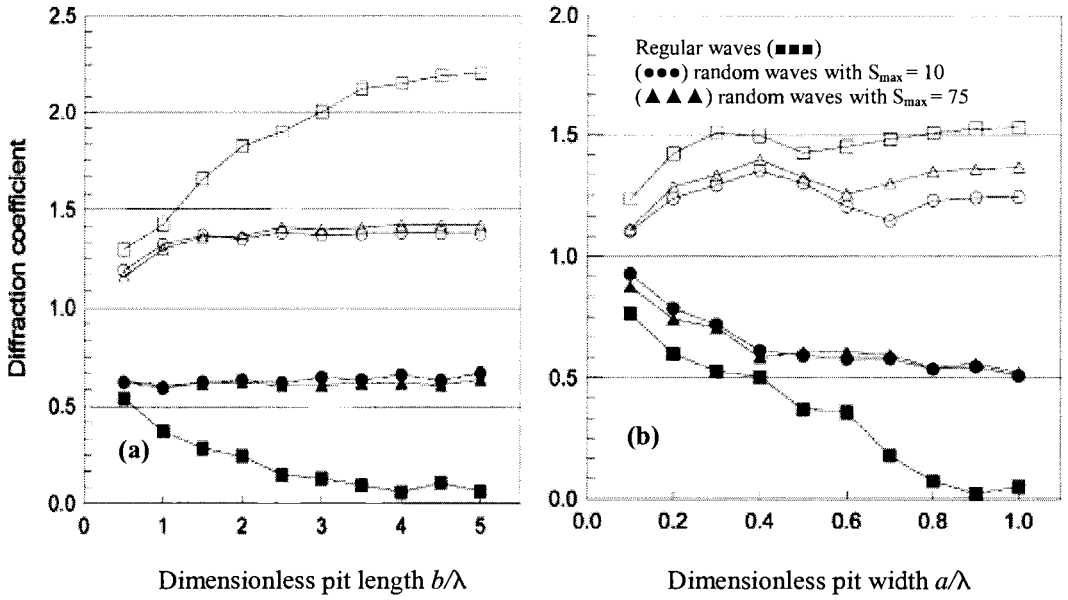

Figure 4.3: Maximum and minimum diffraction coefficients for rectangular pit with $k_1h_1 = 0.167$ and $h_2/h_1 = 3$; for variable pit dimensions **(a)** b/λ and **(b)** a/λ (modified from Lee et al. 2002)

Bender (2003) addresses this problem by extending the step method originally solved for the two dimensional case (i.e. infinitely long trench) to now compensate for finite dimensions. The solution is accurate for a full range of water depths and represents an exact three dimensional solution (i.e. the vertical component is represented without depth integrating). Additionally, the method is capable of solving for the wave field near pits with gradual transitions in depth, another aspect the previous solutions were unable to show. Figure 4.4 shows the solution for the relative amplitude for a gradually sloping truncated cone with a 1:10 sidewall slope. The definition of relative amplitude is identical to the diffraction coefficient used by McDougal et al. (1996). Additionally Bender (2003) couples an analytic nearshore shoaling and refraction method with the step method in order to investigate the evolution of wave height and direction in a surf zone. The method requires wave height and direction to be input along a cross-shore transect at the initiation of the surf zone. The nearshore method then takes over using a beach slope that approximates a typical beach profile (i.e planar beach or equilibrium beach profile). Here the effects of shoaling and refraction are included. In addition, wave breaking is represented

using a depth limited criterion. This allowed the model to be coupled with a shoreline evolution model.

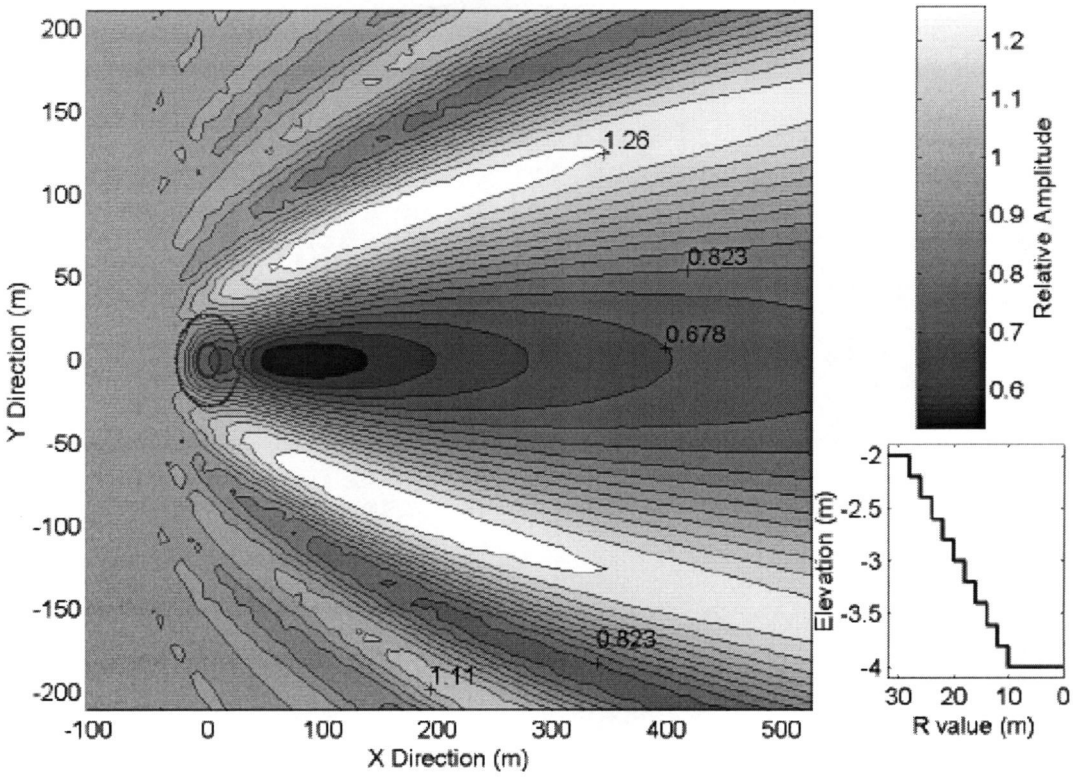

Figure 4.4: Relative amplitude for truncated cone with $k_1h_1 = 0.24$ and sidewall slope = 1:1 (from Bender 2003)

4.2 Numerical applications using the modified mild-slope equation

Previous work using the MMSE has primarily been interested in the reflection generated from an infinitely long feature such as a planar slope, or ripple bed (e.g. Lee et al. 1998). Suh et al. (2001) extends the model to include two-horizontal dimensions and tests the models accuracy against data from a laboratory experiment investigating normally incident waves over a shoal. The maximum slope of the shoal occurs at the base of the shoal and is 0.8:1, which exceeds the mild-slope criterion imposed by Booij (1983). Figure 4.5 illustrates the simulated wave field around the shoal using the numerical model. Figure 4.6 depicts the prediction by the MMSE follows the experimental measurements very well, whereas the prediction by the MSE is shown to

produce significant errors. Additionally, the hyperbolic formulation allows the model to include the effects of backscattered waves offshore of the shoal. The model is advantageous for future applications since the finite difference grid used in the numerical model allows for wave propagation over arbitrary depth.

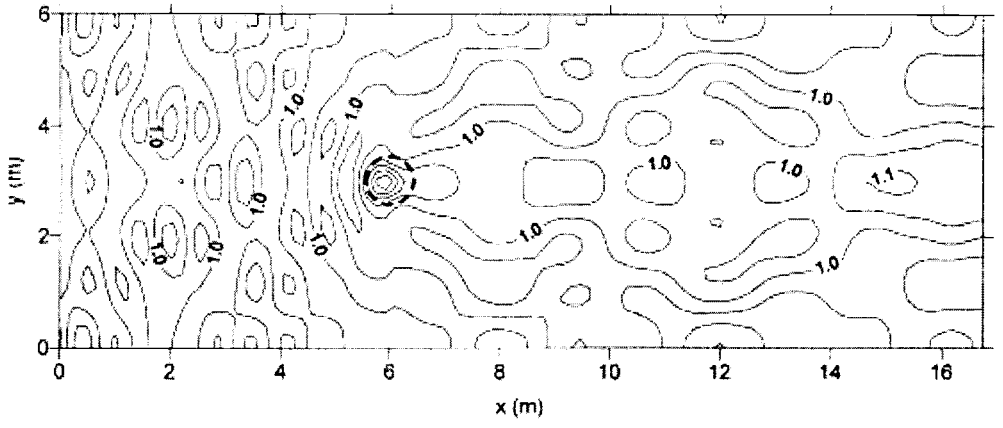

Figure 4.5: Relative amplitude contours calculated using MMSE model. $T = 1.259$ s (from Suh et al. 2001)

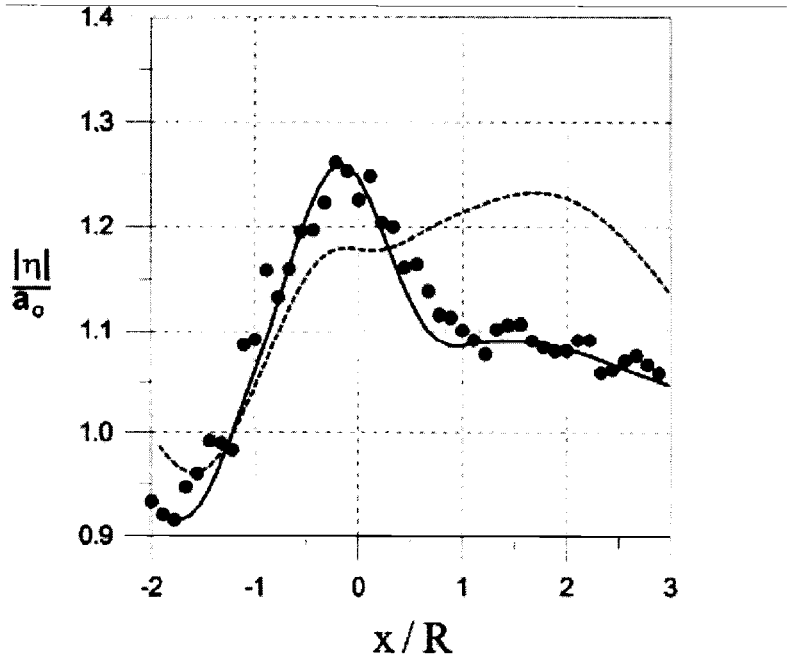

Figure 4.6: Relative amplitude variation along longshore transect through centerline of shoal with radius R. $T = 1.259$ s, ● = experimental data, __ = MMSE, ... = MSE (from Suh et al. 2001)

5.0 Two-dimensional analysis

Applications in this section investigate the impacts on the wave field in the presence of a pit with finite longshore dimensions. First the importance of reflection on the wave field is evaluated. Most predominantly, how its effects transpire far leeward of the pit. Secondly, the discrepancies between the MSE and the MMSE models are investigated in a similar manner as § 3. As in the case with only one horizontal dimension, a hyperbolic form of the MMSE is employed. The addition of the longshore coordinate in the model formulation allows the study of bathymetric anomalies more closely resembling borrow pits. Moreover, the impacts of the wave field within a surf zone are additionally investigated.

5.1 Implementation of modified mild-slope equation model

The extension of the model to include two-horizontal dimensions is straightforward. The same governing equations in § 3.1 are used. However, now the vertically integrated volume flux given in equation (3.5) is given in two horizontal dimensions as $\boldsymbol{Q} = \{P,Q\}$. Additionally, to study the modified wave fields effect on the nearshore region a surf zone must be introduced. This is accomplished through the introduction of another energy dissipation term simulating wave breaking. This term is formulated following Watanabe and Dibajnia (1988), but is now modified for two horizontal dimensions. This breaking formula has been proven to perform consistently with experimental data. Since the form was intended to be implemented for Copeland's (1985) solution to the MSE, it is similarly chosen to be implemented in this study over other possible breaking models.

Due to the time dependency of the model, the free surface elevation may be evaluated contemporarily at each time step allowing the volume flux $\boldsymbol{Q}$ at the nearshore boundary to be set to zero; this eliminates the necessity for a nearshore sponge layer. However, the sponge layer at the offshore boundary is still maintained. Thus with the inclusion of the wave breaking term, equation (3.11) is modified to the following

$$\frac{\partial \mathbf{Q}}{\partial t} + CC_g \nabla \eta + \omega D_s \mathbf{Q} + f_D \mathbf{Q} = 0 \tag{5.1}$$

where f_D is the energy dissipation term given by Watanabe and Dibajnia (1988) as

$$f_D = \alpha_D \tan\beta \sqrt{\frac{g}{h}\left(\frac{\mathbf{Q} - Q_r}{Q_s - Q_r}\right)} \tag{5.2}$$

$$Q_r = 0.4(\eta / h)_b Ch \tag{5.3}$$

$$Q_s = \{0.4(0.57 + 5.3\tan\beta)\}Ch \tag{5.4}$$

where again $\boldsymbol{Q}$ is the flow rate amplitude given in equation (3.5), Q_r is the flow rate amplitude of the broken wave in depth h, Q_s is the wave induced flow rate inside the surf zone on a uniformly sloping beach of tanβ, $(\eta/h)_b$ is the ratio of wave amplitude to water depth at the breaking point; and α_D is a linear ramping function that varies in magnitude from 0 to 2.5 over a cross-shore distance of one-half the wavelength at breaking. This is performed to suppress numerical reflection that would occur if α_D is held constant.

5.1.1 Finite difference method implementation

The governing equations are then discretized in a two dimensional grid as in Figure 5.1 following the same procedure in § 3.1.1. The addition of the longshore coordinate results in the following equation for the free-surface

$$\frac{\eta_{i,l}^{n+1/2} - \eta_{i,l}^{n-1/2}}{\Delta t} + \frac{\dfrac{P_{i+1/2,l}^{n} - P_{i-1/2,l}^{n}}{\Delta x} + \dfrac{Q_{i,l+1/2}^{n} - Q_{i,l-1/2}^{n}}{\Delta y}}{\left[\dfrac{C_g}{C} - R_1\left(\dfrac{dh}{dx}\right)^2 - R_2\dfrac{d^2h}{dx^2}\right]_{i,l}} = 0 \tag{5.5}$$

and where equation (5.1) is spilt into a relation for the volume flux in both the cross-shore and longshore coordinate as

$$\frac{P_{i-1/2,l}^{n+1} - P_{i-1/2,l}^{n}}{\Delta t} + \left[CC_g\right]_{i-1/2,l} \frac{\eta_{i,l}^{n+1/2} - \eta_{i-1,l}^{n+1/2}}{\Delta x} + \omega\left[D_s\right]_{i-1/2,l} P_{i-1/2,l}^{n} + \left[f_D\right]_{i-1/2,l} P_{i-1/2,l}^{n} = 0 \tag{5.6}$$

$$\frac{Q_{i,l-1/2}^{n+1} - Q_{i,l-1/2}^{n}}{\Delta t} + \left[CC_g\right]_{i,l-1/2} \frac{\eta_{i,l}^{n+1/2} - \eta_{i,l-1}^{n+1/2}}{\Delta y} + \omega\left[D_s\right]_{i,l-1/2} Q_{i,l-1/2}^{n} + \left[f_D\right]_{i,l-1/2} Q_{i,l-1/2}^{n} = 0 \tag{5.7}$$

where the grid size to wavelength ratio criterion still follows $\Delta x = \Delta y \geq \lambda_l/60$.

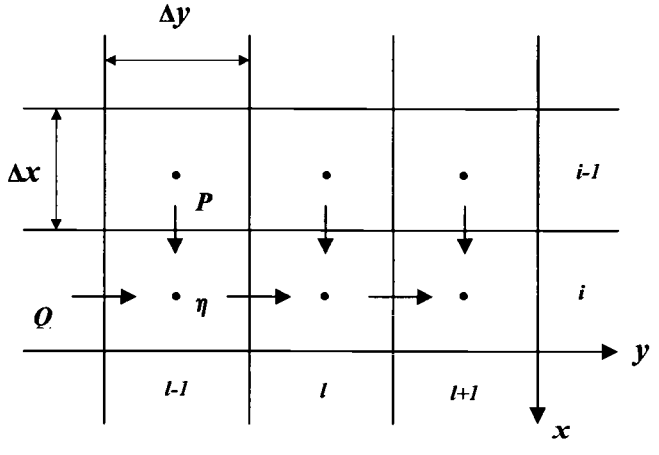

Figure 5.1: Finite difference grid following Suh et al. (2001)

As in § 3.1.1 the governing equations are implemented numerically using a standard finite differencing scheme. However, since two horizontal dimensions now exist the equations are slightly modified. In this formulation, waves are internally generated along a line. Again, a free surface elevation η^* is added to the free surface elevation of the incident wave η^I for each time step Δt following the relation in equation (3.10). Additionally, in order to achieve numeric stability the same criterion on the time step is chosen, which states $C_r = C\Delta t/\Delta x = 0.2$. Moreover, the inclusion of the longshore

coordinate modifies equations representing the bottom curvature and slope to the following

$$\left[\left(\frac{dh}{dx}\right)^2\right]_{i,l} = \left(\frac{h_{i+j,l} - h_{i-j,l}}{2j \cdot \Delta x}\right)^2 + \left(\frac{h_{i,l+j} - h_{i,l+j}}{2j \cdot \Delta y}\right)^2 \tag{5.8}$$

$$\left[\frac{d^2h}{dx^2}\right]_{i,l} = \frac{h_{i+j,l} - 2h_{i,l} + h_{i-j,l}}{(j \cdot \Delta x)^2} + \frac{h_{i,l+j} - 2h_{i,l} + h_{i,l-j}}{(j \cdot \Delta y)^2} \tag{5.9}$$

where i and l are the cross-shore and longshore coordinates respectively, Δx and Δy are the grid sizes, and j is the minimum integer required to produce a positive denominator in equation (3.3). This integer by default is set at $j = 1$, however as shown in the two-dimensional analysis when sharp transitions in depth exist, a larger value is required.

5.1.2 Calculation of wave height and wave angle

In order to determine the effects of the modified wave climate on shoreline response the wave height and wave angle must be calculated to drive the shoreline response model. The wave height can be generated from the model by time-averaging the time series of free-surface elevation after steady-state conditions have been reached. The root-mean-square of the free-surface elevation time series is used to calculate wave height by the following relation

$$H_{rms} = 2(2 \cdot \overline{\eta^2})^{1/2} \tag{5.10}$$

where the bar designates a time-average. Depth-limited breaking is used in the present formulation to determine the point when breaking is initiated. This follows the criterion

$$\kappa = \frac{H}{h} \tag{5.11}$$

where κ = 0.78 is the breaker index defined by the USACE Coastal Engineering Manual (2001) for regular waves. The numerical model determines when $\kappa \geq 0.78$ and turns on the dissipation term f_D in equation (5.1) to simulate wave breaking.

Wave direction can be calculated by tracking the directions of the two volume flux vectors P and Q at each grid point. Since these values are vertically integrated from the particle velocity, wave direction can be closely approximated by

$$\theta = \arctan\left[(\overline{Q^2} / \overline{P^2})^{1/2}\right] \tag{5.12}$$

which follows the formula used by Copeland (1985).

5.2 The influence of longshore finiteness and pit geometry

The importance of the borrow site shape may significantly influence the wave field modification. As shown in the proceeding section, the sidewall shape and slope of a trench can influence the magnitude and location of the reflection coefficient in k_1h_1. In a similar fashion, the sidewall shape and slope in the longshore direction might impact the degree of refraction and diffraction generated in lee the borrow pit. Figures 5.3 to 5.5 illustrate the impact on the wave height H_{rms} as well as the wave direction θ for three different borrow pit geometries: (1) a tapered square pit, (2) a truncated cone, and (3) a Gaussian shaped pit. In these cases constant depth, mean cross-shore width $\bar{a}$, and longshore length $\bar{b}$ is fixed in order to exemplify the specific cases effects on refraction, diffraction, and reflection. The square pit and the truncated cone have sidewall slopes of 0.2:1. The relative pit length and width for each case are $\bar{a}/h_1 = \bar{b}/h_1 = 15$. The profile in depth for the Gaussian shaped pit is defined similarly to equation (3.16) but now includes a longshore dependency. The equation is modified accordingly as

$$h(x,y) = h_1 + (h_2 - h_1) \cdot e^{-\left[\frac{(x-x_c)^2}{2\cdot\beta_1^2} + \frac{(y-y_c)^2}{2\cdot\beta_2^2}\right]} \tag{5.13}$$

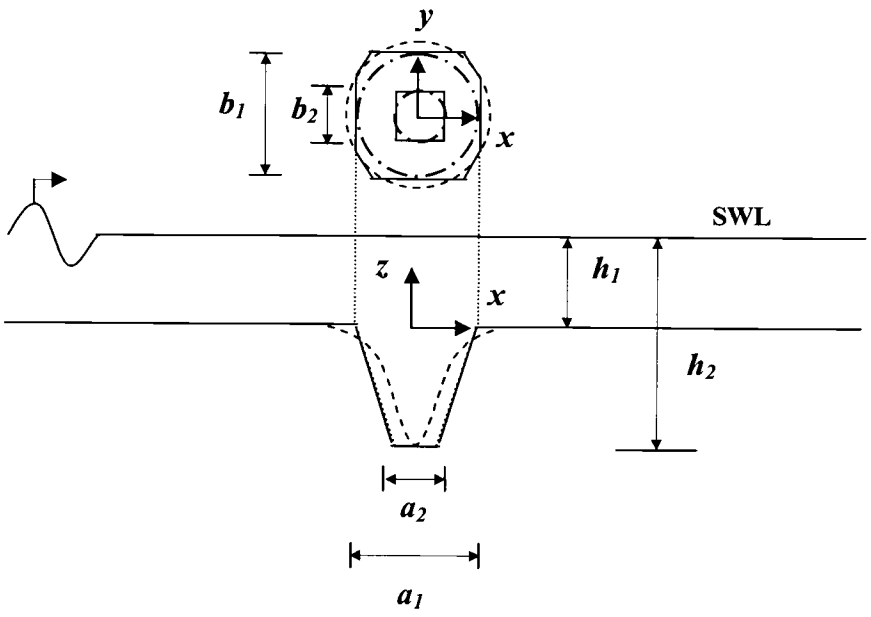

Figure 5.2: Definition sketch for three-dimensional pit. __ = tapered square, _.._ = truncated cone, --- = Gaussian

In order to be consistent with the analysis in § 3, the relative shape parameters $\beta_1 = \beta_2 = 12$ were selected. The volume inside each pit is comparable for each pit type; however, the cross-shore and longshore dimensions are somewhat larger than for the tapered square and truncated cone. It is evident from Figures 5.3 to 5.5 that no single pit type produces significantly different patterns in the wave field. This may imply that the sidewall slope rather than the shape of the pit itself has the biggest influence on the wave field for pits of similar length and width. The smallest attenuation occurs directly behind the pit and then the effects of diffraction cause energy to seep back into the region creating somewhat larger wave heights as the distance from the pit increases. For this example the incident wave height is H_i = 1m. For all cases the minimum wave height achieved is roughly $0.6H_i$; this can be seen more clearly in Figure 5.6. The cross-shore extent of the shadow region is slightly larger for the Gaussian shaped pit and tapered square pit than it is for the truncated cone. The $0.8H_i$ contour extends for approximately eight wavelengths leeward of the pit whereas for

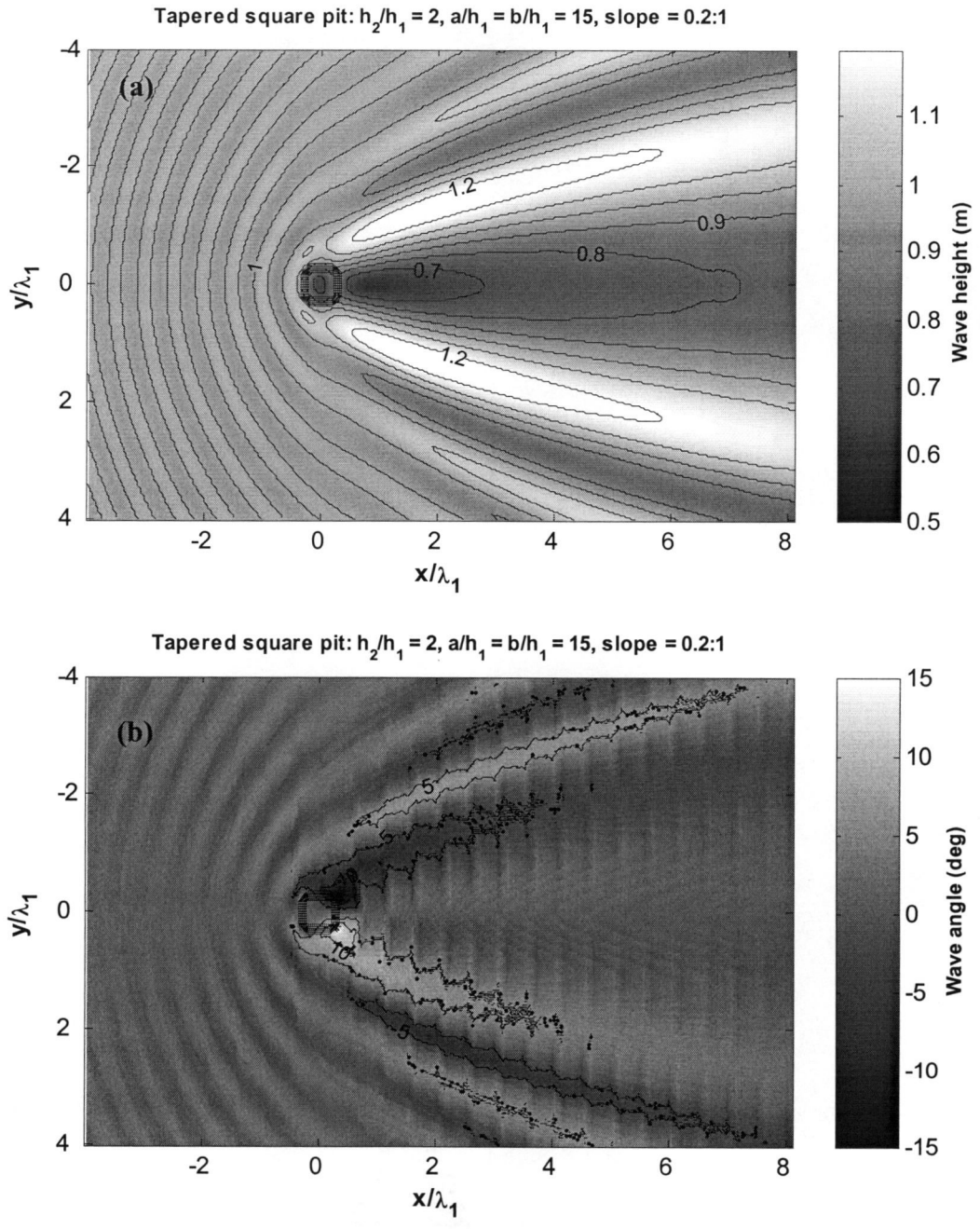

Figure 5.3: Contour plots for a tapered square pit with $k_1h_1 = 0.24$.
(a) wave height **(b)** wave direction; H_i = 1m, $\theta = 0°$, Δx = 1m

the truncated cone this contour extends only five wavelengths from the pit centerline. Additionally, the area of larger wave height associated with the scattering of wave energy extends further for the Gaussian shaped pit. This may be due to the fact that

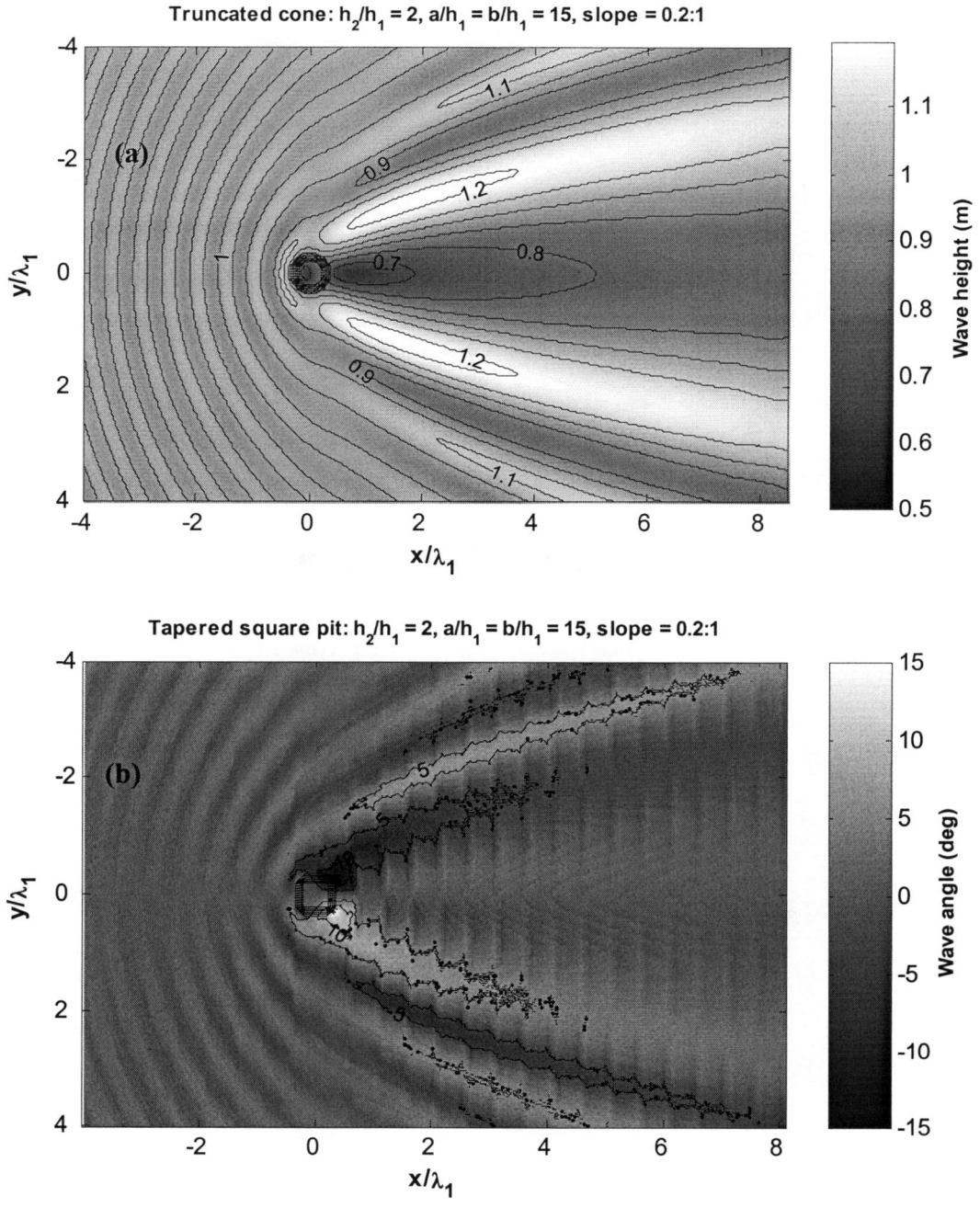

Figure 5.4: Contour plot for a truncated cone with $k_1h_1 = 0.24$
(a) wave height **(b)** wave direction; H_i = 1m, θ = 0°, Δx = 1m

the Gaussian pit has a larger planform area than any other pit types.

Figures 5.7 and 5.8 illustrate the longshore variation of wave height and direction at a cross-shore transect $x/\lambda_1 = +4$ leeward of the pit for each pit type. For normally incident waves the wave height is symmetric about the pit centerline, while

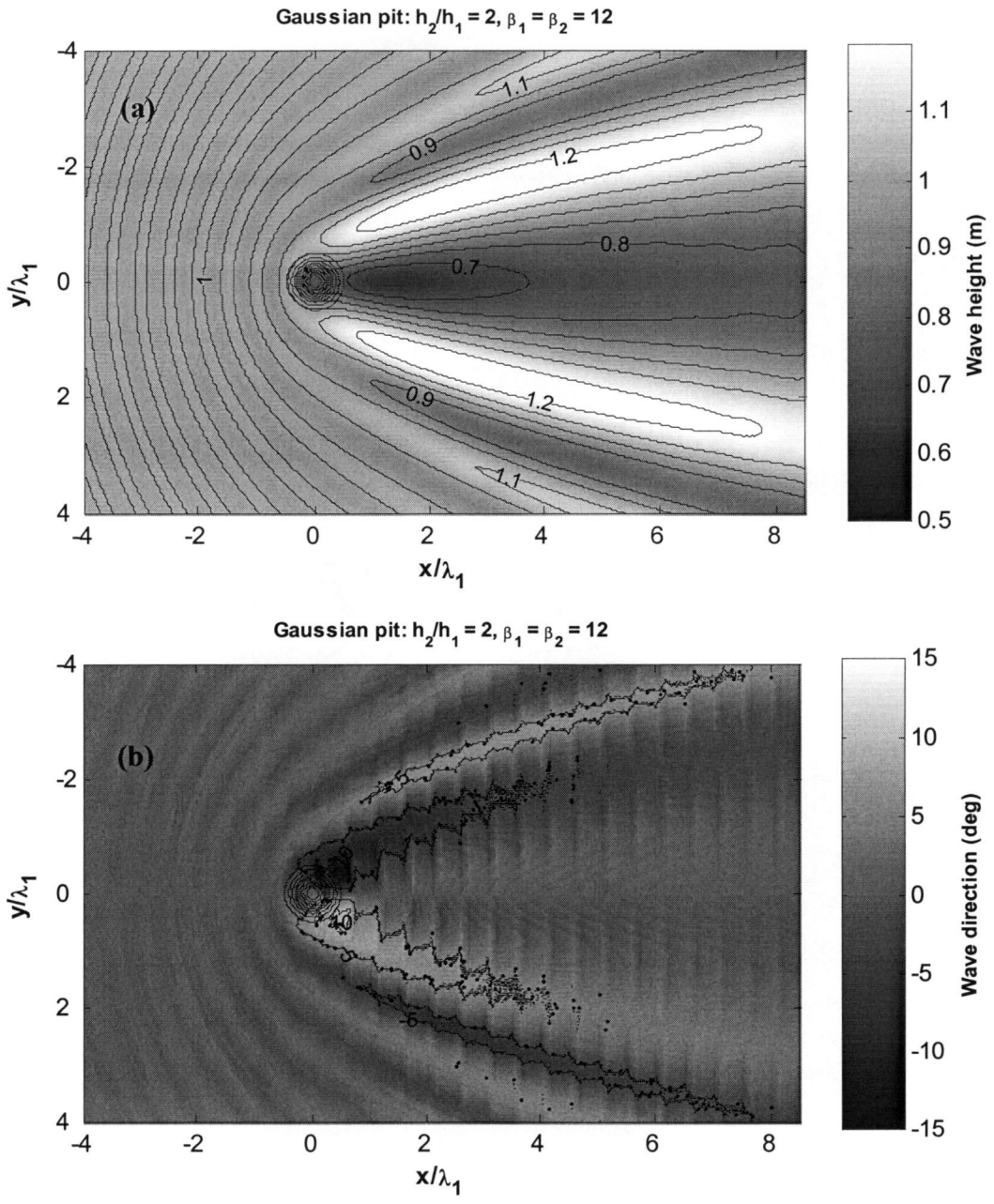

Figure 5.5: Contour plot for a Gaussian pit with $k_1h_1 = 0.24$
(a) wave height **(b)** wave direction; H_i = 1m, θ = 0°, Δx = 1m

the wave direction has an anti-symmetric relation. The most substantial difference between the pit types is the magnitude of reflection generated seaward of the anomaly. The reflection generated by the Gaussian shaped pit is much smaller than the other pit

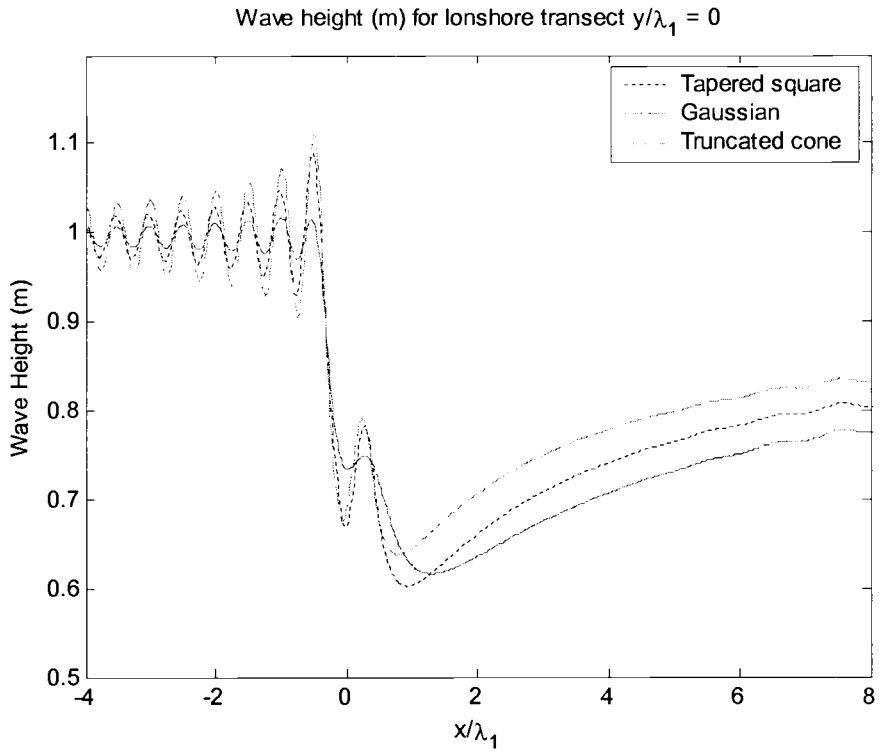

Figure 5.6: Cross-shore transect of wave height through pit centerline. $k_1h_1 = 0.24$, $\bar{a}/h_1 = \bar{b}/h_1 = 15$, $h_2/h_1 = 2$

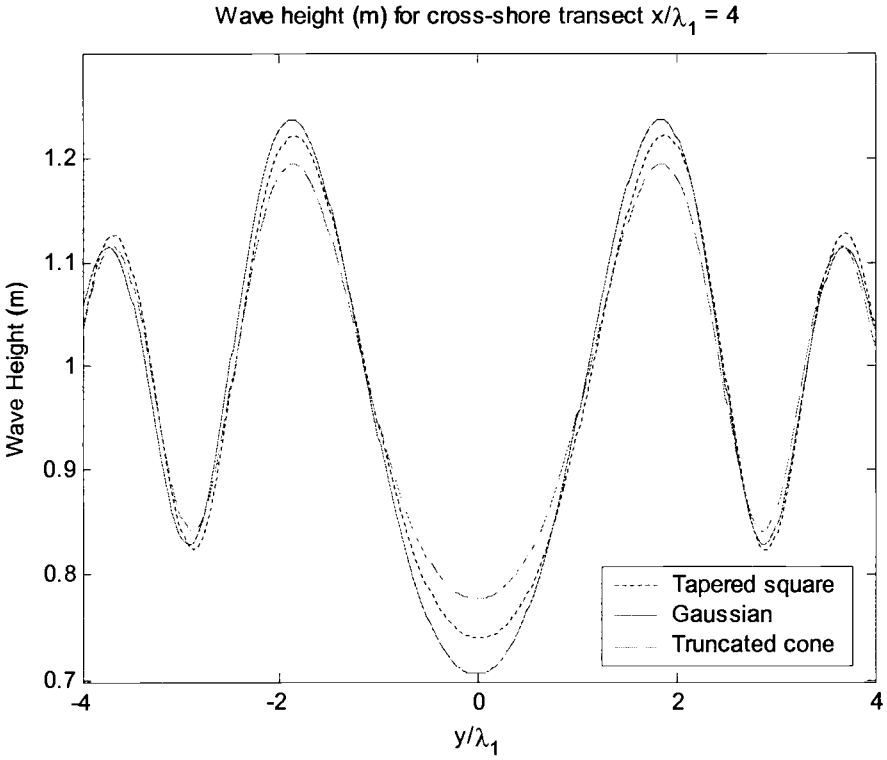

Figure 5.7: Longshore transect of wave height through $x/\lambda_1 = 4$. $k_1h_1 = 0.24$, $\bar{a}/h_1 = \bar{b}/h_1 = 15$, $h_2/h_1 = 2$

types. In the previous section, a Gaussian pit was shown to have only one distinct peak in the reflection coefficient K_r at $k_1h_1 \approx 0.1$ (see Figure 3.18). At $k_1h_1 = 0.24$ the reflection coefficient is approximately $K_r = 0.05$. This may contribute to why the longshore variation in wave height for the Gaussian pit is more extreme than for the other pit types which produce more reflection. In addition, the test illustrates that the overall trend in the longshore variation in wave height is dominated by refraction, and remains consistent for pit shapes of similar planform dimension.

Another effect of the pit geometry on the wave field (which is not directly shown here) is the influence of the longshore pit length $\bar{b}$. McDougal et al. (1996) demonstrates that the wave heights in the shadow region decrease in magnitude as the longshore length increases. This occurs because diffraction is a less dominant process directly behind the pit as the pit becomes longer; the example is analogous to a detached breakwater.

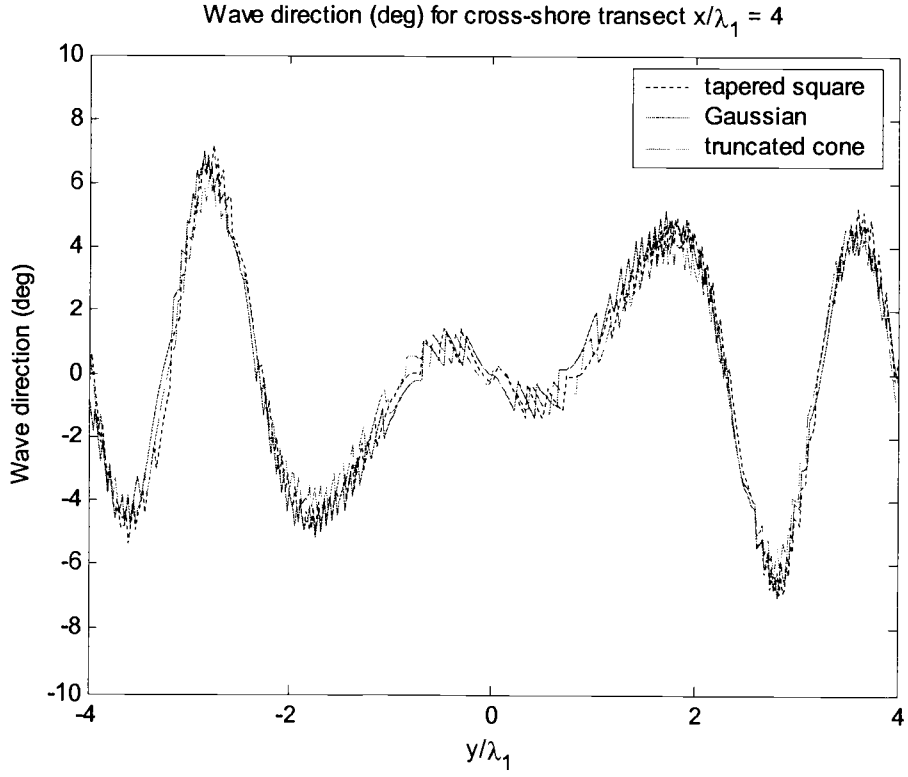

Figure 5.8: Longshore transect of wave angle through $x/\lambda_1 = 4$.
$k_1h_1 = 0.24$, $\bar{a}/h_1 = \bar{b}/h_1 = 15$, $h_2/h_1 = 2$

5.3 A test of the mild-slope equations inaccuracy in three dimensions

In § 3.2 and § 3.4 the inaccuracy of the MSE was shown for the case of a single slope following Booij's (1983) problem and again for a trench with linearly sloping sidewalls following Bender (2003). However, this was for longshore uniform transitions in depth, therefore it is of interest to determine how the inaccuracy of the MSE translates for the case of a finite pit and investigate if the refraction and diffraction patterns in lee of the pit are significantly altered using the MSE formulated model. Referring back to the results in Figure 3.15 for a trench with sidewall slopes of 1:1, large differences between the predicted magnitudes of K_r where shown when using the MSE versus the MMSE model. Specifically, for $k_1h_1 = 0.88$, where the MSE predicts $K_r = 0.0335$ and the MMSE predicts $K_r = 0.1860$. Figure 5.9 illustrates the wave height contour plot for a square pit with the same dimensions used in the one-dimensional trench case using the MMSE model.

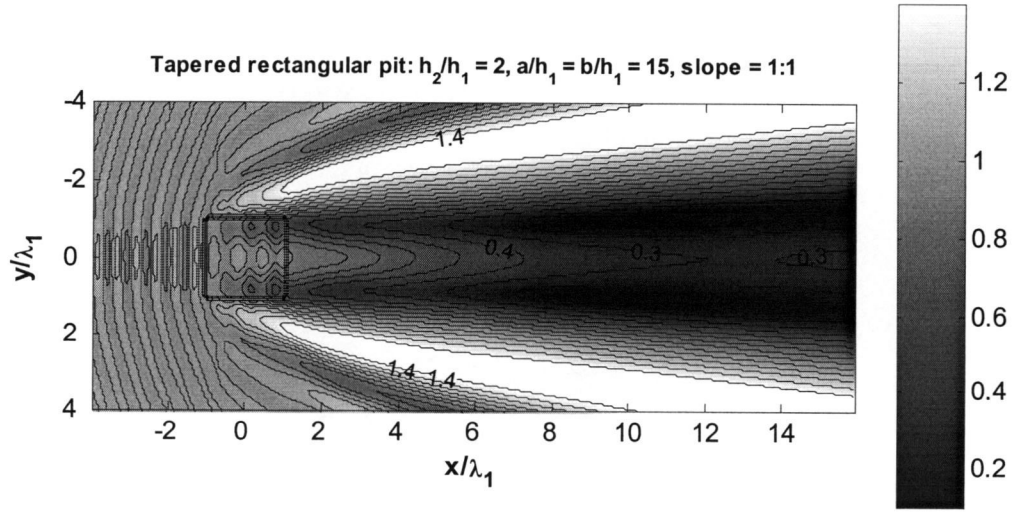

Figure 5.9: Contour plot of wave height using MMSE model (to scale)
$k_1h_1 = 0.88$; $\bar{a}/h_1 = \bar{b}/h_1 = 15$, $h_2/h_1 = 2$; sidewall slope = 1:1

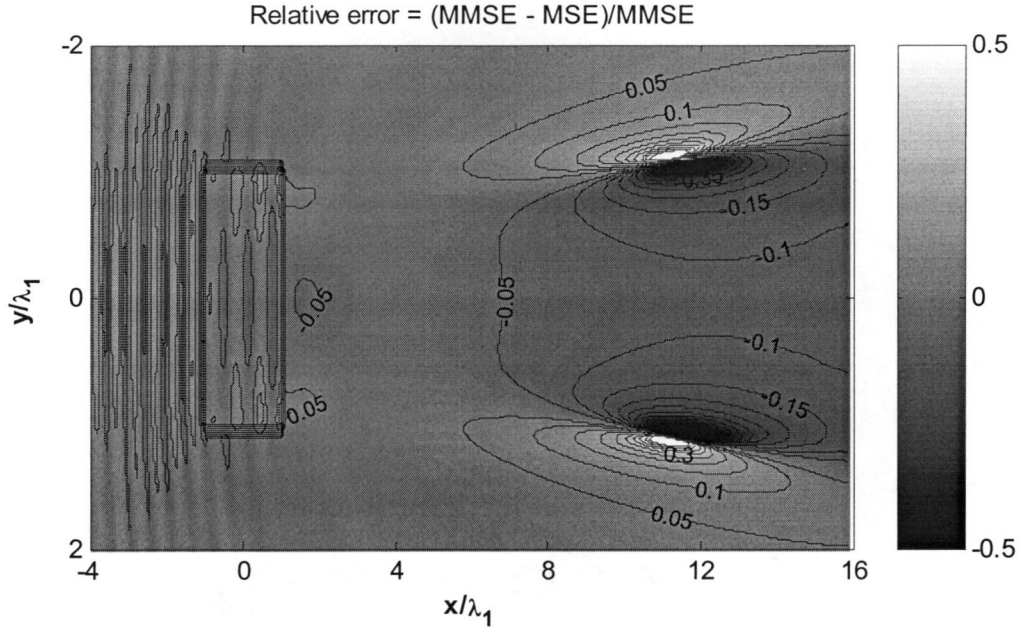

Figure 5.10: Relative error between the MMSE and MSE models (distorted scale). $k_1h_1 = 0.88$; $\bar{a}/h_1 = \bar{b}/h_1 = 15$, $h_2/h_1 = 2$; sidewall slope = 1:1

Using the same relative trench depth, width, and incident wave conditions, the inaccuracy of the MSE is tested. Figure 5.10 demonstrates the relative error between the MSE and MMSE models. In order to magnify the region where error occurs, the cross-shore and longshore scales are distorted. The relative error is calculated using the relation

$$\frac{H_{MMSE} - H_{MSE}}{H_{MMSE}} \tag{5.14}$$

The difference between the two models is apparent in two regions: (1) seaward of the pit and (2) leeward of the pit near the longshore transects $y/\lambda_1 = \pm 1$. The first discrepancy is expected since the magnitudes in K_r were shown to be considerably different for the infinitely long trench. The second region where the two models disagree occurs in the shadow regions leeward of the trench. This pit is located within the intermediate depth region and correspondingly alters the refraction pattern leeward of the pit. Here, two shadow regions adjacent to the pit corners develop rather than

one region located through the centerline of the pit as in § 5.2. However, a point to be made is the absolute difference in wave height is not large; this can be seen looking at the longshore variation in wave height through a longshore transect at $x/\lambda_f = 12$ in Figure 5.11. As in the case for an infinitely long trench with sloping sidewalls, the MSE predicts larger wave heights leeward of the pit. Figure 5.12 shows the wave height over a cross-shore transect through the pit centerline at $y/\lambda_f = 0$ and also demonstrates this effect. Thus, the prediction by the MSE to does not seem to alter the wave height leeward of the pit by an extensive amount; the maximum difference in wave height is roughly 3 cm in magnitude. The reason the difference is minimal may be influenced by the presence of diffraction since the pit is finite in longshore extent.

In order to test the dominance of diffraction and the possibility that wave energy is being leaked back into the region directly leeward of the pit, the longshore extent of the pit is increased by four times (i.e. $\bar{b}/h_1 = 60$). The contour plot of wave height using the MMSE model is given in Figure 5.13. The increased pit length (in theory) will lessen the effects of diffraction in the shadow region since a larger distance separating the pit corners exists. Figure 5.14 shows the relative error between the MSE and MMSE results. As in the square pit case, the largest relative error between the two models occurs seaward of the pit and adjacent to the pit corners; this which also corresponds to the shadow regions as shown in Figure 5.15. The wave height in this region is approximately $H = 0.2$ m. In the cross-shore transect through the pit centerline, the largest difference in absolute wave height occurs. The MMSE predicts a wave height of approximately 5 cm smaller than the MSE. For this case the wave height increases in after eight wavelengths leeward of the pit, which is illustrated in Figure 5.16. Although increasing the length of the pit does produce a slightly larger error between the MMSE and MSE models, no significant difference in the trend in longshore wave height occurs. Rather, this test more clearly demonstrates the importance of the pit length, and how the shadow region moves to different longshore positions as the length of the pit changes.

Since the effects of wave reflection are not significant for this case, it may be useful to impose a criterion that specifies when reflection will start to contribute to

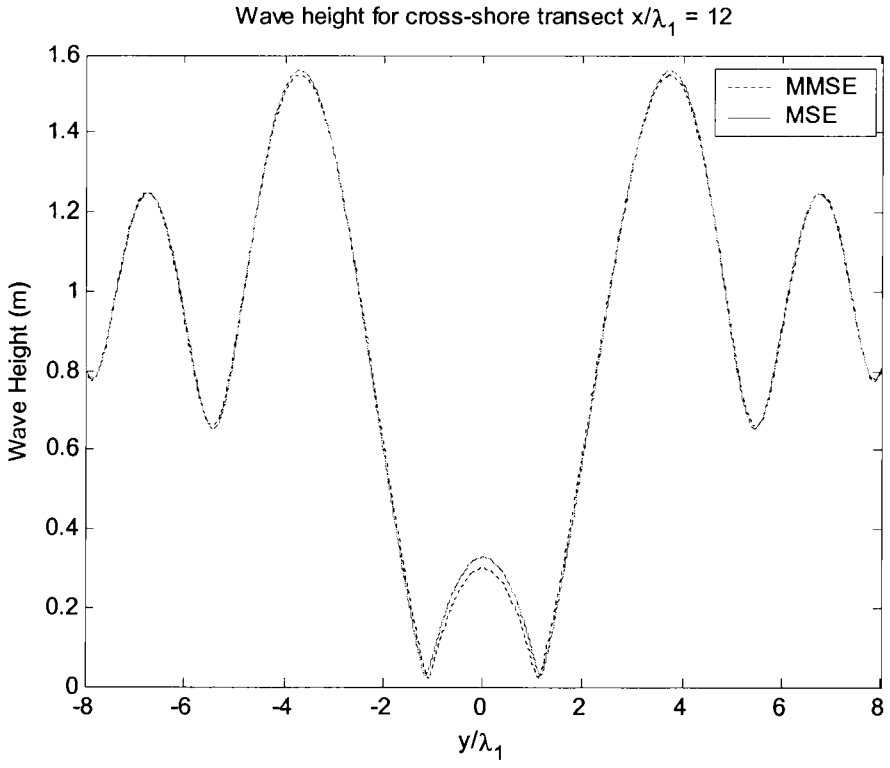

Figure 5.11: Comparison of wave height along longshore transect $x/\lambda_1 = 12$

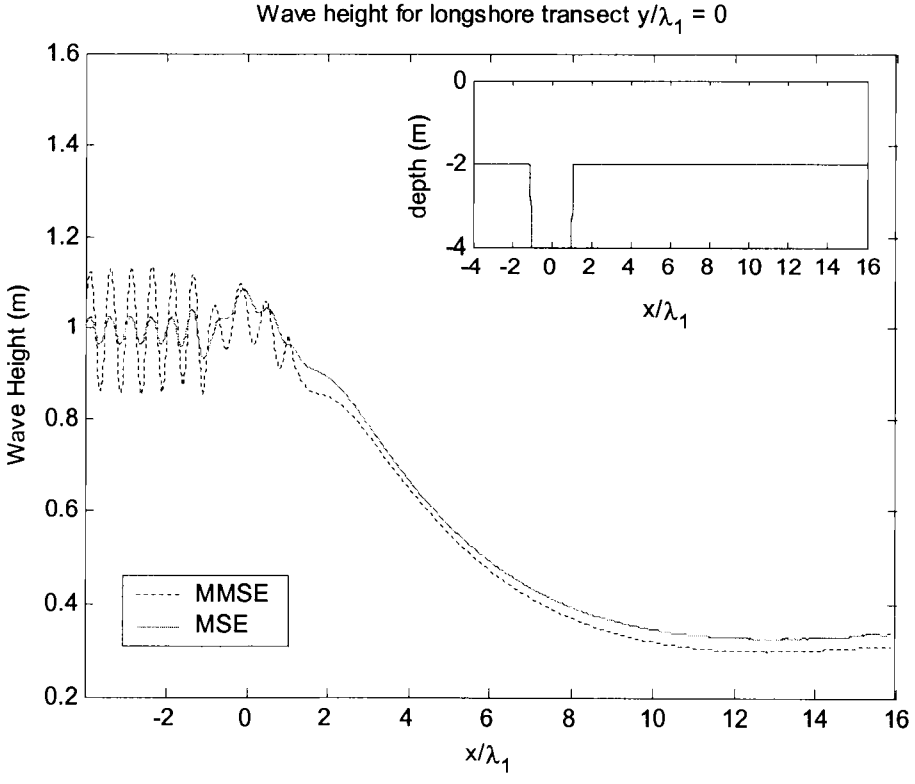

Figure 5.12: Comparison of wave height along transect through pit centerline $y/\lambda_1 = 0$

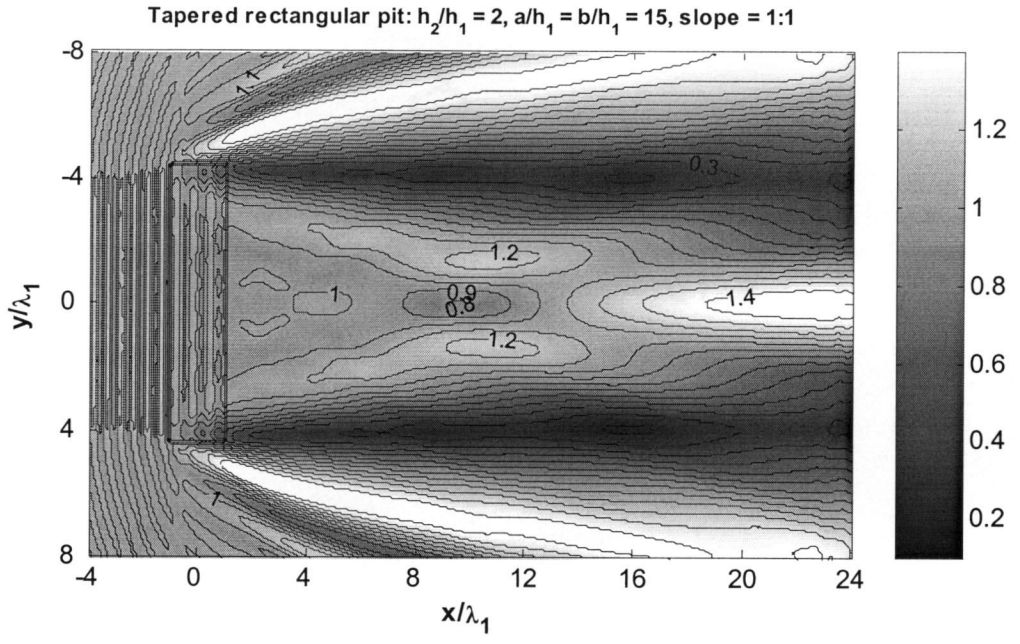

Figure 5.13: Contour plot of wave height using MMSE model (to scale)
$k_1h_1 = 0.88$; $\bar{a}/h_1 = 15$, $\bar{b}/h_1 = 60$, $h_2/h_1 = 2$; sidewall slope = 1:1

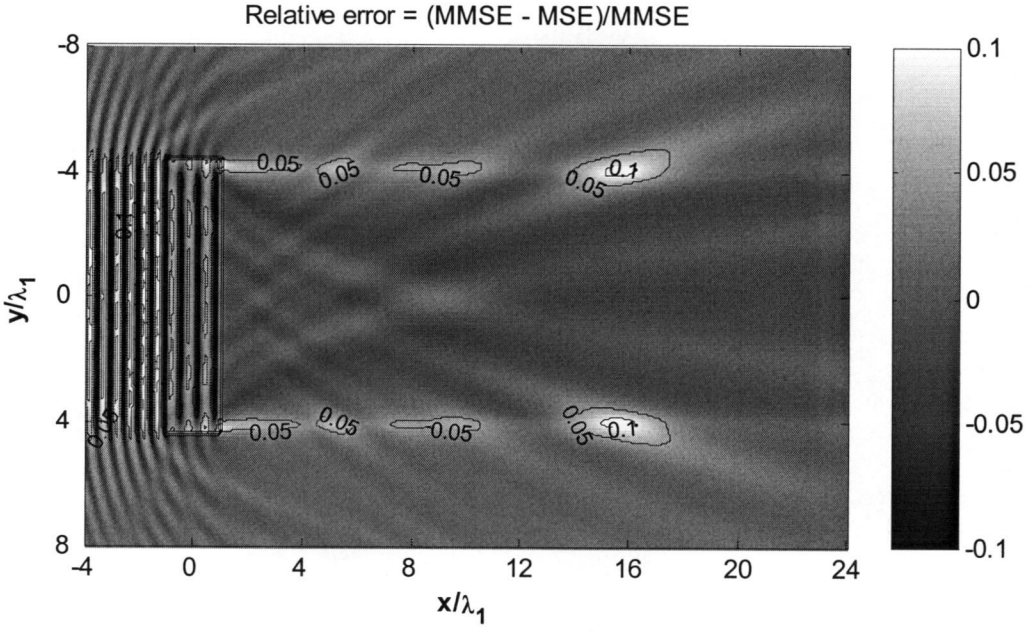

Figure 5.14: Relative error between the MMSE and MSE models.
$k_1h_1 = 0.88$; $\bar{a}/h_1 = 15$, $\bar{b}/h_1 = 60$, $h_2/h_1 = 2$; sidewall slope = 1:1

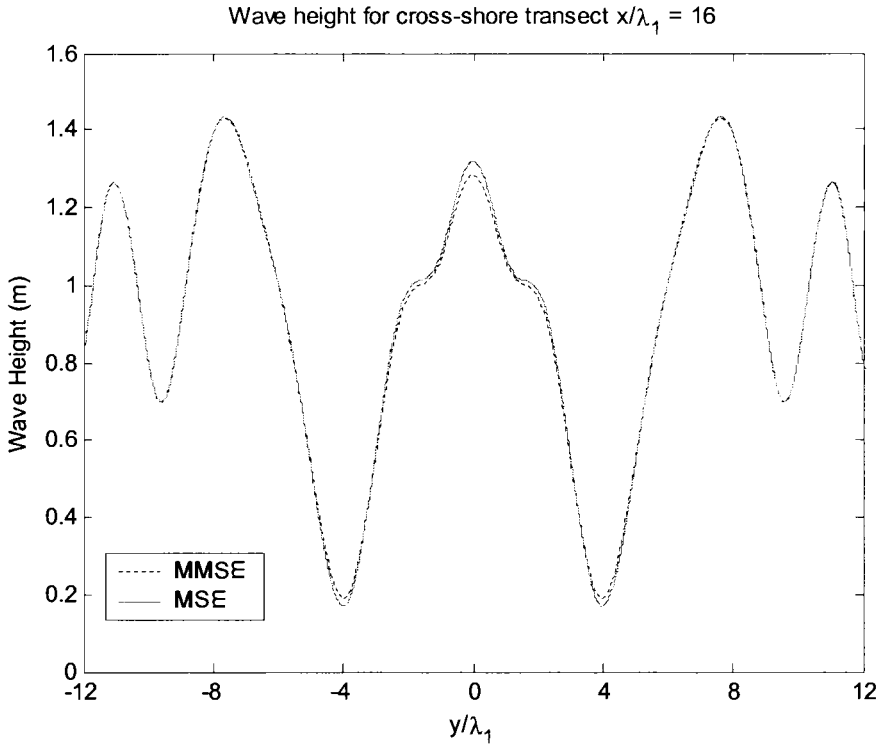

Figure 5.15: Comparison of wave height along longshore transect $x/\lambda_1 = 16$

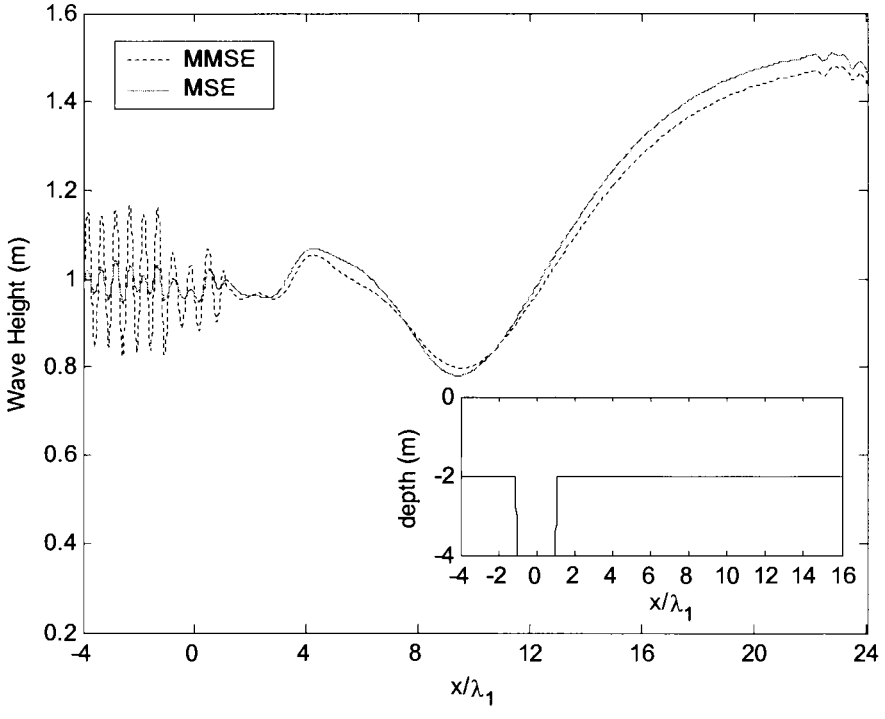

Figure 5.16: Comparison of wave height along transect through pit centerline $y/\lambda_1 = 0$

significant changes leeward of the pit. The magnitude of the transmitted wave is related to the reflected wave by

$$K_r^2 + K_t^2 = 1 \tag{5.15}$$

assuming energy is conserved. Therefore, for a 10% reduction of the transmitted wave (Kt = 0.9) would require $K_r = 0.44$, and similarly for 20% reduction in wave height $K_r = 0.6$. This means that much larger reflection coefficients are necessary before reflection may start contribute significantly to the wave field leeward of the pit. In the current study, the reflection coefficient never reached a value larger than $K_r = 0.4$.

5.4 Addition of a surf zone: Investigation of breaking conditions

The previous examples focus only on the accuracy of the wave model using a constant depth surrounding the pit. In this section a borrow site located just outside a surf zone is investigated. A planar beach is initiated at a cross-shore distance leeward of the pit rather than being applied to the entire cross-shore domain. Although, logistically a borrow site located within the beach slope can be modeled, such a bathymetry would have varying water depth on either side of the pit, altering the reflective properties of the pit. The same wave conditions used throughout the section are applied again. Here $k_1h_1 = 0.88$, where the water depth outside the pit is $h_1 = 10$m. Additionally, the depth inside the pit is $h_2 = 20$ m. The nearshore slope of $\tan\beta = 0.02$ is initiated at the cross-shore transect located 500 m offshore. Figure 5.17 provides the definition sketch of the setup for the model run. The modified wave field for this example is shown in Figure 5.18. The impact on the breaking location can clearly be seen.

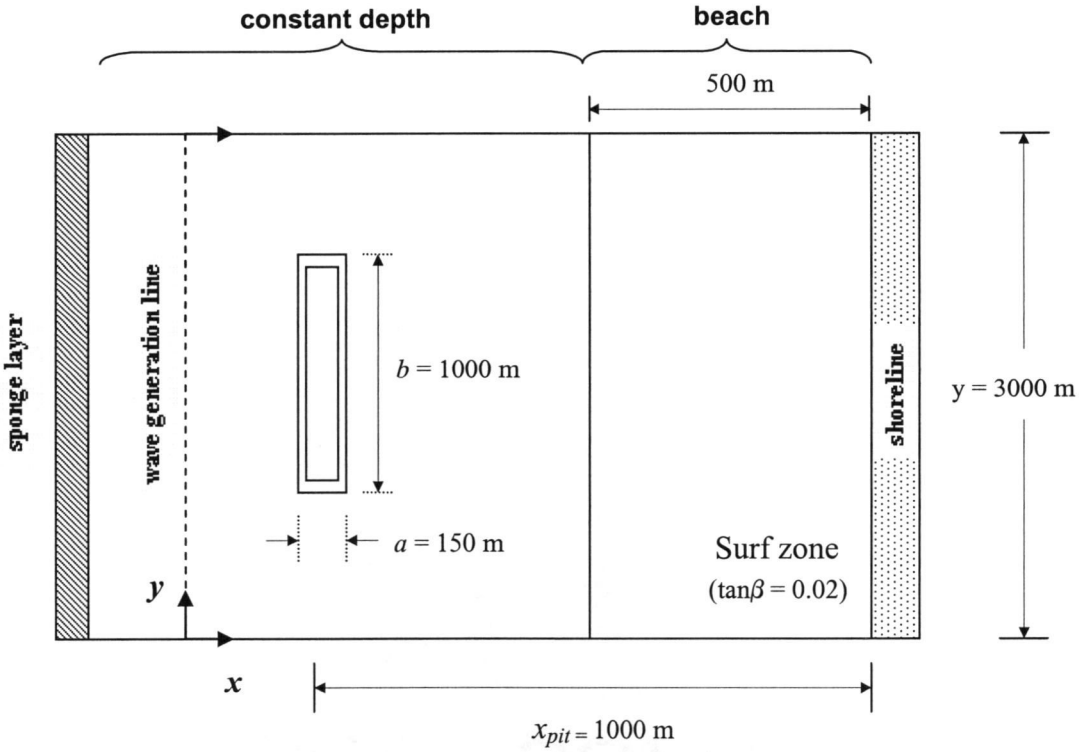

Figure 5.17: Definition of model domain with addition of surf zone

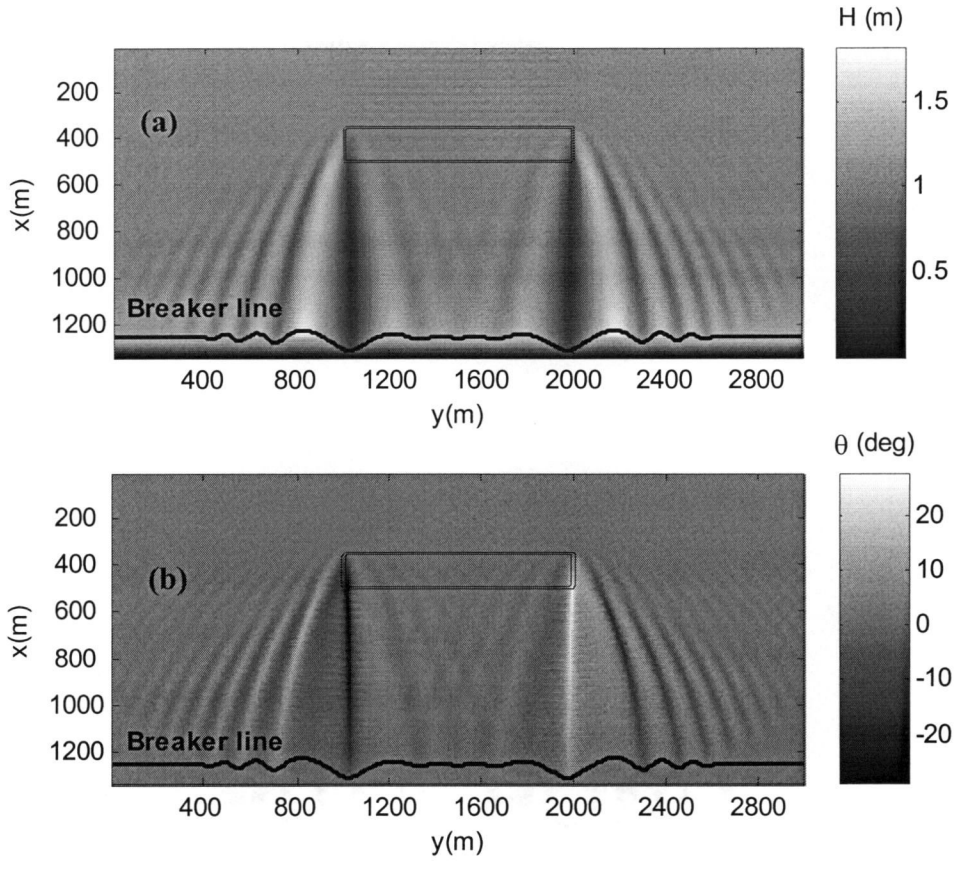

Figure 5.18: Modifications to **(a)** wave height and **(b)** wave angle. Tapered rectangular pit. $k_1h_1 = 0.88$; $\bar{a}/h_1 = \bar{b}/h_1 = 100$, $h_2/h_1 = 2$; sidewall slope = 1:1

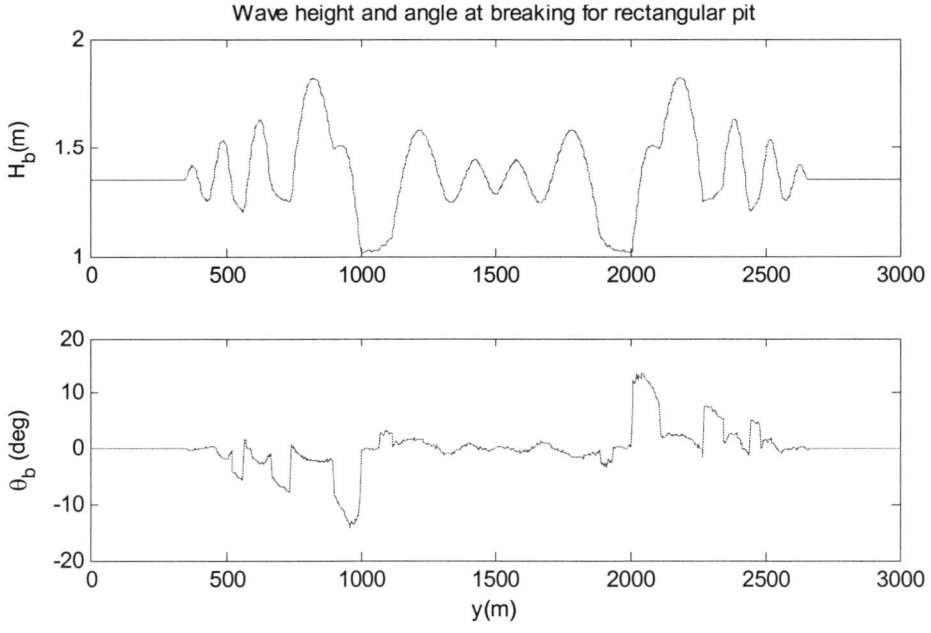

Figure 5.19: Wave height and angle at breaking for tapered rectangular pit

As the waves reach the nearshore region the influence from the borrow pit is still substantial; therefore the waves will shoal and ultimately break according to the wave pattern that occurs in the constant depth region. The cross-shore location at which breaking is initiated is a function of where the shadow region occurs. For this example, two shadow regions are generated adjacent to each pit corner. Figure 5.19 depicts how the largest wave angle occurs at the longshore positions where the shadow regions occur. Qualitatively this is explained by the scattering of waves from the regions through the effects of refraction.

5.5 Comparison of MMSE to REF/DIF 1

In Michalsen et al. (2003) the MMSE model is compared to the REF/DIF 1 wave model of Kirby and Dalrymple (1994). Figure 5.20 shows the resultant wave field leeward of a borrow pit with a truncated cone shape and 0.1:1 sidewall slopes. Since the pit is short in longshore extent, only one shadow region develops. However, the disruption on the breaker line is similar to the previous example. Figure 5.21 shows the prediction in the breaker line agrees very well between the two models. This provides more evidence that the wave field is controlled mainly by the effects of refraction and diffraction as the distance away from the borrow pit increases and the effects of reflection are not as significant. As a final investigation, the wave height and angle at breaking are compared over all longshore coordinates in Figures 5.22 (a) and (b). REF/DIF predicts significantly larger values of both, the reasons for these differences are unknown. However, the oscillations are well represented (i.e. the maxima and minima occur at the same longshore positions). Lastly the variation in wave height over the cross-shore transect through the pit centerline is given in Figure 5.22 (c). Here the only noticeable difference between the two models occur seaward of the trench. This is a result of REF/DIF's inability to include backscattered waves.

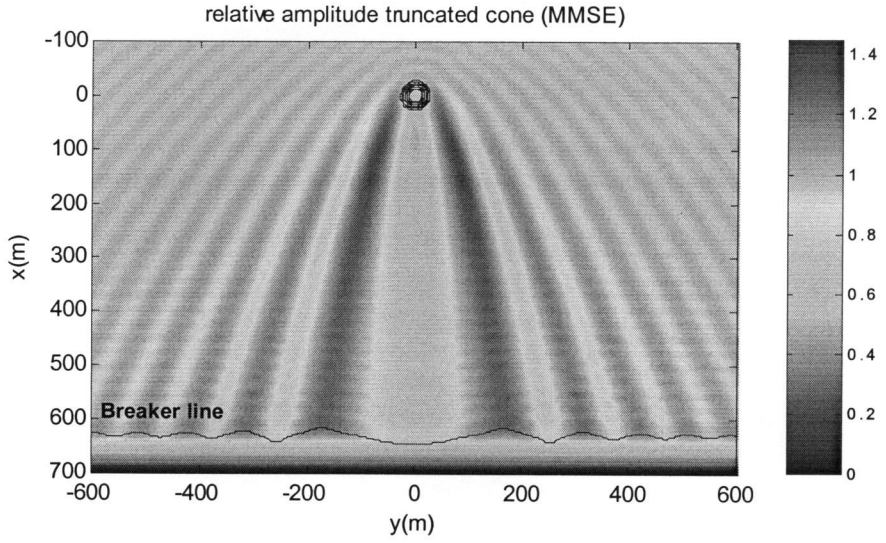

Figure 5.20: Wave height for truncated cone: $k_1h_1 = 0.24$, $\bar{a}/h_1 = \bar{b}/h_1 = 20$, $h_2/h_1 = 2$; sidewall slope = 0.1:1, H_i =1m, tanβ = 0.02

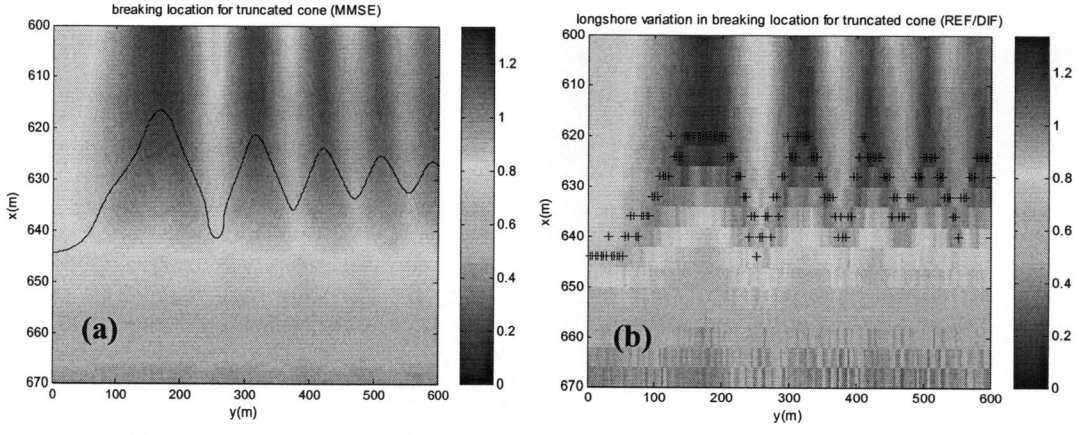

Figure 5.21: Wave height and location of breaking predicted using: **(a)** __ = MMSE model and **(b)** + = REF/DIF

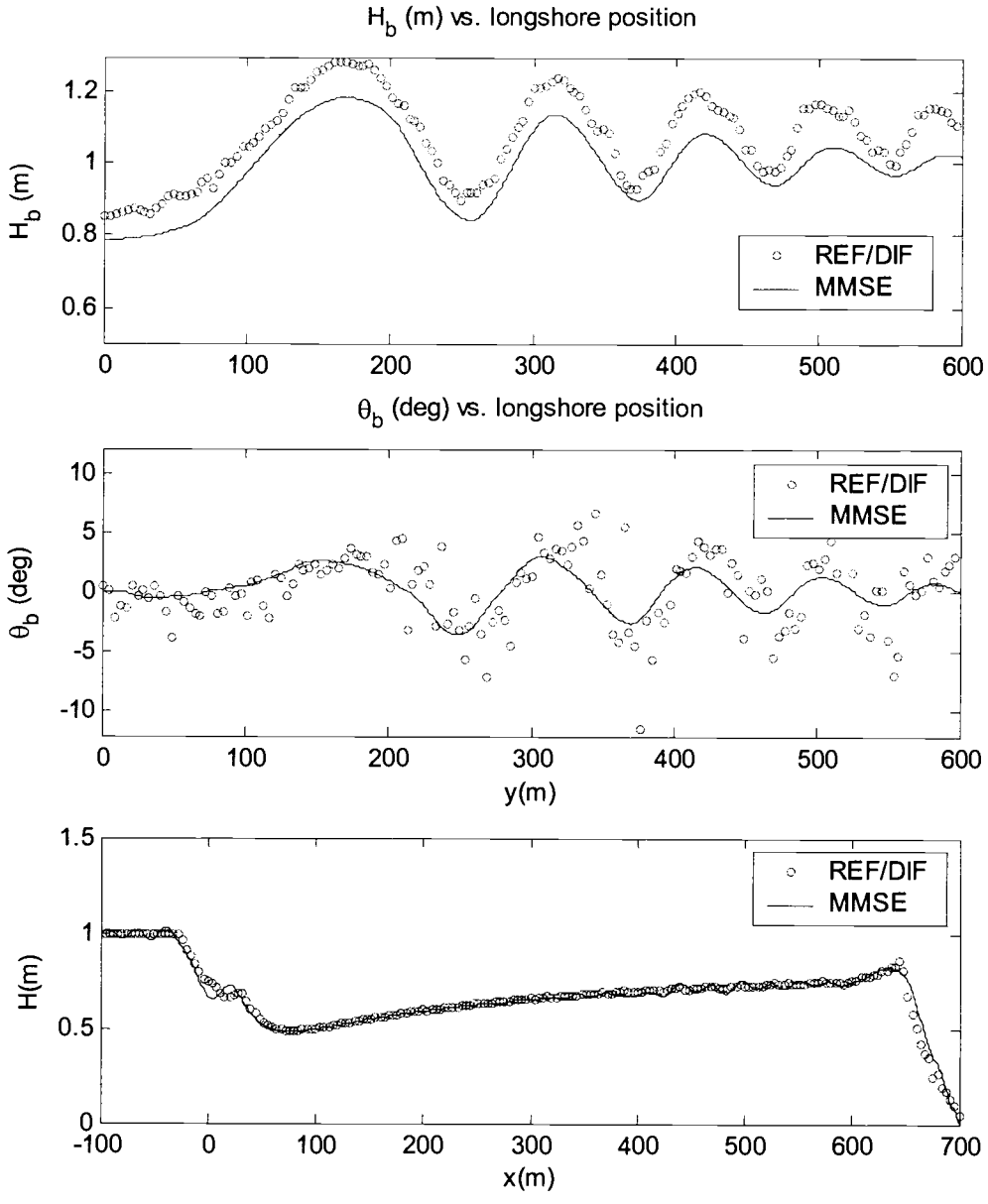

Figure 5.22: Comparisons between REF/DIF and MMSE for a truncated cone. **(a)** Wave height at breaking **(b)** wave angle at breaking **(c)** wave height along cross-shore transect through pit centerline (y = 0m)

6.0 Shoreline Response and nearshore circulation

The modified wave field created by the borrow pit can have direct impacts on the shoreline morphology (i.e. Grand Isle, LA). Borrow sites located within the active profile have been shown to influence the generation of erosional hot spots (EHS). Many studies have previously used one-line models by coupling a wave model that uses a parabolic approximation to the MSE. Therefore it is of interest to investigate the impacts of using such a model on the prediction of shoreline response around borrow sites where gradients in depth break the mild-slope criterion and where reflection is significant.

6.1 Shoreline response modeling

6.1.1 One-line model formulation

Many slightly different forms of one-line models exist, and there is generally a high degree of empiricism in formulations of longshore sediment transport. The sediment transport equation in the present study is formulated in the same manner employed in the GENESIS model by Hanson and Kraus (1989). The one-line model assumes a constant beach profile in the longshore direction. The "one-line" refers to the zero depth contour specifying the shoreline, and the depth of closure h_* specifies the cross-shore extent of the profile. The model moves the profile landward for accretion or seaward for erosion for each longshore cell. The governing equation controlling the shoreline position x in time t is based on the diffusion equation. The equation follows the form

$$\frac{\partial x}{\partial t} = \frac{1}{h_* + B} \cdot \frac{\partial Q_{sed}}{\partial y} \tag{6.1}$$

$$Q_{sed} = \frac{K_1 H_b^{2.5} \sqrt{g/\kappa} \sin 2\alpha_b}{16(s-1)(1-p)} - \frac{K_2 H_b^2 \sqrt{g/\kappa} \cos \alpha_b}{8(s-1)(p-1)\tan \beta} \cdot \frac{\partial H_b}{\partial y} \tag{6.2}$$

where a positive change in x indicates erosion, B is the berm height, Q_{sed} is the longshore transport rate, K_1 and K_2 are empirical coefficients, H_b is the wave height at breaking; κ is the breaker index; α_b is the wave angle at breaking relative to the shoreline ($\alpha_b = \theta_b - \gamma$), θ_b indicating the wave direction from the x-axis, and γ indicating the angle of shore normal from the y-axis; s is specific gravity of sand, p is the sand porosity, and $\tan\beta$ is the nearshore slope. The second term in equation (6.2) has been studied by Gourlay (1982) and is included when longshore gradients in wave height are large, as in the case of the present study. It is seen that the wave height and angle at breaking are the only items required to determine the shoreline evolution as a function of time. For the current study, the steady-state time-averaged wave height H_b and angle θ_b at breaking from the MMSE model are used to drive the model. The empirical coefficients K_1 and K_2 are specified by Kraus (1983) to be site specific. Although in previous literature, they have generally followed the value of $K_1 = 0.77$ and $0.5K_1 \leq K_2 \leq 1.0K_1$.

6.1.2 Numerical implementation

The change in shoreline position Δx is calculated for each longshore transect spaced at an even interval Δy. For faster computational time, Δy may be specified coarser than the grid size used in the wave model. The grid is setup so that the sediment transport $(Q_{sed})_i$ is specified at the grid lines and the shoreline position x_i is specified at the grid midpoints. Dean and Dalrymple (2002) discuss the implementation of equations (6.1) and (6.2) using an explicit method. Using this method the updated shoreline position as a function of time follows the methodology

$$x_i^{n+1} = y_i^n - \frac{\Delta t}{\Delta y(h_* + B)} \cdot \left(Q_{i+1}^{n+1} - Q_i^{n+1}\right) \tag{6.3}$$

where subscripts i and n denote the spatial and temporal steps, and $Q = Q_{sed}$ for convenience. However, the use of the explicit method places a criterion on the step in time for numerical stability; the time step Δt must be set according to

$$\Delta t < \frac{\Delta y^2}{2G} \tag{6.4}$$

in which the longshore diffusivity G is

$$G = \frac{K_1 H_b^{2.5} \sqrt{g/\kappa}}{8(s-1)(1-p)(h_* + B)} \tag{6.5}$$

In the present study the shoreline is initially straight; therefore, the initial shoreline position at the first time step is set to zero. Additionally the conditions at each longshore boundary are such that $x(0) = x(l) = 0$ where l designates the length of the beach

6.1.3 The significance of reflection

Although the resulting wave field leeward of a borrow pit is shown to be rather similar in comparison for both the MSE and MMSE models, it is still of interest to quantify the shoreline response predicted using a one-line model. The case in § 5.4 corresponds to a case when using the MSE is almost equivalent to neglecting wave reflection altogether. Therefore, this represents a case where the MMSE and MSE models should have the largest differences. As it turns out, the predicted shoreline response using the MMSE versus the MSE is visually indistinguishable. Figure 6.1 depicts the shoreline position that is calculated at four instances in time, t = 1, 5, 10, and 30 days using the empirical coefficients $K_1 = K_2 = 0.77$. By t = 30 days, the planform shape reaches an equilibrium where minimal change occurs. Two large areas of accretion develop near the y = 1000 m and y = 2000 m longshore coordinates. These locations correspond to the approximate locations of the pit corners as well as the place where the smallest breaking wave height occurs (e.g. Figure 5.17). The pattern of the shoreline position closely resembles the longshore variation in breaking wave height. This is due to the inclusion of the term proportional to the longshore gradient in wave height at breaking ($\partial H_b / \partial y$) originally imposed by Ozasa and

Brampton (1979) and used in the recent work of Bender (2003). On the other hand, Figure 6.2 illustrates the shoreline response predicted using the original CERC formula neglecting the term proportional to $\partial H_b / \partial y$. The result shows a general smoothing of the oscillations in erosion and accretion, however the largest areas of accretion still persist at the longshore positions y = 1000 m and y = 2000 m, but now extend about half as far from the initial shoreline position.

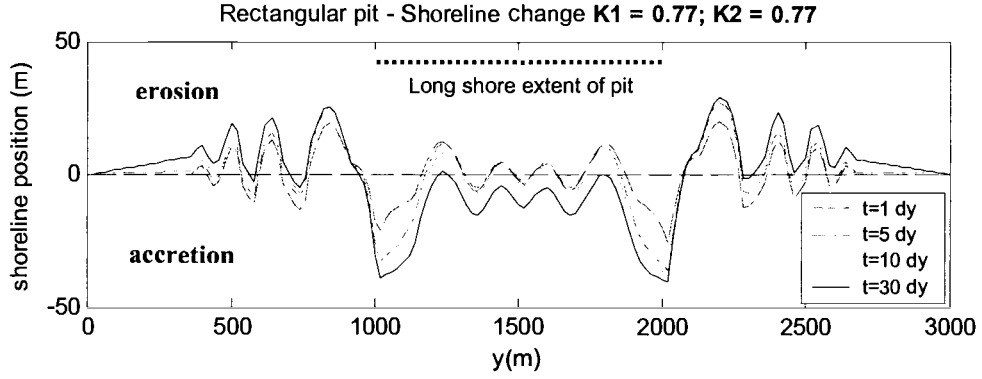

Figure 6.1: Shoreline evolution for tapered rectangular pit with $K_1 = K_2 = 0.77$. $k_1h_1 = 0.88$; $\bar{a}/h_1 = \bar{b}/h_1 = 100$, $h_2/h_1 = 2$; sidewall slope = 1:1, $x_{pit} = 1000$m, tanβ =0.02

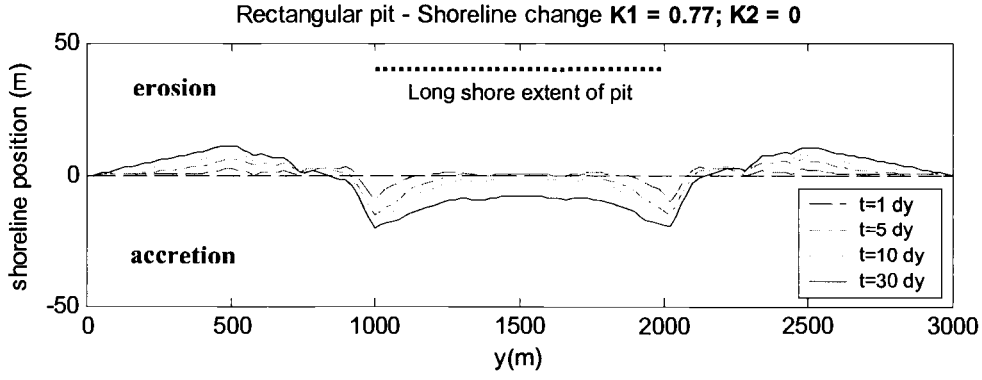

Figure 6.2: Shoreline evolution for tapered rectangular pit with $K_1 = 0.77$; $K_2 = 0$. $k_1h_1 = 0.88$; $\bar{a}/h_1 = \bar{b}/h_1 = 100$, $h_2/h_1 = 2$; sidewall slope = 1:1, $x_{pit} = 1000$m, tanβ =0.02

6.1.4 Comparison in shoreline response: REF/DIF 1 vs. MMSE

As a final test, the results using the MMSE model are compared to those using REF/DIF 1 (e.g. Kirby and Dalrymple 1994). In § 5.5, it was illustrated that REF/DIF predicts both a larger wave height and wave angle at breaking. The coefficients K_1 and K_2 are both fixed at 0.77 in order to apply an equal weighting to each sediment transport term in equation (6.2). Figure 6.3 shows that REF/DIF predicts a larger amount of accretion and erosion than the MMSE results predict. The model was run for twice as long for the MMSE case and the salient feature still did not extend even half as far. However, the differences are not attributed to the fact that REF/DIF is unable to include the effects of reflection. Instead it is believed that the noise included in the longshore variation in wave angle (e.g. Figure 5.20 (b)) is the main source of the two models differences. For this reason, in addition to the fact that REF/DIF does not include reflection makes it is difficult to trust the accuracy of its results in a one-line model.

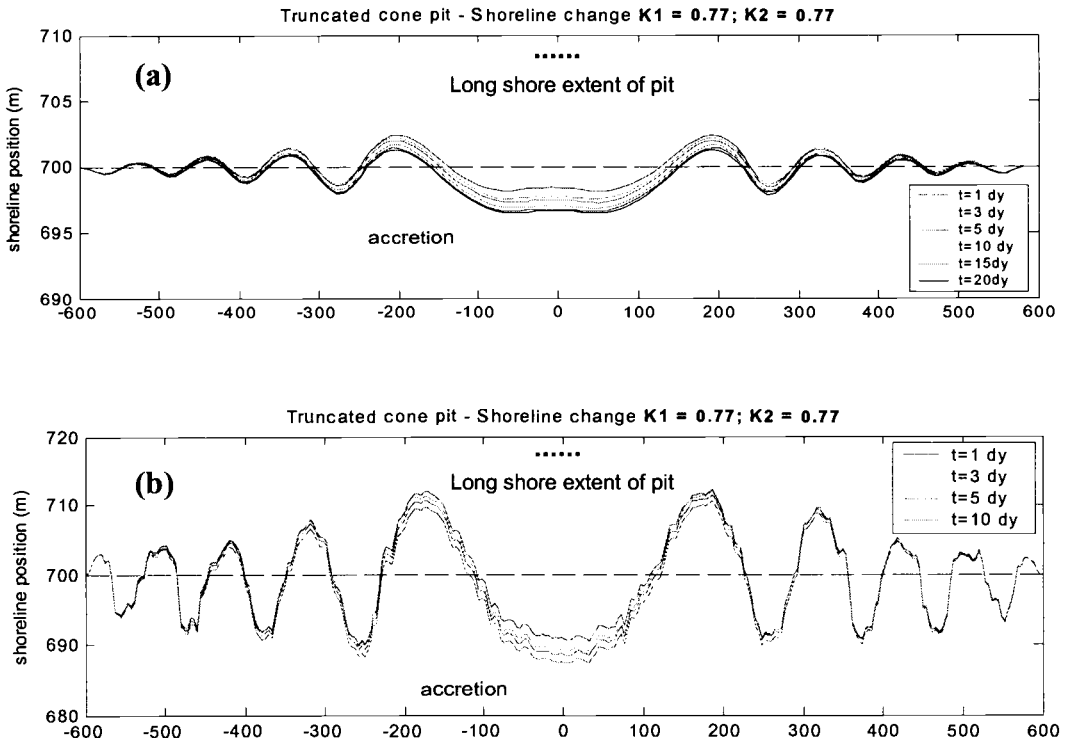

Figure 6.3: Shoreline evolution results for a truncated cone with 1:10 sidewalls and $k_1h_1 = 0.24$. **(a)** MMSE model with t = 20 days **(b)** REF/DIF with t = 10days

6.2 Nearshore Circulation

The circulation pattern that results due to the presence of a borrow pit is investigated using the OK-MODEL by Özkan-Haller and Kirby (1997). The model is a psuedospectral, two-dimensional-horizontal (2DH) circulation model formulated to solve the depth-integrated, phase-averaged Navier Stokes equations. The model can be used independently, or can be coupled with an external wave propagation model. For this example, the latter is performed using information output from the MMSE model in § 5.4.

6.2.1 Basic model formulation

The depth integrated, time averaged Navier Stokes equations including the effects of unsteady forcing due to radiation stress gradients are given as

$$\frac{\partial \eta}{\partial t} + \frac{\partial}{\partial x}\left[u(h+\eta)\right] + \frac{\partial}{\partial y}\left[v(h+\eta)\right] = 0 \tag{6.6}$$

$$\frac{\partial u}{\partial t} + u\frac{\partial u}{\partial x} + v\frac{\partial u}{\partial y} = -g\frac{\partial \eta}{\partial x} + \tilde{\tau}_x + \tau'_x - \tau_{bx} \tag{6.7}$$

$$\frac{\partial v}{\partial t} + u\frac{\partial v}{\partial x} + v\frac{\partial v}{\partial y} = -g\frac{\partial \eta}{\partial y} + \tilde{\tau}_y + \tau'_y - \tau_{by} \tag{6.8}$$

where η is the wave-averaged free-surface elevation, h is the water depth with respect to the still water level; u and v are the depth-averaged current velocities in the x and y directions, and parameters $\tilde{\tau}_x$ and $\tilde{\tau}_y$ denote the radiation stress gradients which follow

$$\tilde{\tau}_x = -\frac{1}{\rho d}\left(\frac{\partial S_{xx}}{\partial x} + \frac{\partial S_{xy}}{\partial y}\right) \tag{6.9}$$

$$\tilde{\tau}_y = -\frac{1}{\rho d}\left(\frac{\partial S_{xy}}{\partial x} + \frac{\partial S_{yy}}{\partial y}\right) \tag{6.10}$$

where ρ is the density of water, $d = h + \eta$, and radiation stresses are calculated in the same manner as Dean and Dalrymple (1991). Additionally parameters τ'_x and τ'_y represent the effects of lateral momentum mixing; and τ_{bx} and τ_{by} represent bottom friction. The specification and theory for these parameters may be found in Özkan-Haller and Kirby (2002).

6.2.2 Model inputs

In addition to the bathymetry, the only information required from the external wave model are the forcing terms $\tilde{\tau}_x$ and $\tilde{\tau}_y$, wave height H_{rms}, and breaking dissipation ϵ_b, which is given by Thorton and Guza (1983) as

$$\varepsilon_b = \frac{3\sqrt{\pi}}{16}\frac{\rho g B^3 f_p}{\gamma^4 d^5} H_{rms}^7 \tag{6.11}$$

where f_p is the peak frequency, and the wave transformation parameters are $B = 0.78$ and $\gamma = 0.45$. The dissipation is required to calculate the mixing and bottom friction terms. In the present study, similar constants employed by the authors are selected. The mixing coefficient: $M = 0.25$ and bottom friction coefficient: $c_f = 0.006$. Additionally, the domain origin of the OK-MODEL model is set up in a different manner than the wave model, as illustrated in Figure 6.4. Therefore, the appropriate steps must be taken in transforming the data from the wave model convention to the convention used by the OK-MODEL.

6.2.3 Model application: Rectangular shaped pit with tapered sidewalls

The model was run for the case of a rectangular shaped borrow pit with tapered sidewalls with slope 1:1. Additionally, the nearshore surf zone has a beach slope of $\tan\beta = 0.02$. The domain for the OK-MODEL was slightly smaller than the domain modeled by the MMSE wave model; as demonstrated by Figure 6.4. In the OK-MODEL, the cross-shore domain extends only $x_{circ} = 750$ m from the shoreline, while the longshore domain extends $y_{circ} = 2000$ in total length. Additionally, to decrease the computational time, the grid size used by the OK-MODEL was $\Delta x_{circ} = 4$ m, rather than the grid size the specified in the wave model $\Delta x_{wave} = 1$ m.

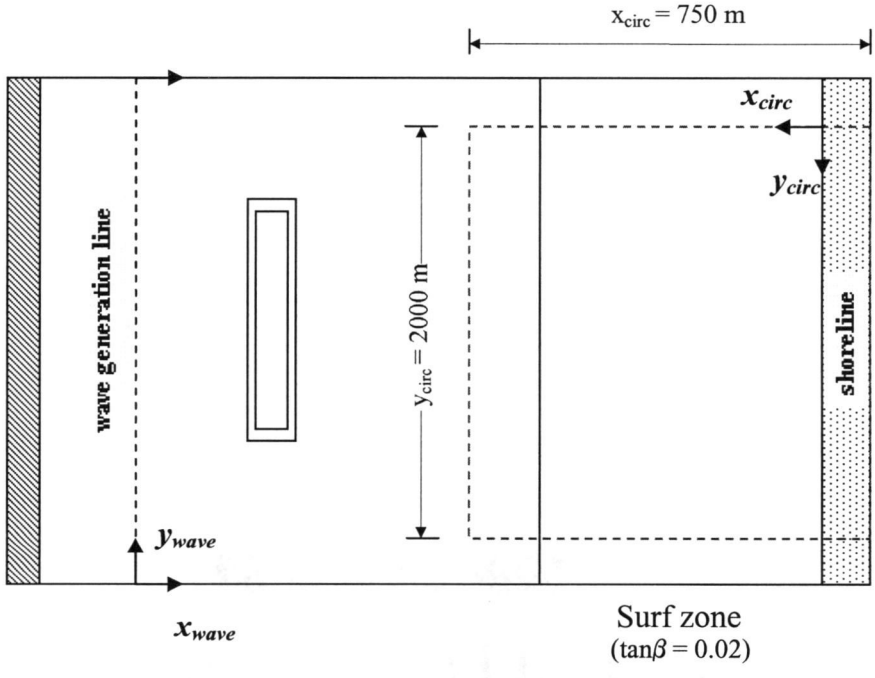

Figure 6.4: Circulation model domain in reference to wave model domain

The purpose of the current test is to determine whether the longshore gradients in wave height illustrated by the wave model results, will result in currents induced by MWL gradients. The OK-MODEL outputs the longshore and cross-shore velocities as a function of time at a specified time interval and step size. In this example the model is run for approximately 10 minutes in time following the initial forcing.

Analyzing the trends and magnitudes of the velocity vectors will indicate the presence of wave driven flows. Additionally, the presence of rip currents can be determined by looking at vorticity snapshots in time. Vorticity is related to the longshore and cross-shore current velocities as

$$q = \left(\frac{\partial v}{\partial x} - \frac{\partial u}{\partial y} \right) \tag{6.12}$$

and has units of (1/s). Figures 6.5 and 6.6 illustrate the initial periods of a rip current formation directly adjacent to the longshore extent of the pit corners (i.e. y = 1000 m and y = 2000 m). The figures are enlarged to focus on one rip (y = 2000 m), since the formation is symmetric about the pit centerline (y = 1500 m). The process can be demonstrated by the velocity vectors at various stages in time; the arrows illustrate that converging flows meet at y = 2000 m. This is a result of the region of low setup created in the shadow zone surrounded by two regions of high setup. The figures also illustrate the magnitude of vorticity denoted by the color map. Here, a rip neck is indicated by a strip with opposite magnitudes of vorticity located on either side of the neck. By the time of t = 512 s, the rip currents appear to be shedding vortices.

Another interesting effect to notice is the magnitude of the longshore flows traveling from y > 2000 m compared to those traveling from y < 2000 m. The currents are much larger for the former, especially at the later snapshots in time. Reasons for this can be explained by referring back to Figures 5.18 (a) and 5.19 (a), which illustrates that the longshore gradient in wave height is much larger in the region y > 2000 m than for y < 2000m. This leads to the conclusion that the magnitude of the gradient longshore gradient in wave height dominates the magnitude of the currents.

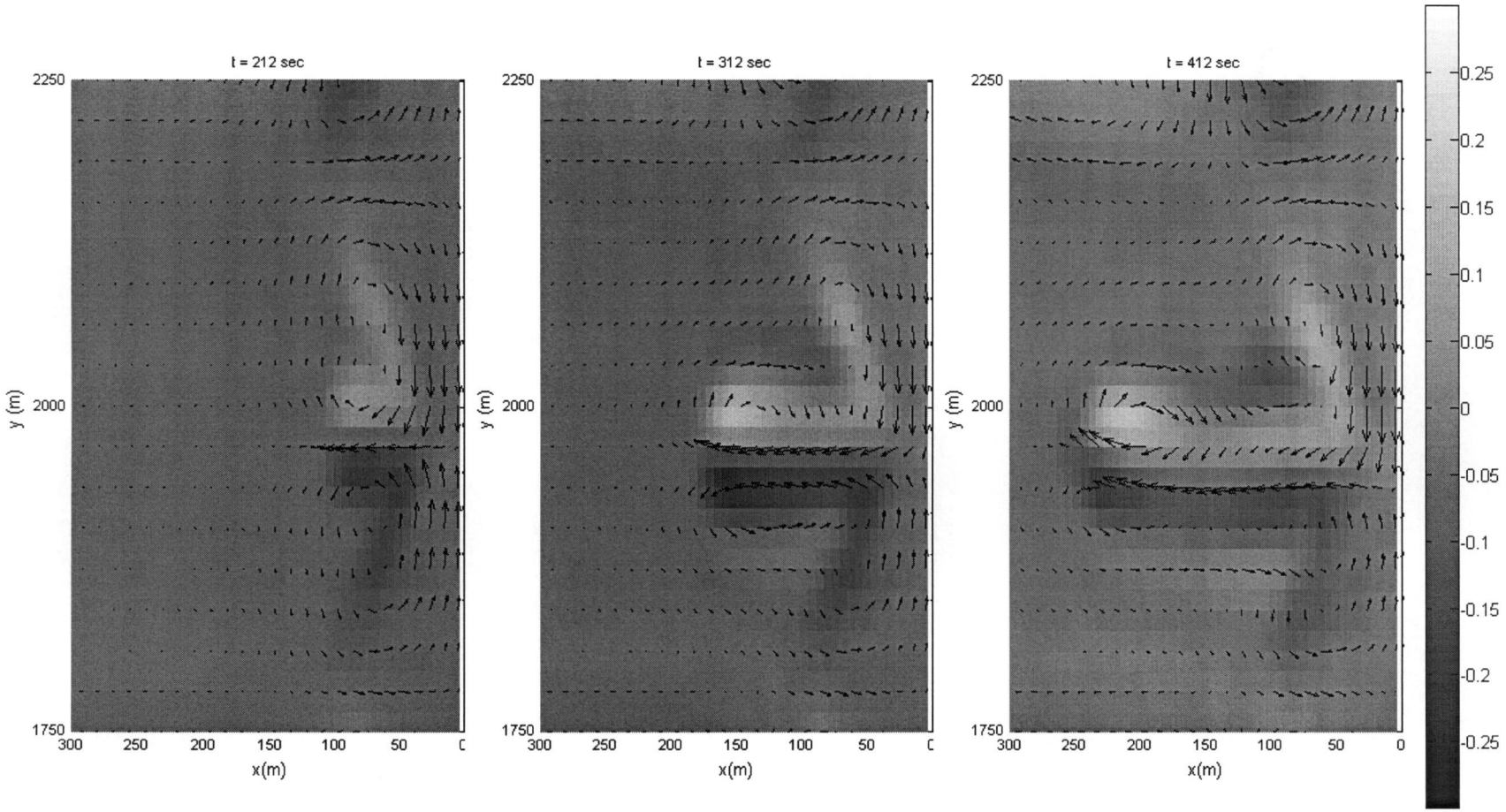

Figure 6.5: Snapshots of vorticity q (1/s) in surf zone for a rectangular pit. **(a)** $t = 212$ s **(b)** $t = 312$ s **(c)** $t = 412$ s

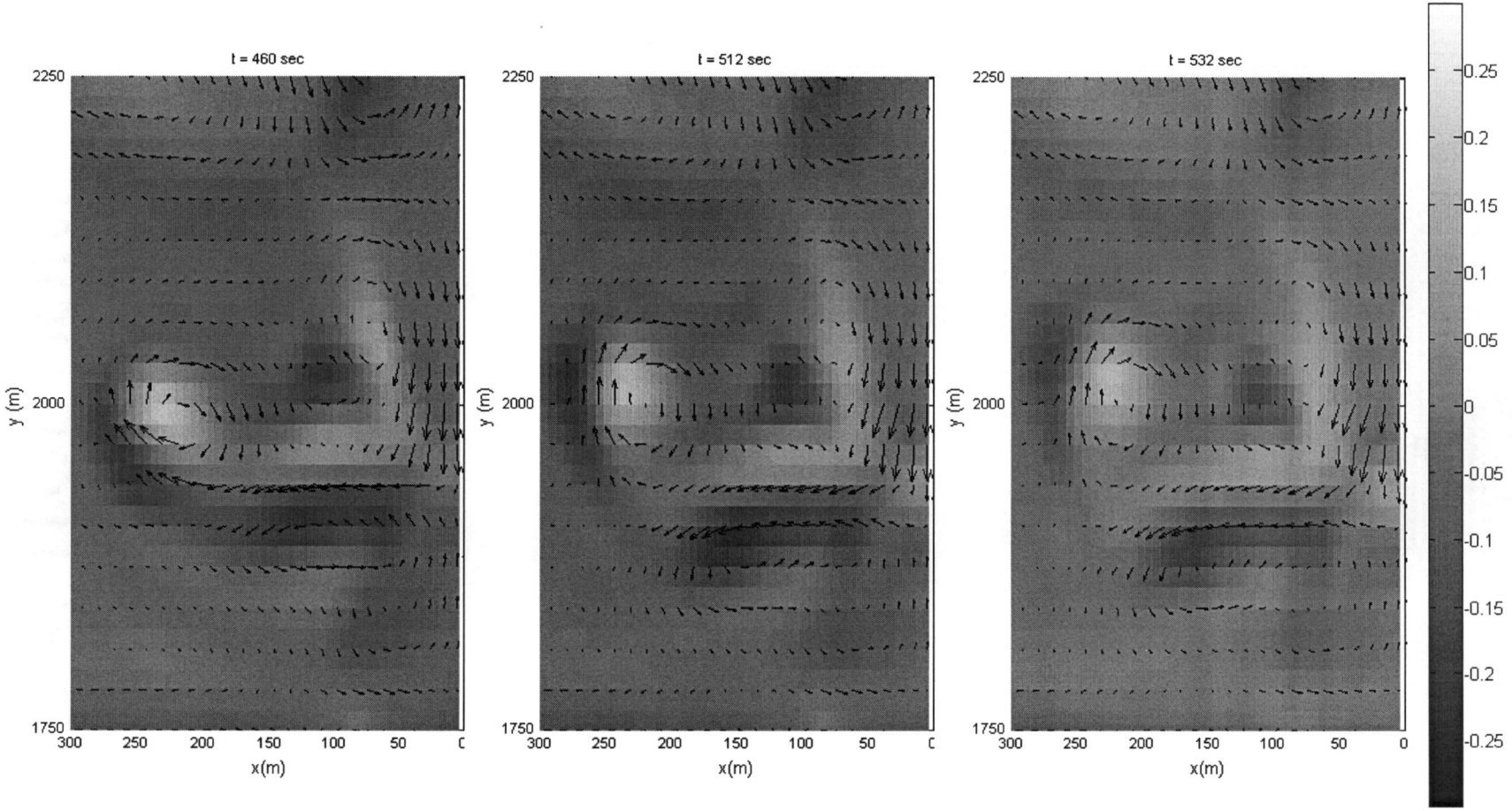

Figure 6.6: Snapshots of vorticity q (1/s) in surf zone for a rectangular pit. **(a)** $t = 460$ s **(b)** $t = 512$ s **(c)** $t = 532$ s

In summary, this analysis indicates that longshore currents generated by MWL gradients exist and can be strong enough to create rip currents. For this case two shadow regions with significant wave attenuation occurred from the presence of the borrow pit. Thus, two rip formations occurred at each region. However, depending on the longshore extent of the borrow pit, as well as the incident wave conditions different wave patterns can result, thereby creating different circulation patterns. For long waves (i.e. $kh < \pi/10$) and borrow pits that have similar longshore and cross-shore dimensions (i.e. $a \approx b$), the wave field is generally described by having one shadow region directly leeward of the pit (e.g. Figures 5.3 to 5.5). However, for shorter waves ($kh > \pi/10$) and longer rectangular shaped pits, the shadow region separates into two distinct regions (e.g. Figure 5.9 and 5.13). Therefore, rip currents can be generated at different longshore positions depending on the location of the shadow region.

Finally, the fact that rip currents are shown to form from the presence of a borrow pit raises additional questions about the accuracy of shoreline evolution models commonly utilized to study the impacts of borrow pits on the shoreline. In the presence of these flows, one-line models fail to account for sediment carried with the offshore flow associated with rip currents. Since one-line models are shown to predict areas of accretion at the longshore positions (e.g. Figures 6.1 and 6.2) where rip currents form, in theory sediment may be carried offshore from this region rather than accreting. This would result in a significantly different shoreline response trend.

7.0 Conclusions

A modified mild-slope equation (MMSE) wave model was employed to investigate the significance of the known errors associated with Berkhoff's (1972) original mild-slope equation (MSE), most notably in situations when the mild-slope criterion is violated or where wave reflection is substantial. It is theorized that the inaccuracies resulting from the use of models based on this formulation would transfer errors into other models predicting shoreline response. The analysis is primarily important in the case of offshore borrow sites or other bathymetric anomalies located in the nearshore region that significantly modify the wave climate. Although analytical methods describing wave transformation around such features exist, they require highly idealized bathymetries which are not typically observed in the field. Therefore, the use of the numerical model is essential in estimating the potential impacts of examples like the offshore borrow pit. Many wave models currently used involve a parabolic approximation to the elliptic MSE in order to reduce computational requirements. However, this results in two limitations in the wave model: (1) the inability to predict wave transformation over steep features and (2) the inability to include reflected (backscattered) waves.

The MMSE corrects for the MSE's limitation in representing steep features. Additionally, the implementation of a hyperbolic solution allows the inclusion of reflected waves. Therefore, in order to determine its applicability for modeling the case of an offshore borrow pit, the MMSE model was tested against known analytical solutions for a two-dimensional trench. It was determined that the model performed well for trench sidewall slopes as large as 1:1. For practical applications this limit is acceptable since the maximum slope attainable in the field is controlled by the angle of repose of the sediment.

In addition, the significance of reflection generated from a trench was studied. Using the dimensionless properties about the geometry of borrow pits in the field, it was shown under the right conditions, borrow sites are capable of reflecting 30% (i.e $K_r > 0.3$) of the incident wave energy. Consequently, a classification describing when the effects of reflection are largest was included as part of a parameterization analysis. Here, it was demonstrated that the variability of the maxima in the reflection

coefficient is a function of the ratio between the cross-shore width and wavelength inside the trench for shallow water conditions. However, in the transition into intermediate water this relation changes; the degree of change is a function of the depth and sidewall slopes of the trench. Thus, a preliminary set of design guidelines were constructed as a guide to prevent the implementation of borrow pits with highly reflective properties.

Next the impacts on the wave field in three-dimensions were analyzed. In these cases the longshore finiteness of the pit substantially changes the wave pattern leeward of the feature. Through the effects of refraction and diffraction, a shadow region of low wave setup forms. First the effects of borrow pit shape was analyzed by looking a three possible pit shapes: a tapered square, truncated cone, and Gaussian shape. Holding the pit width, length, and sidewall slope constant it was demonstrated that all produce similar wave patterns in lee of the feature regardless of shape. Secondly, it was demonstrated that although reflection may also be substantial in the direct vicinity of a borrow pit, the effects of refraction and diffraction far outweigh its influence leeward of the feature. This was shown by comparing a specific case where the differences in the reflection coefficient predicted by the MMSE to the MSE model were most pronounced. A conclusion of this result suggests that the use of the MSE equation does not significantly alter the predictions in wave height far away from the feature and the utilization of this formulation would not generate significant errors in basic shoreline evolution models. This claim was validated by placing a surf zone leeward of the borrow pit, and calculating the wave conditions at breaking. Through the application of a common one-line model, it was determined that the differences between the MMSE and MSE did not significantly alter the predicted shoreline response.

As a final study, the presence of mean water level gradient driven currents is investigated by applying a 2DH nearshore circulation model. The results indicated that the regions of low setup created by the shadow region leeward of the pit create an area where converging longshore currents meet. As a result, the beginnings of rip currents are generated, suggesting possible offshore return of water. However, previous studies investigating the shoreline response near borrow sites have applied a

one-line model that is incapable of including the effects of MWL gradient induced flows. Therefore, the sediment transport trend that may result in the presence of rip currents is not represented. Thus, in order to accurately model the process a more advanced sediment transport model capable of describing the above process is required. It would be of interest to investigate the predictions in shoreline response using an energetics based sediment transport model (e.g. Bailard 1981). This would undoubtedly provide further insight into the creation of erosional hot spots, and more importantly their prediction.

Bibliography

Allen, J.R.L. 1970. The avalanching of granular solids on dune and similar slopes, *Journal of Geology*, 78: 326-351.

Bailard, J.A. 1981. An energetics total load sediment transport model for a plane sloping beach, *Journal of Geophysical Research*, 86: 10938-10954.

Bender, C.J. and Dean, R.G. 2001. Erosional hot spot prediction through wave analysis. *Proceedings of the Fourth International Symposium on Ocean Wave Measurement and Analysis* (WAVES 2001), ASCE, Reston, vol. II, 1306-1315.

Bender, C.J. 2003. Wave transformation by bathymetric anomalies with gradual transitions in depth and resulting shoreline response. Doctoral Dissertation. Department of Civil and Coastal Engineering, University of Florida.

Bender, C.J. and Dean, R.G. 2003. Wave field modification by bathymetric anomalies and resulting shoreline changes: a review with recent results. *Coastal Eng*ineering, 49: 125-153.

Berkhoff, J.C.W., 1972. Computation of combined refraction-diffraction. *Proceedings of the 13th International Conference on Coastal Engineering*, ASCE, 471-490.

Booij, N. 1981 Gravity waves on water with non-uniform depth and current. Rep. No. 81-1, Dept. of Civ. Eng., Delft Univ. of Technology.

Booij, N. 1983. A note on the accuracy of the mild-slope equation. *Coastal Engineering*, 7: 191-203.

Chamberlain, P.G., and Porter, D. 1995. The modified mild-slope equation. *Journal of Fluid Mechanics*, 291: 393-407.

Combe, A.J., and Soileau, C.W. 1987. Behavior of man-made beach and dune: Grand Isle, Louisiana, *Proceedings of Coastal Sediments '87*, ASCE, 1232-1242.

Copeland, G.J.M. 1985. A practical alternative to the "mild-slope" wave equation. *Coastal Engineering*, 9: 125-149.

Davies, A.G. and Heathershaw, A.D. 1984. Surface-wave propagation over sinusiodally varying topography. *Journal of Fluid Mechanics*, 144: 419-443.

Dean, R.G. 1964. Long wave modification by linear transitions. *Journal of the Waterways and Harbors Division*, ASCE, 90 (1): 1-29.

Dean, R.G. and Dalrymple, R.A. *Water wave mechanics for engineers and scientists.* Singapore: World Scientific, 1991.

Dean, R.G., Liotta, R., and Simon, G. 1999. Erosional hot spots. UFL/COEL-99/021. Department of Coastal and Oceanographic Engineering, University of Florida.

Dean, R.G. and Dalrymple, R.A. *Coastal Processes with Engineering Applications.* Cambridge University Press, 2002.

Demir, H., Otay, E.N., Work, P.A., and Börekçi, O.S., 2004. Impacts of dredging on shoreline change. *Journal of Waterway, Port, Coastal, and Ocean Engineering*, ASCE, 130 (4): 170-178.

Dingemans, M.W. *Water wave propagation over uneven bottoms: Part 1 – Linear wave propagation*. Singapore: World Scientific, 1997.

Ebersole, B.A., Cialone, M.A., and Prater, M.D. 1986. Regional coastal processes numerical modeling system, Report 1, A linear wave propagation model for engineering use. Technical Report CERC-86-4. CERC, Department of the Army, WES, Corps of Engineers.

Fernandez, G.J., 1999. Erosional hot spots at Delray Beach, Florida: mechanisms and probable causes. Masters Thesis. Department of Civil and Coastal Engineering, University of Florida.

Gourlay, M.R. 1982. Nonuniform alongshore currents and sediment transport – A one-dimensional approach. Civil Engineering Research Report No. CD31. Department of Civil Engineering, University of Queensland, St Lucia, Queensland.

Gravens, M.B., and Rosati, J.D. 1994. Numerical study of breakwaters at Grand Isle, Louisiana, Miscellaneous Paper CERC-94-16. U.S.Army Corps of Engineers, Vicksburg, Mississippi.

Gravens, M.B. 1997. Wave resolution effects on predicted shoreline positions, *Journal of Waterway, Port, Coastal, and Ocean Engineering*, 123 (1): 23-33.

Hanson, H., and Kraus, N.C. 1989. GENESIS – Generalized model for simulating shoreline change. Vol. 1: reference manual and users guide, USAE-WES, Coastal Engineering Research Center, Vicksburg, Mississippi.

Horikawa, K., Sasaki, T., and Sakuramoto, H. 1977. Mathematical and laboratory models of shoreline change due to dredged holes. *Journal of the Faculty of Engineering*, The University of Tokyo, XXXIV, No. 1: 49-57.

Kelley, S.W., Ramsey, J.S., and Byrnes, M.R., 2004. Evaluating the physical effects of offshore sand mining for beach nourishment. *Journal of Coastal Research*, 20 (1): 89-100.

Kirby, J.T. and Dalrymple, R.A. 1983a. Propagation of obliquely incident waves over a trench. *Journal of Fluid Mechanics*, 133: 47-63.

Kirby, J.T. 1986. A general wave equation for waves over ripples. *Journal of Fluid Mechanics*, 162: 171-186.

Kirby, J.T. and Dalrymple, R.A. 1994. User's manual, combined refraction / diffraction model, REF/DIF-1, Version 2.5. Center for Applied Coastal Research, Department of Civil Engineering, University of Delaware. Newark, Delaware.

Kojima, H., Ijima, T., and Nakamuta, T. 1986. Impact of offshore dredging on beaches. along the Genkai Sea, Japan. *Proceedings 20th International Conference on Coastal Engineering*, Taipai, II, ASCE, New York, 1281-1295.

Komar, P.D. 1969. The longshore transport of sand on beaches. Ph. D thesis. University of California, San Diego.

Kraus, N.C., and Harikai, S. 1983. Numerical model of the shoreline change at Oarai Beach. Coastal Engineering, 7: 1-28.

Kraus, N. C., and Galgano, F. A. 2001. Beach erosional hot spot: Types, causes, and solutions, ERDC/CHL Coastal and Hydraulics Engineering Technical Note CHETN-II-44, U.S. Army Engineer Research and Development Center, Vicksburg, MS. *(http://chl.wes.army.mil/library/publications/chetn)*

Lamb, H. 1932. Hydrodynamics: 5th Edition. University Press, Cambridge. Section 176.

Larson, J., Dancy, H. 1983. Open boundaries in short wave simulations—a new approach. *Coastal Engineering*, 7: 243-257.

Lee, J J. and Ayer, R.M. 1981. Wave propagation over a rectangular trench. *Journal of Fluid Mechanics*,110: 335-347.

Lee, C., and Suh, K.D. 1998. Internal generation of waves for time-dependent mild-slope equations. *Coastal Engineering*, 34: 35-57.

Lee, C., Park, W.S., Cho, Y.-S., and Suh, K.D., 1998. Hyperbolic mild-slope equations extended to account for rapidly varying topography. *Coastal Engineering*, 34: 243-257.

Lee, H.S., Williams, A.N., Lee, B.H., and Oh, J., 2002. Diffraction of multidirectional random waves by multiple rectangular submarine pits. *Ocean Engineering*, 30, 85-106.

Long, J.W., Özkan-Haller, T.H., Kaihatu, J.M., Lippmann, T.C., Shore, J.A., and Welsh, D., On the wave and circulation field at the nearshore canyon experiment (NCEX), *EOS Trans. AGU, 84(52)*, Ocean Sci. Meet. Suppl., Abstract OS21I-04, 2003.

Maa, J.P.-Y., and Hobbs, C.H. III. 1998. Physical impacts of waves on adjacent coasts resulting from dredging at Sandbridge Shoal, Virginia. *Journal of Coastal Research*, 14 (2): 525-536.

Maa, J.P.-Y., Hobbs, C.H. III.,and Hardaway, C.S. 2001. A criterion for determining the impact on shorelines caused by altering wave transformation. *Journal of Coastal Research*, 17 (1): 107-113.

Maa, J.P.-Y, Hsu, T.-W, and Lee, D.Y. 2002. The RIDE model: an enhanced computer program for wave transformation. *Ocean Engineering*, 29: 1441-1458.

Madsen, P.A., Larson, J. 1987 An efficient finite-difference approach to the mild-slope equation. *Coastal Engineering*, 11: 329-351.

Madsen, P.A., Bingham, H.B., and Wang, B. 2002. Velocity formulations and mild-slope approximations in the framework of Boussinesq theory. *Proceedings 28th International Conference on Coastal Engineering*, Cardiff, UK, World Scientific Publishing Co. Pte. Ltd., New Jersey, London, Singapore, Hong Kong, 472-484.

Massel, S.R. 1993. Extended refraction-diffraction equation for surface waves. *Coastal Engineering*, 19: 97-126.

McDougal, W.G., Williams, A.N., and Furukawa, K. 1996. Multiple pit breakwaters. *Journal of Waterway, Port, Coastal, and Ocean Engineering*, ASCE, 122: 27-33.

Mei, C.C. 1985. Resonant reflection of surface water waves by periodic sandbars. *Journal of Fluid Mechanics*, 152: 315-335.

Michalsen, D.R., Haller, M.C., and Suh, K.D. 2003. Erosional hot spot modeling: The impact of offshore borrow holes, *Coastal Engineering Today/ACE Conference*, Fall, 2003

Miles, J.W. 1967. Propagation of water waves over an infinite step. *Journal of Fluid Mechanics*, 23: 399-415.

Motyka, J.M., and Willis, D.H. 1974. The effect of refraction over dredged holes. *Proceedings 14th International Conference on Coastal Engineering*, Copenhagen, ASCE, New York, 615-625.

Ozasa, H. and Brampton, A.H. 1979. Models for predicting the shoreline evolution of beaches backed by seawalls. Report No IT 191. Hydraulics Research Station, Wallingford, England.

Özkan-Haller, H. T. and Kirby, J.T. 1997. A Fourier-Chebyshev collocation method for the shallow water equations including shoreline runup, *Applied Ocean Research*, 19: 21-34.

Özkan-Haller, T.H. and Kirby, J.T. 2002. OK-MODEL: A Pseudospectral solution of nearshore wave and circulation problem, Documentation and User's Manual

Pelnard-Considère, R., 1956, "Essai de Théorie de l'Evolution des Formes de Rivage en Plages de Sable et de Galets," 4th Journees de l'Hydraulique, Les Energies de la Mer, Question III, Rapport No. 1.

Price, W.A., Motyka, J.M. and Jaffrey, L.J. 1978. The effect of offshore dredging on coastlines. *Proceedings 16th International Conference on Coastal Engineering*, Hamburg, ASCE, New York, II, pp. 1347-1358.

Radder, A.C. 1979. On the parabolic equation method for water-wave propagation. *Journal of Fluid Mechanics*, 95: 159-176.

Smith, J.M., Sherlock, A.R., and Resio, D.T. 2001. Steady-state spectral wave model user's manual for STWAVE, Version 3.0. *Special Report ERDC/CHL SR-0101*, U.S. Army Waterways Experiment Station, Vicksburg, Miss.

Suh, K.D., Lee, C., and Park, W.S., 1997. Time-dependent equations for wave propagation on rapidly varying topography. *Coastal Engineering*, 32: 91-117.

Suh, K.D. Lee, C., Park, Y., and Lee, T.H. 2001. Experimental verification of two-dimensional modified mild-slope equation model. *Coastal Engineering*, 44: 1-12.

Takano, K. 1960. Effets d'un obstacle paralélléléipipédique sur la propagation de la houle. *Houille Blanche*, 15: 247-267.

Thornton, E.B. and Guza, R.T. 1983. Transformations of wave height distribution. *Journal of Geophysical Research*, 88: 5925-5938.

Thornton, E.B. and Stanton, T., Modeling of surfzone generated infragravity waves during NCEX, *EOS Trans. AGU, 84(52),* Ocean Sci. Meet. Suppl., Abstract OS12E-02, 2003.

U.S. Army Corps of Engineers, 2001. Coastal Engineering Manual. Engineer Manual 1110-2-1100, U.S. Army Corps of Engineers, Washington, D.C.

Van Dolah, R.F., Digre, B.J., Gayes, P.T., Donovan-Ealy, P. and Dowd, M.W., 1998. An Evaluation of Physical Recovery Rates in Sand Borrow Sites Used for Beach Nourishment Projects in South Carolina. Final Report Submitted to: The South Carolina Task Force on Offshore Resources and the Mineral Management Service, Office of International Activities and Marine Minerals. 76pp plus Appendices.

Watanabe, A., and Dibajnia, M., 1988. A numerical model of wave deformation in surf zone. *Proceedings of the 21st International Conference on Coastal Engineering*, ASCE, 578-587.

Williams, A.N. 1990. Diffraction of long waves by a rectangular pit. *Journal of Waterway, Port, Coastal, and Ocean Engineering,* ASCE, 116: 459-469.

Williams, A.N. and Vasquez, J.H. 1991. Wave interaction with a rectangular pit. *Journal of Offshore Mechanics and Arctic Engineering*, 113: 193-198.

Williams, B.P. 2002. Physical modeling of nearshore response to offshore borrow pits. Masters Thesis. Department of Civil and Coastal Engineering, University of Florida.

Work, P.A., Fehrenbacher, F., Voulgaris, G., and Chen, W. 2003. Nearshore Dredging Impacts, Folly Island, South Carolina, USA. *Proceedings of Coastal Sediments '03*, ASCE, St. Petersburg, FL, May 2003.

Appendix A: Components of terms R_1 and R_2 in MMSE formulation

$$W_1 = -2\lambda + 2\frac{k_h}{k} + 2\frac{kh \cdot k_h}{\lambda} - 4\frac{\lambda h \cdot k_{hh}}{k} + \frac{h \cdot k_{hh}}{k} + \frac{h^2 k_h^2}{\lambda} - 2\frac{\lambda h^2 \cdot k_h^2}{k^2} \tag{A.1}$$

$$W_2 = 2k - 2\frac{k_h}{\lambda} + 2h \cdot k_h \tag{A.2}$$

$$W_3 = 2k_h - \frac{k_{hh}}{\lambda} + 2\frac{h \cdot k_h^2}{k} \tag{A.3}$$

$$W_4 = -2\frac{k \cdot k_h}{\lambda} \tag{A.4}$$

$$W_5 = -\frac{k_h^2}{\lambda} \tag{A.5}$$

$$W_6 = 1 + \frac{h \cdot k_h}{k} \tag{A.6}$$

$$U_1 = 1 + \frac{h \cdot k_h}{k} \tag{A.7}$$

$$U_2 = -\frac{k}{\lambda} \tag{A.8}$$

$$U_3 = -\frac{k_h}{\lambda} \tag{A.9}$$

$$I_1 = \int_{-h}^{0} \cosh^2 k(h+z)dz \tag{A.10}$$

$$I_2 = \int_{-h}^{0} \cosh k(h+z)\sinh k(h+z)dz \tag{A.11}$$

$$I_3 = \int_{-h}^{0} (h+z)\cosh k(h+z)\sinh k(h+z)dz \tag{A.12}$$

$$I_4 = \int_{-h}^{0} (h+z)\cosh^2 k(h+z)dz \tag{A.13}$$

$$I_5 = \int_{-h}^{0} (h+z)^2 \cosh^2 k(h+z)dz \tag{A.14}$$

$$k_h = \frac{\partial k}{\partial h} = -\frac{\lambda k}{\lambda h + \sinh^2 kh} \tag{A.15}$$

$$k_h h = \frac{\partial^2 k}{\partial h^2} = -\frac{\lambda k}{\lambda h + \sinh^2 kh}\left(2 + \frac{k + h \cdot k_h}{\lambda} \cdot \sinh 2kh\right) \tag{A.16}$$

$$\lambda = \frac{\omega^2}{g} = k \tanh kh \tag{A.17}$$